

**Cytochrome P450 Structure and Function Supporting Drug Design for Major Human Diseases and
Drug Metabolism and Toxicity Predictions in Neonates**

by

Jinghan Liu

A dissertation submitted in partial fulfillment
of the requirements for the degree of
Doctor of Philosophy
(Medicinal Chemistry)
in the University of Michigan
2023

Doctoral Committee:

Professor Emily E. Scott, Chair
Professor Richard J. Auchus
Professor Jolanta Grembecka
Professor Nouri Neamati

Jinghan Liu

ljinghan@umich.edu

ORCID iD: 0000-0001-7803-3070

© Jinghan Liu 2023

Dedication

This dissertation is dedicated to all the trainees, past, present, and future in Emily Scott's laboratory.

Acknowledgements

I would like to thank everyone that has supported me throughout my graduate career. I am grateful to Dr. Heather Carlson, Dr. Francis Yoshimoto, Dr. Jed Lampe, Dr. Sylvie Kandel, Dr. Samuel Offei, and Schuyler Byrn for direct contributions in at least one of the projects described in this dissertation. Additionally, I would like to thank the many Scott Lab members for their various support through the years: Dr. Simone Brixius-Anderko, Dr. Aaron Bart, Dr. Kurt Harris, Dr. Nicole Motl, Sarah Burris-Hiday, Alaina Richard, Cara Loomis, and Ellie Frydendall.

I am also very grateful to Dr. Nouri Neamati, Dr. Richard Auchus, and Dr. Jolanta Grembecka who have served on my committee. Their advice and support have been invaluable to both my research and my professional growth.

Most importantly, I am extremely grateful to my advisor Dr. Emily Scott, who welcomed me into her lab when I had no experience in protein crystallography. Through every stage of this journey, Dr. Scott has consistently been at my side, offering unwavering trust, mentorship, encouragement, and support, shaping me into a better scientist and a more confident person. I am extremely fortunate to have been part of her lab. She is quite possibly the best mentor any student could ask for.

The research in this dissertation was made possible due to the funding from NIH Grant R37 GM076343 and NIH Grant R01 AI150494. Data for the crystal structures in this dissertation

were collected at both the Stanford Synchrotron Radiation Lightsource and the Advanced Photon Source. I wish to extend my gratitude to the University of Michigan Center for Structural Biology, whose generous provision of crystallization instrumentation was vital to my work. I would like to offer particular thanks to Dr. Jennifer Meagher, who not only trained me in using this equipment, but also provided consistent guidance throughout this process.

I am also appreciative for the support from Medicinal Chemistry Department, especially to Dr. Amanda Garner, who have supported me over the years, and to Sarah Lloyd and Grey Hendry, who have helped answer questions and coordinate with Rackham and International Center. I would also like to thank College of Pharmacy for the fellowship in my first year, and to Antoinette Hopper for all the assistance and resources she has provided.

Finally, I would like to thank all my friends and family for their support and encouragement throughout my graduate education. In particular I want to thank my boyfriend Charles Zhang, whose love and encouragement have been absolutely vital to my success as a graduate student.

Table of Contents

Dedication.....	ii
Acknowledgements.....	iii
List of Tables	x
List of Figures.....	xi
Abstract.....	xix
Chapter 1 Introduction	1
1.1 Cytochrome P450 Spectroscopic Features.....	2
1.2 Cytochrome P450 catalytic Cycle.....	4
1.2.1 Cytochrome P450 redox partner.....	6
1.3 Structure of Cytochrome P450.....	7
1.3.1 Structural conservation and diversity.....	7
1.3.2 Conformational Dynamics.....	9
1.4 Cytochrome P450 Enzymes Involved in Bile Acids Synthesis.....	10
1.4.1 Cytochrome P450 8B1	11
1.4.2 Cytochrome P450 27A1	16
1.5 CYP3A7 Role in Fetal Development and Xenobiotic Metabolism	18
1.5.1 Steroidogenic pathway and estriol production	19
1.5.2 Xenobiotic metabolism and drug elimination	20
1.6 Conclusions	22
Chapter 2 The structure and characterization of human cytochrome P450 8B1 supports future drug design for nonalcoholic fatty liver disease and diabetes	23

2.1 Summary	23
2.2 Introduction	24
2.3 Experimental Procedures.....	26
2.3.1 Expression and purification of CYP8B1 and W281F mutant	26
2.3.2 Human cytochrome P450 reductase	29
2.3.3 Crystallization and structural determination	29
2.3.4 Ligand binding assay	30
2.3.5 Determination of kinetic parameters	30
2.3.6 CYP8B1 inhibition assays.....	31
2.3.7 Docking 7α -hydroxycholest-4-en-3-one into the CYP8B1 active site.....	32
2.4 Results	33
2.4.1 Generation of Recombinant CYP8B1	33
2.4.2 CYP8B1 Substrate Binding.....	34
2.4.3 CYP8B1 Catalysis	35
2.4.4 Recombinant CYP8B1 W281F Substrate Binding and Catalysis	36
2.4.5 CYP8B1 Inhibitor Binding.....	38
2.4.6 CYP8B1 Inhibition.....	40
2.4.7 Structure of CYP8B1 Co-crystallized with the Nonselective Inhibitor (S)-Tioconazole	42
2.4.8 Docking of Native Substrate	45
2.5 Discussion	46
2.5.1 Recombinant CYP8B1 Characterization.....	46
2.5.2 CYP8B1 Function	48

2.5.3 Towards CYP8B1 Inhibitors	49
2.5.4 Analysis of Opportunities for Selectively Targeting CYP8B1	51
2.6 Conclusion.....	55
Chapter 3 Pyridine-containing substrate analogs are restricted from accessing the human cytochrome P450 8B1 active site by tryptophan 281	56
3.1 Summary	56
3.2 Introduction	57
3.3 Experimental procedures.....	60
3.3.1 Synthesis of 12-(3'-pyridyl)-androsta-4,11-dien-3,17-dione (Compound 8).....	60
3.3.2 Synthesis of 12-(3'-pyridyl)-androsta-4,11-diene 3a,17b-diol (Compound 9)	61
3.3.3 Expression and purification of WT and W281F mutant CYP8B1	61
3.3.4 Expression and purification of Human cytochrome P450 reductase.....	62
3.3.5 Ligand binding assay	62
3.3.6 WT and W281F mutant CYP8B1 inhibition assays.....	62
3.3.7 Crystallization and structural determination	63
3.4 Results	64
3.4.1 Chemical Synthesis of Compounds.....	64
3.4.2 CYP8B1 Binding of 12-Pyridine Substituted Steroids	64
3.4.3 CYP8B1 Inhibition by 12-Pyridine Substituted Steroids.....	66
3.4.4 Structure of CYP8B1 Co-crystallized with Compound 8	67
3.4.5 W281F Mutation in P450 8B1 Has Enhanced Interaction with and Inhibition by 12-Pyridine Substituted Steroids	70
3.5 Discussion	72

3.6 Conclusion.....	77
Chapter 4 Cytochrome P450 3A7 Structure Reveals Four Binding Sites for Its Native Substrate Dihydroepiandrosterone Sulfate	78
4.1 Summary	78
4.2 Introduction	78
4.3 Experimental procedures.....	81
4.3.1 Materials.....	81
4.3.2 Expression and Purification of Wild Type and Hexa-mutant CYP3A7.....	82
4.3.3 Expression and Purification of Human Cytochrome P450 Reductase and Cytochrome b ₅	83
4.3.4 Ligand Binding Assay	83
4.3.5 Wild Type and Hexa-mutant CYP3A7 DHEA-S 16 α -Hydroxylation Kinetic Assay .	84
4.3.6 Analytical Method for DHEA-S Hydroxylation	85
4.3.7 Crystallization and Structural Determination.....	86
4.4 Results	87
4.4.1 Wild type and Hexa-mutant CYP3A7 Binding of Substrate DHEA-S and Inhibitor Clotrimazole	87
4.4.2 Kinetics of DHEA-S Metabolism.....	90
4.4.3 Structure of Hexa-mutant CYP3A7 Co-crystallized with DHEA-S	91
4.5 Discussion	99
4.6 Conclusion.....	106
Chapter 5 Cytochrome P450 27A1	107
5.1 Summary	107
5.2 Introduction	108

5.3 Experimental procedures.....	109
5.3.1 Expression and purification of CYP27A1	109
5.3.2 Ligand binding assay	112
5.3.3 Screening of CYP27A1 Crystallization Conditions	112
5.4 Results and discussion.....	113
5.4.1 Generation of Recombinant CYP27A1	113
5.4.2 CYP27A1 Substrate and Inhibitor Binding.....	115
5.4.3 CYP27A1 crystallization screening	120
5.5 Conclusion.....	121
Chapter 6 Conclusion and Future Directions.....	122
Bibliography	129

List of Tables

Table 2.1 CYP8B1 binding and inhibition by azoles.	39
Table 2.2 X-ray data collection, refinement, and validation statistics.	42
Table 3.1 Effects of 12-pyridyl steroidal compounds 7, 8, or 9 on the CYP8B1 heme Soret peak and inhibition of its 7α-hydroxycholest-4-en-3-one 12α-hydroxylation activity. Maximal concentrations of compounds 7-9 in the spectral shift assays were 280 μ M. Inhibition was evaluation of in the presence of 80 μ M concentration of compound. Assays were performed in duplicate.	67
Table 3.2 X-ray data collection, refinement, and validation statistics.	67
Table 4.1 The difference of AICc is representative of the difference between the simpler model (Michaelis-Menten) minus the alternative model (Hill). A negative number for the difference of AICc means that the simpler model has the lower AICc and is preferred.	91
Table 4.2 X-ray data collection, refinement, and validation statistics.	92
Table 4.3 Cα root mean square deviations (rmsd) between each two molecules (A-L) of CYP3A7 structure.	97
Table 5.1 CYP27A1 binding with inhibitors. Groups likely to form Fe-N interactions are circled in red. All titration experiments were done once.	118

List of Figures

- Figure 1.1 Ligand induced spectral shifts in cytochrome P450 enzymes.** Ligands can perturb the heme iron coordination state resulting in unique changes to UV-Vis spectral signal. Ligands (denoted as R) can displace a water typically coordinated to the heme in the resting state to cause one of two main spectra (type I: blue, type II: red). (Figure adapted from Alaina Richard)..... 3
- Figure 1.2 Cytochrome P450 CO-difference spectrum.** Spectral changes of a P450 enzyme when reduced and bound to carbon monoxide gives characteristic Soret absorbance at A) ~450 nm and B)~420 nm. 4
- Figure 1.3 Cytochrome P450 catalytic cycle,** starting from substrate binding to the heme iron and proceeding clockwise⁸ (with permission). P450 substrate is denoted as R-H, and metabolized product as R-OH..... 5
- Figure 1.4 The eukaryotic cytochrome P450 system.** A) The microsomal P450 enzymes accept two electrons from cytochrome P450 reductase and in some cases cytochrome *b₅*. B) The mitochondrial P450 enzymes receive electrons from the adrenodoxin and adrenodoxin reductase system. 7
- Figure 1.5 Cytochrome P450 global structure.** The conserved fold of a human cytochrome P450 enzyme anchored in the endoplasmic reticulum. The P450 enzyme colored pink at the N-terminus through red at the C-terminus. Selected helices, the redox partner binding

region, the substrate entry region, and the proximal side and the distal side of the enzyme are labeled.	9
Figure 1.6 Cytochrome P450 enzymes in bile acid synthesis. CYP7A1, CYP7B1, CYP8B1, CYP27A1, and CYP39A1 facilitate cholesterol metabolism through two pathways: the classic and alternative pathways.	11
Figure 1.7 Structures and names for CYP8B1 substrate and product. CYP8B1 hydroxylates its substrate at C ₁₂ position (red).....	12
Figure 1.8 NAFLD progression.	14
Figure 1.9 Estriol biosynthesis in the human placenta. Dehydroepiandrosterone sulfate (DHEA-S), secreted in prodigious amounts by the fetal adrenal glands, is converted to 16 α -hydroxy-DHEA-S in the fetal liver, which is converted in the placenta to estriol.	19
Figure 2.1 Characterization of recombinant, purified wild type CYP8B1. (A) SDS-PAGE, (B) UV-visible absorbance spectrum, indicating heme incorporation with a Soret λ_{\max} at 420 nm, (C) reduced carbon monoxide difference spectrum, and (D) reduced carbon monoxide difference spectrum in the presence of 7 α -hydroxycholest-4-en-3-one.	35
Figure 2.2 Comparisons of WT CYP8B1 (blue) and W281F mutant CYP8B1 (red). A) Structures and names for CYP8B1 substrate and product. Native 7 α -hydroxycholest-4-en-3-one B) binding and C) metabolism to 7 α ,12 α -dihydroxycholest-4-en-3-one. D) Summary of the WT and W281F CYP8B1 7 α -hydroxycholest-4-en-3-one binding and metabolism of 7 α -hydroxycholest-4-en-3-one.	36
Figure 2.3 Substrate binding. Absorbance changes upon titration of the native substrate 7 α -hydroxycholest-4-en-3-one into A) wild type CYP8B1 and B) the CYP8B1 W281F mutant	

were fit to a single-site binding equation to determine the respective C) and D) dissociation constants (K_d values) and maximal absorbance changes.....	37
Figure 2.4 CYP8B1 catalytic activity. Metabolism of 7α -hydroxycholest-4-en-3-one to $7\alpha,12\alpha$ -dihydroxycholest-4-en-3-one by A) wild type CYP8B1 and B) the CYP8B1 W281F mutant.	38
Figure 2.5 CYP8B1 binding of azoles (A) tioconazole, (B) econazole, (C) miconazole, (D) clotrimazole, (E) liarozole, and (F) ketoconazole.....	39
Figure 2.6 CYP8B1 inhibition by azoles (A) tioconazole, (B) econazole, (C) miconazole, (D) clotrimazole, and (E) liarozole.....	41
Figure 2.7 CYP8B1 structure. A) Overview of CYP8B1 (ribbons colored red N-terminus to blue C-terminus) in complex with tioconazole and glycerol (grey sticks). The heme is shown in black sticks with a red sphere for the iron. B) Active site cavity (grey mesh).....	43
Figure 2.8 CYP8B1 active site illustrating A) tioconazole ligand simulated annealing composite omit map and B) residues within 5 Å of tioconazole (sticks). Coloring as in figure 2.7.	44
Figure 2.9 The native 7α-hydroxycholest-4-en-3-one substrate (gray sticks) computationally docked into the CYP8B1 structure (blue ribbons). Heme, black sticks.	46
Figure 2.10 W281F CYP8B1 reduced carbon monoxide difference spectrum (A) in the absence of 7α -hydroxycholest-4-en-3-one and (B) in the presence of 7α -hydroxycholest-4-en-3-one. Compare to the wild type spectra in Figure 2.1.....	48
Figure 2.11 Structural comparisons of CYP8B1 (pale cyan) with CYP8A1 (raspberry) and CYP7A1 (orange). Comparisons of CYP8B1 with CYP8A1 A) overall and B) active sites. Comparisons of CYP8B1 with CYP7A1 C) overall and D) active sites.	52

Figure 2.12 Active site cavities (grey mesh) for A) CYP8A1 (raspberry) and B) CYP7A1 (orange). Heme is shown as black sticks with red sphere for iron.....	54
Figure 3.1 Classic pathway for cholesterol conversion to bile acids.	59
Figure 3.2 Synthesis of three substrate-based 12-pyridine containing steroid analogs as potential inhibitors of CYP8B1. Differences explored include modifications at C3, placement of the double ring $\Delta 4$ in the A ring vs. $\Delta 5$ in the B ring, and modifications of at C17.....	64
Figure 3.3 UV-visible difference spectra for CYP8B1 wild type ligand binding. Spectra for titrations of CYP8B1 wild type with A) 12-pyridyl compound 8 as an example (0.009 μM -79.375 μM) and B) tioconazole (0.000195 μM -8 μM) as positive control.....	65
Figure 3.4 UV-visible absolute spectrum for CYP8B1 wild type tioconazole binding in the presence of 12-pyridyl compounds. Spectrum of CYP8B1 wild type with A) no ligand (black, 421 nm), tioconazole in the presence of 280 μM 12-pyridyl compound 7 (red, 421.5 nm), and tioconazole alone (blue, 424 nm) and B) no ligand (black, 421 nm), tioconazole in the presence of 280 μM 12-pyridyl compound 8 (magenta, 422 nm), and tioconazole alone (blue, 424 nm).....	66
Figure 3.5 Structures of CYP8B1 and 12-pyridyl compound 8. A) Overview of CYP8B1 (ribbons colored red N-terminus to blue C-terminus) in complex with compound 8 (grey sticks). The CYP8B1 heme is shown in black sticks with a red sphere for the iron. B) Simulated annealing composite omit map for compound 8. C) Active site cavity (grey mesh), with circles a-d indicating areas with additional space compared to the complex with tioconazole, with arrows indicating channels opening to the protein exterior and bulk	

solvent. D) The distance between the pyridine nitrogen and the C6 on the opposite side of compound **8** is 8.8 Å. 69

Figure 3.6 UV-visible difference spectra for CYP8B1 W281F mutant binding of compounds

A) 7 (0.15625 μM-360 μM), B) 8 (0.15625 μM-360 μM), and C) 9 (0.15625 μM-120 μM).
..... 71

Figure 3.7 W281F mutant CYP8B1 binding and inhibition by the three different 12-pyridyl

steroids. Absorbance changes for titration of CYP8B1 mutant W281F with A) Compound 7, B) Compound 8, C) Compound 9. D) inhibition of its 7α-hydroxycholest-4-en-3-one 12α-hydroxylation activity by compound 9. E) Summary of the fitted binding affinities (K_d), inhibition at 80 μM concentration of each compound, and the fitted IC₅₀ of compound 9. Assays were performed in triplicate and all data points 72

Figure 3.8 Comparisons of CYP8B1 structures binding 12-pyridyl compound 8 and

tioconazole. The CYP8B1/**8** structure is shown as rainbow-colored ribbons progressing from red N-terminus to blue C-terminus and **8** as grey sticks. The CYP8B1/tioconazole structure is shown in grey ribbons with tioconazole as blue sticks. Heme is in black sticks with red sphere. A) The overview demonstrates the differential placement of tioconazole (blue sticks) binding the heme iron and **8** (grey sticks) 11.2 Å from the iron. B) The backbone of the B' helix (blue) is shifted away from the heme, providing additional space for binding of **8**. C) These two structures reveal differential sides chain rotamers for several residues in the F, G, and I helices and β₄ region surrounding the active site. These include F209, D210, F213, F216, F236, F277, W281 and F482. D) A network between W281, D210, and R479 (dashed lines) that is present when tioconazole is bound is disrupted when **8** binds and the W281 side chain indole flips by 180° 75

Figure 4.1 UV-vis difference spectra for CYP3A7 wild type and hexa-mutant binding of DHEA-S and clotrimazole. A) Titration of DHEA-S with wild type CYP3A7 yields a peak at 388 nm and a trough at 421.5 nm. B) Titration of DHEA-S with the CYP3A7 hexa-mutant yields a peak at 387 nm and a trough at 419 nm. C) Titration of clotrimazole with wild type CYP3A7 yields a peak at 434 nm and a trough at 412 nm. D) Titration of clotrimazole with CYP3A7 hexa-mutant yields a peak at 432 nm and a trough at 412 nm. Representative spectra shown for the triplicate titrations. 88

Figure 4.2 Ligand binding and DHEA-S catalysis for CYP3A7 wild type (red) and hexa-mutant (blue). A) DHEA-S type I binding is conserved but the hexa-mutant is more saturated and has a ~2-fold higher affinity. B) Clotrimazole type II binding is conserved and binds to a similar extent to both enzymes, but has ~2-fold higher affinity for the hexa-mutant. Kinetic parameters of DHEA-S 16 α -hydroxylation by C) wild type and D) hexa-mutant CYP3A7 best fit to the Michaelis-Menten equation with coefficient of determinations (R²) of 0.979 and 0.938, respectively. E) Values for steady-state binding and catalytic parameters with 95% confidence intervals in parenthesis. All experiments were performed in triplicate..... 89

Figure 4.3. DHEA-S metabolism by CYP3A7. Representative MRM chromatograms for DHEA-S (7.5 μ M) (A), its 16 α -hydroxy metabolite (B) and the internal standard estriol 3-sulfate (C) in incubations with the wild type CYP3A7 in the presence and absence of the co-factor NADPH. 91

Figure 4.4 Arrangement of 12 molecules shown in two directions. Each molecule is in a unique color with label in black..... 93

Figure 4.5 Hexa-mutant CYP3A7 structural overview. A) Representative ligand-free molecule with the positions of the K421A/K422A/K424A/R69G/C77G/K244E mutations shown in red sticks. B) Comparison of a ligand-free molecule (yellow ribbons) with a molecule (green ribbons) containing four copies of DHEA-S (shown in sticks with grey carbons). Heme in black sticks with rust sphere for iron..... 95

Figure 4.6 Seven distinct crystal contacts observed in CYP3A7 structure. Interactions between (A) molecule I and J through a salt bridge, (B) molecule E and C through hydrogen bonding, (C) molecule B and A through hydrophobic interactions, (D) molecule L and K through hydrogen bonding, (E) molecule A and J through hydrophobic interactions, (F) molecule B and D through hydrogen bonding, and (G) molecule C and F through a salt bridge. Molecule name is label in black. Secondary structures and residue names are labeled in red. 96

Figure 4.7 Interactions of the DHEA-S substrates (sticks with grey carbons) with the CYP3A7 hexa-mutant (rainbow ribbons from blue N-terminus to red C-terminus). A) Strong electron density (simulated annealing composite omit at 1σ) defines the positioning of all four molecules of the substrate DHEA-S. B) The DHEA-S closest to the heme (DHEA-S1) is oriented with its C17 carbonyl directed toward the heme iron. The second DHEA-S molecule (DHEA-S2) also binds in the active site cavity (grey mesh) but in a different orientation. C) Residues within 4 Å of any of the DHEA-S molecules are shown as sticks, with key sulfate-protein interactions indicated by dashed lines. The sulfate of DHEA-S3 extends to the surface and interacts with Arg243 of a symmetry-related molecule (black sticks). D) Channels from the active site to the protein exterior are indicated by black arrows 1-4. 99

Figure 4.8 Comparisons of CYP3A7 hexamutant structures determined with different liganded states. A) The structure with four DHEA-S molecules bound (green) is quite similar to the previous structure determined with the adventitious ligand dithiothreitol (slate). B) Comparison of the previous dithiothreitol (154 g/mol) complex (slate), the DHEA-S (288 g/mol) complex (green) and the ligand-free structure (yellow) reveal remarkably little changes in active site residue rotamers (DTT not shown). 101

Figure 5.1 Human CYP27A1 purification. CYP27A1 eluted from (A) NiNTA chromatography after a 5 CV 8 mM histidine wash, (B) CM chromatography with a gradient elution, and (C) size exclusion chromatography in tetramers and higher molecular weight oligomers. Pooled fractions in dark purple; absorbance at 417 nm in purple; absorbance at 280 nm in blue.. 114

Figure 5.2 Characterization of recombinant, purified CYP27A1. (A) SDS-PAGE with GroEL and upper-most bands, (B) UV-visible absorbance spectrum, indicating heme incorporation with a Soret λ_{max} at 417 nm, (C) reduced carbon monoxide difference spectrum. 115

Figure 5.3 CYP27A1 ligand binding. Absorbance changes upon titration of the A) clotrimazole and C) 7 α -hydroxycholest-4-en-3-one into CYP27A1 were fit to a single-site binding equation to determine the respective B) and D) dissociation constants (K_d values). 117

Figure 6.1 Structures of potential next-generation CYP8B1 inhibitors. A) Steroid core with an aziridine attached to the C ring. B) Steroid core with a pyridine replacing the C ring.. 125

Abstract

Human cytochrome P450 superfamily are heme-containing monooxygenases. While some cytochrome P450 (CYP) enzymes clear drugs, others are good targets for drug inhibition in various diseases. However, the absence of structural and functional information for three human membrane proteins currently impedes these advances. Inhibition of bile acid-generating CYP8B1 and CYP27A1 are two validated but unrealized approaches to treating nonalcoholic fatty liver disease (NAFLD) and type 2 diabetes or breast cancer, respectively. A third P450, CYP3A7, is important in fetal development and drug clearance in premature infants. The structure/function strategy employed herein is defining atomic-level interactions between these three human P450 enzymes and relevant substrates and inhibitors. X-ray crystallographic structures of CYP8B1 were determined with two different inhibitors, identifying two different binding sites, one as anticipated in the active site, and one unknown one in a channel leading to the active site. This work also identified a Trp281 residue that appears critical for the enzyme's ability to bind such compounds, a hypothesis that was confirmed using mutagenesis. A structure of fetal CYP3A7 with its primary steroidal substrate, dehydroepiandrosterone sulfate, is remarkable in that four copies of the ligand were bound to the protein, something that was entirely unsuspected and leads to further inquiries about the role of this substrate catalysis in normal fetal development. The structural work in this dissertation is supported by binding and enzymatic studies of these two proteins with relevant substrates and inhibitors as well as a second bile acid-generating CYP27A1. This newly-available information correlating structural and functional aspects will advance the development of CYP8B1

and CYP27A1 selective inhibitors, which will be helpful in the design of new therapeutic methods for these human diseases. The corresponding information for CYP3A7 will help predict variable drug clearance and make safer drug dosing guidelines for newborns.

Chapter 1 Introduction

Cytochrome P450 enzymes (CYP450) represent a large and highly diverse family of heme-containing monooxygenases, which are ubiquitously expressed in living organisms. In humans, CYP enzymes play a pivotal role in the metabolism of a wide range of exogenous and endogenous compounds. These enzymes employ a heme prosthetic group as the site of catalysis, enabling them to perform a wide range of physiological functions. The xenobiotic-metabolizing CYP enzymes are involved in the metabolism of many clinically important drugs, toxins, and carcinogens, and contribute significantly to drug dosing, adverse drug-drug interactions, and individual responses to drugs. These CYP enzymes can be considered generalists due to their ability to bind numerous small molecule substrates with relatively low affinity, oxidizing them to products that can be more easily cleared from the body. On the other hand, a second set of CYP enzymes, the endogenous-metabolizing CYP enzymes, specialize in the metabolism of endogenous molecules, such as fatty acids, eicosanoids, steroid hormones, and vitamins. These P450 enzymes play a vital role in maintaining homeostasis. These enzymes have a higher affinity for fewer substrates, making them important targets for pharmaceutical manipulation in specific disease states¹.

Cytochromes P450 enzymes are arranged into families and subfamilies based on amino acid sequence identity. Families share approximately 40% or greater percent identity and are represented with an Arabic number, while subfamilies are represented by capital letters and share 55% amino acid identity. Individual isoforms within a subfamily are specified by a terminal Arabic number. In humans, the 57 P450 enzymes fall into 18 families and 41 subfamilies. Subfamilies often share a major substrate type. The majority of human P450 enzymes primarily act on the

xenobiotic and sterol substrates. Others act on the fatty acid, eicosanoid, and vitamin substrates. A considerable number of P450 enzymes are considered "orphans," as their primary substrate class is unknown². This dissertation focuses on human P450 enzymes from the sterol and xenobiotic substrate classes.

1.1 Cytochrome P450 Spectroscopic Features

Cytochrome P450 enzymes employ a heme prosthetic group at the site of catalysis. This heme group is buried in the center of the enzyme. The iron is coordinated to the nitrogens of the four protoporphyrin pyrrole rings of the heme, as well as a conserved cysteine thiolate in the proximal side of the heme. The UV-visible spectral signals produced by the P450 heme group are unique and are affected by the iron's chemical environment and redox state (Figure 1.1). The Soret band is the most prominent absorbance signal, and it is around 417 nm when the ferric (3+) heme is in a resting state with water coordination to the iron at the 6th coordination site³. The Soret peak shifts to shorter wavelengths (~393 nm) is typically observed when ligands bind in the active site such that they displace the water from the heme iron (type I binding), causing the ferric iron to be in a penta-coordinate, high-spin state. Conversely, a shift to longer wavelengths (~424 nm) is typically observed when ligands not only displace this water but have a ligand nitrogen that coordinates the heme iron (type II binding), causing the iron to be in a hexacoordinate, low-spin state. While the former is often observed for substrates, the latter typically consistent with inhibition since it blocks O₂ binding at this site as required for catalysis. Therefore, these spectral characteristics are often a useful way to determine whether a ligand binds and how a ligand is oriented in the P450 active site with respect to the iron. In addition, monitoring the degree of shift observed during a ligand binding can be used to determine ligand affinity or the dissociation constant (K_d).

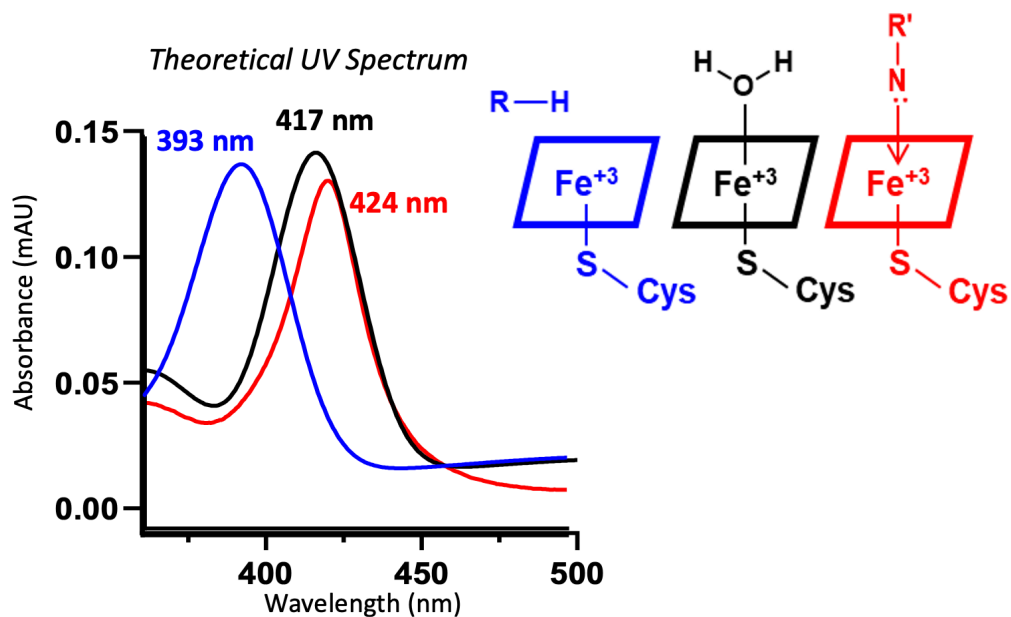


Figure 1.1 Ligand induced spectral shifts in cytochrome P450 enzymes. Ligands can perturb the heme iron coordination state resulting in unique changes to UV-Vis spectral signal. Ligands (denoted as R) can displace a water typically coordinated to the heme in the resting state to cause one of two main spectra (type I: blue, type II: red). (Figure adapted from Alaina Richard)

This Soret band can also be utilized as a valuable indicator of P450 concentration, purity, and stability. The enzyme's concentration can be calculated by measuring the Soret absorbance and applying Beer's law. Similarly, the relative purity can be gauged by examining the ratio of Soret to the total protein absorbance at ~280 nm absorbance. The stability of the P450 enzyme can be evaluated by analyzing its reduced-carbon monoxide difference spectrum. This involves chemically reducing the heme iron from the ferric state (Fe^{3+}) to the ferrous state (Fe^{2+}) in the presence of carbon monoxide⁴. Under these conditions the Soret absorbance red shifts to ~450 nm due to carbon monoxide binding to the heme iron, for which the enzyme superfamily is named (Figure 1.2A). The presence of a peak at 450 nm absorbance is correlated with normal heme coordination, while a peak at 420 nm indicates an issue with the normal heme Fe-proximal interaction (Figure 1.2B). There are two explanations for this P420 in literature. One is that the

proximal cysteine thiolate becomes protonated and dissociates from the heme iron. The other is that this cysteine-Fe interaction is substituted for a histidine-Fe interaction due to some conformational change of the proximal side of the heme⁵. While formation of P420 as historically thought to be an irreversible catalytically inactive form, this is certainly not always the case^{4, 6, 7}.

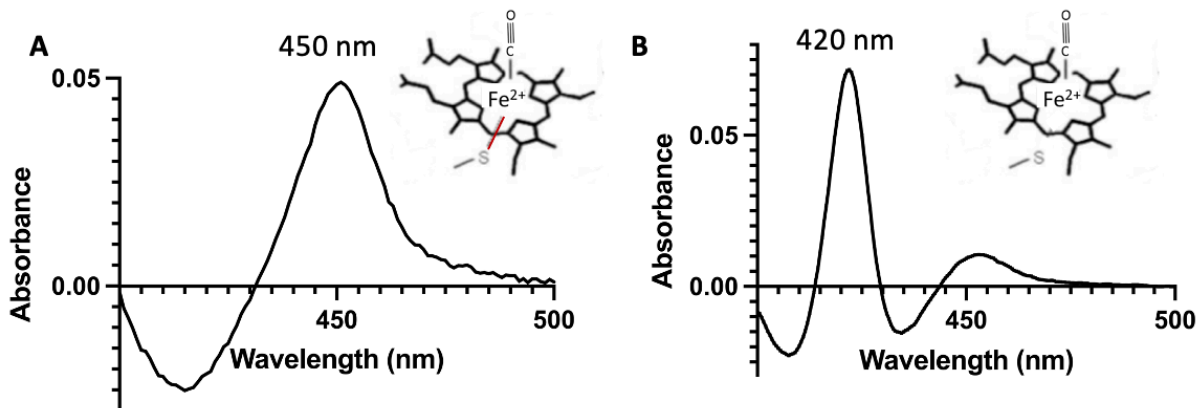


Figure 1.2 Cytochrome P450 CO-difference spectrum. Spectral changes of a P450 enzyme when reduced and bound to carbon monoxide gives characteristic Soret absorbance at A) ~450 nm and B) ~420 nm.

1.2 Cytochrome P450 catalytic Cycle

The cytochrome P450 catalytic cycle can be divided into several distinct steps (Figure 1.3). The first step is typically substrate binding, where the lipophilic substrate enters the enzyme's buried active site and binds in close proximity to the heme iron, displacing the water (type I binding). Then an electron is transferred from NADPH to the heme iron via a redox partner protein, reducing the iron from the ferric (Fe^{3+}) to the ferrous (Fe^{2+}) state. An oxygen molecule then binds to the ferrous heme iron, forming a $\text{Fe}^{2+}\text{-O}_2$ complex. Another electron is transferred from NADPH by a redox partner protein to the $\text{Fe}^{2+}\text{-O}_2$ complex, leading to the formation of a peroxo-ferric species. Subsequently two protonation events occur, first forming a hydroperoxo intermediate (also known as Compound 0), and then a highly reactive ferryl iron-oxo species (also known as

Compound I). Compound I then abstracts hydrogen from the substrate, and oxygen rebound generates the hydroxylated product. The hydroxylated product is released from the active site, allowing a water molecule to bind to the ferric iron (Fe^{3+}), completing the cycle. Besides this hydroxylation reaction, P450 enzymes can also catalyze a variety of other reactions, such as epoxidation, dealkylation, nitrogen oxidation, and lyase activity, which all follow the overall P450 catalytic cycle. In addition to this main productive pathway, P450 enzymes also possess three nonproductive pathways. These nonproductive pathways ultimately restore the ferric P450 state. They use reducing equivalents from NADPH, but no catalytic product is formed. Depending on where they occur in the catalytic cycle, they produce either superoxide, hydrogen peroxide, or extra water (Figure 1.3).

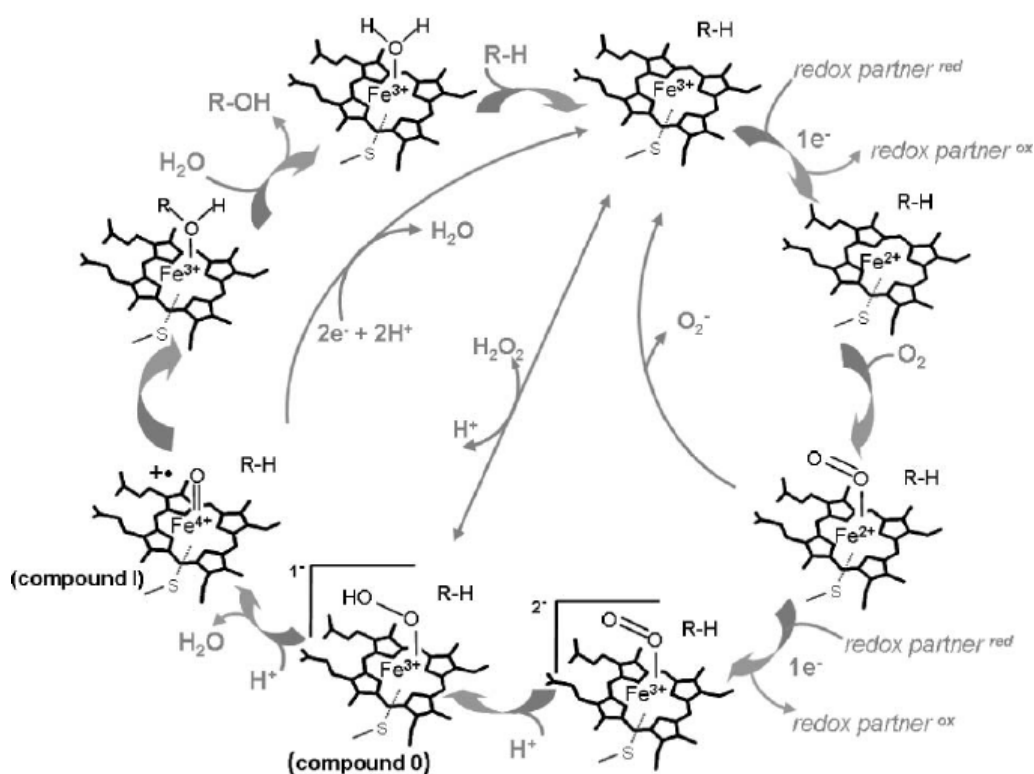


Figure 1.3 Cytochrome P450 catalytic cycle, starting from substrate binding to the heme iron and proceeding clockwise⁸ (with permission). P450 substrate is denoted as R-H, and metabolized product as R-OH.

1.2.1 Cytochrome P450 redox partner

As previously discussed, most P450 enzymes rely on their redox partner proteins to transfer electrons from NADPH, which is essential for their enzymatic reactions. These redox partner systems include either NADPH-cytochrome P450 reductase and/or cytochrome *b*₅ for microsomal P450 enzymes, or adrenodoxin and adrenodoxin reductase for mitochondrial P450 enzymes.

Cytochrome P450 reductase is a key component of microsomal P450 systems, transferring electrons from NADPH to P450 enzymes through its flavin cofactors, flavin adenine dinucleotide (FAD) and flavin mononucleotide (FMN) (Figure 1.4A). The electron transfer process begins with NADPH binding to membrane-bound cytochrome P450 reductase and donating two electrons to the FAD cofactor. One electron at a time is transferred to the cytochrome P450 reductase FMN cofactor before being shuttled to the heme iron of the P450 enzyme. The process occurs twice, with two single-electron transfers, enabling the P450 enzyme to proceed with its catalytic cycle. The FMN cofactor cannot simultaneously accept and donate electron, so cytochrome P450 reductase conformational changes and transient interactions with P450 enzymes are required. In some cases, the second electron (but not the first) can be provided by cytochrome *b*₅, a small membrane-bound heme protein. Although cytochrome *b*₅ is not essential for P450 catalysis, its interaction with P450 can lead to allosteric modulation of P450 activity, affecting catalytic efficiency⁹. It is believed that the binding sites for cytochrome P450 reductase and cytochrome *b*₅ overlap on the proximal side of the P450 enzyme, suggesting that their binding is mutually exclusive.

On the other hand, mitochondrial P450 systems use the adrenodoxin and adrenodoxin reductase (Figure 1.4B). The membrane-bound adrenodoxin reductase accepts two electrons from NADPH, which are transferred to its FAD coenzyme. One electron at a time is then transferred to

the iron-sulfur cluster of the soluble adrenodoxin protein. Adrenodoxin subsequently transfers one electron at a time to the heme iron of the P450 enzyme. Again, two single-electron transfers are required for one P450 catalytic cycle.

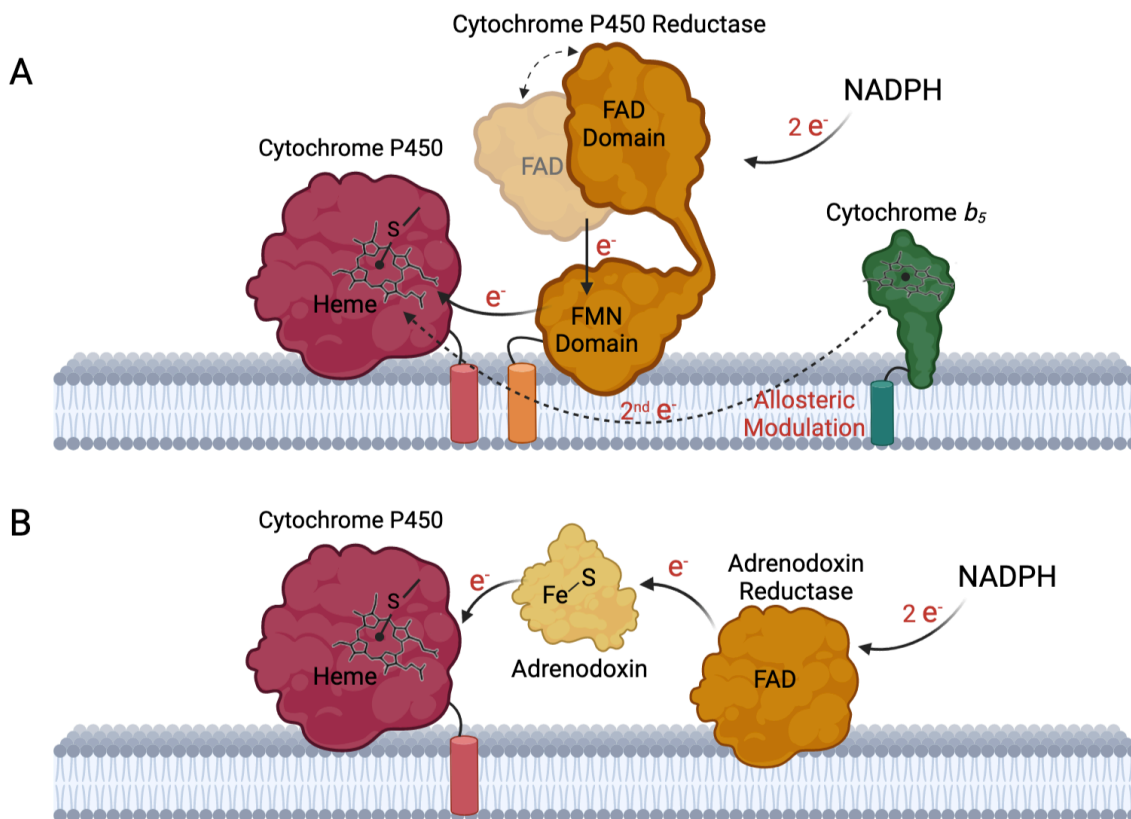


Figure 1.4 The eukaryotic cytochrome P450 system. A) The microsomal P450 enzymes accept two electrons from cytochrome P450 reductase and in some cases cytochrome b_5 . B) The mitochondrial P450 enzymes receive electrons from the adrenodoxin and adrenodoxin reductase system.

1.3 Structure of Cytochrome P450

1.3.1 Structural conservation and diversity

Cytochrome P450 enzymes share a highly conserved single globular domain composed of 12 primary alpha helices (designated A-L), various minor alpha helices (notated with a prime), and four beta-sheet regions (Figure 1.5). The global fold of P450 enzymes forms around the heme prosthetic group, which is located roughly in the enzyme's center, serving as the "floor" of the

active site cavity, and dividing the P450 enzyme into proximal and distal halves (Figure 1.5). The proximal side of the heme is coordinated by a cysteine thiolate, situated in a loop region just prior to the L helix. The P450 redox partner usually binds to the surface of the proximal side of the heme, while substrates enter and bind in the active site on the distal side of the heme (Figure 1.5). The distal side of the heme is bordered by the I helix, which extends through the entire enzyme and contains a generally conserved alcohol/acid residue pair involved in P450 protonation steps. The F/G region forms the distal protein surface, having exterior hydrophobic regions partially embedded into either the endoplasmic reticulum or the mitochondria membrane, which facilitates entry of hydrophobic substrates from the membrane core into the active site cavity. The endoplasmic reticulum-bound enzymes are also anchored to the membrane through an N-terminal helix (Figure 1.5). Both membrane-binding surfaces not only secure the enzyme to the cytosolic face of the endoplasmic reticulum but also influences the substrate access and product egress pathways. This structural conservation of P450 enzymes enables their core catalytic functions.

Despite the conservation of the overall P450 fold, the sequence diversity and differential positioning of secondary structure components within the P450 superfamily give rise to a wide range of accommodated substrates and reactions. The chemical diversity of the F (F'), G (G'), and I helices, and several variable loop regions, such as the B-C loop (sometimes including a short B' helix), particularly contribute to the active site cavity's unique architecture for each enzyme. These structural variations modulate substrate specificity and regioselectivity, thereby increasing the functional diversity of the P450 enzyme superfamily.

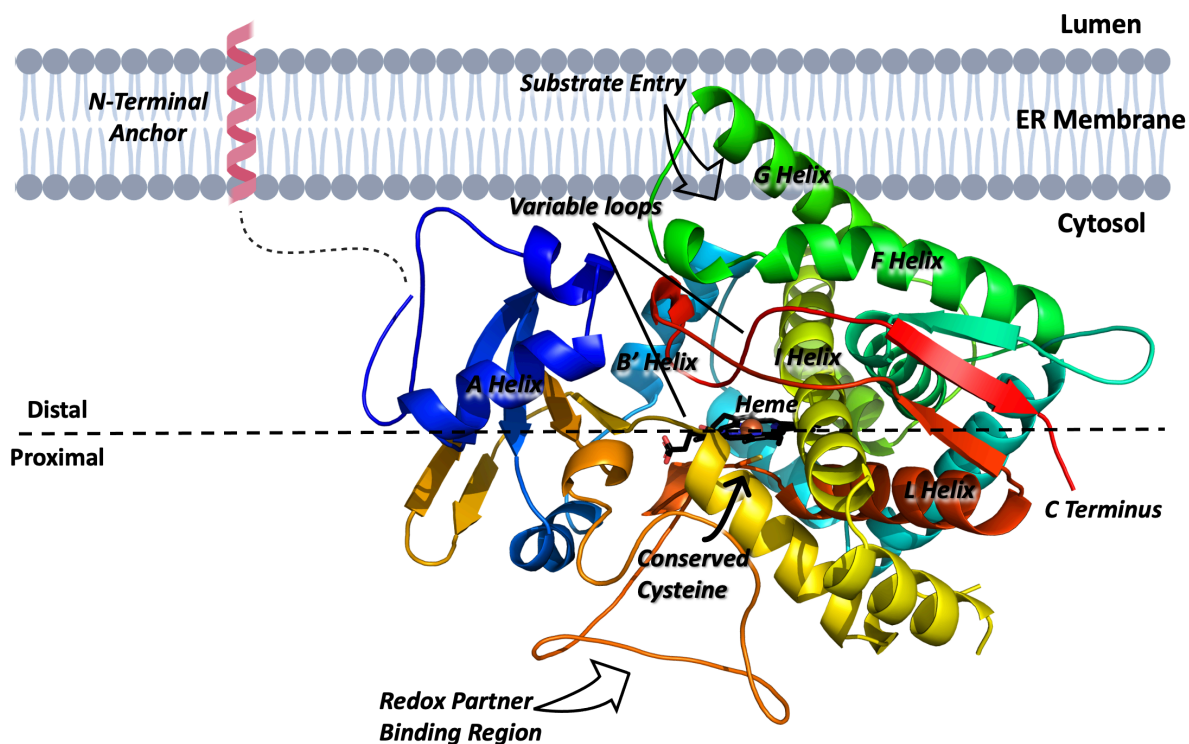


Figure 1.5 Cytochrome P450 global structure. The conserved fold of a human cytochrome P450 enzyme anchored in the endoplasmic reticulum. The P450 enzyme colored pink at the N-terminus through red at the C-terminus. Selected helices, the redox partner binding region, the substrate entry region, and the proximal side and the distal side of the enzyme are labeled.

1.3.2 Conformational Dynamics

P450 enzymes undergo conformational changes to allow ligand access to the active site and product egress. These conformational changes primarily occur in the F/G region associated with the membrane (Figure 1.5, green), leading to the formation of access channels. The F and G helices, which are perpendicular to the I helix, have been implicated in such ligand entry and egress, particularly for hydrophobic substrates which access the buried active site from the membrane-bound face of the catalytic domain. Some human cytochrome P450 enzymes are less promiscuous in terms of the allowable substrates and seem to have less conformational flexibility; this is the case for CYP17A1^{10, 11} and other P450 enzymes that metabolize endogenous substrates. Other human cytochrome P450 enzymes are quite malleable in terms of the active site flexibility.

This allows the promiscuity for a single P450 enzyme to accommodate many different small molecule scaffolds; such is the case for CYP3A4 and other P450 enzymes involved in drug metabolism¹. Thus, understanding dynamic structural changes is crucial for understanding both small molecule binding and egress, as well as elucidating the mechanisms governing substrate specificity and catalytic activity.

1.4 Cytochrome P450 Enzymes Involved in Bile Acids Synthesis

High serum cholesterol has been associated with various disease states such as atherosclerosis, cardiovascular diseases, and liver diseases. The most significant pathway for eliminating cholesterol from the body and maintaining cholesterol homeostasis is the conversion of cholesterol to bile acids in the liver. This pathway is facilitated by five P450 enzymes, namely CYP7A1, CYP7B1, CYP8B1, CYP27A1, and CYP39A1, through two pathways: the classic and alternative pathways (Fig 1.6).

In the classic pathway, CYP7A1 catalyzes the rate-limiting step. It converts cholesterol into 7 α -hydroxycholesterol, which is ultimately metabolized into the primary bile acids cholic acid and chenodeoxycholic acid. CYP8B1, a sterol 12- α -hydroxylase, is responsible for the synthesis of cholic acid and controls the ratio of cholic acid over chenodeoxycholic acid in the bile, adjusting the hydrophobicity of the bile acid pool. In the alternative pathway, CYP27A1 initiates the process by catalyzing the conversion of cholesterol to 27-hydroxycholesterol, which is further metabolized into 3 α ,7 α -dihydroxy-5 β -cholestanoic acid, a precursor to the secondary bile acid, chenodeoxycholic acid. CYP7B1, an oxysterol 7 α -hydroxylase, inactivates oxysterols and converts them to bile salts. It also plays a role in the alternative pathway by catalyzing the conversion of 27-hydroxycholesterol to 7 α ,27-dihydroxycholesterol. Finally, CYP39A1 selectively catalyzes the 7 α -hydroxylation of 24-hydroxycholesterol, a reaction that is important

for maintaining cholesterol homeostasis in the brain. Dysregulation of these enzymes has been associated with several disease states, while some also play unique roles in other physiologically important functions, making them good drug targets.

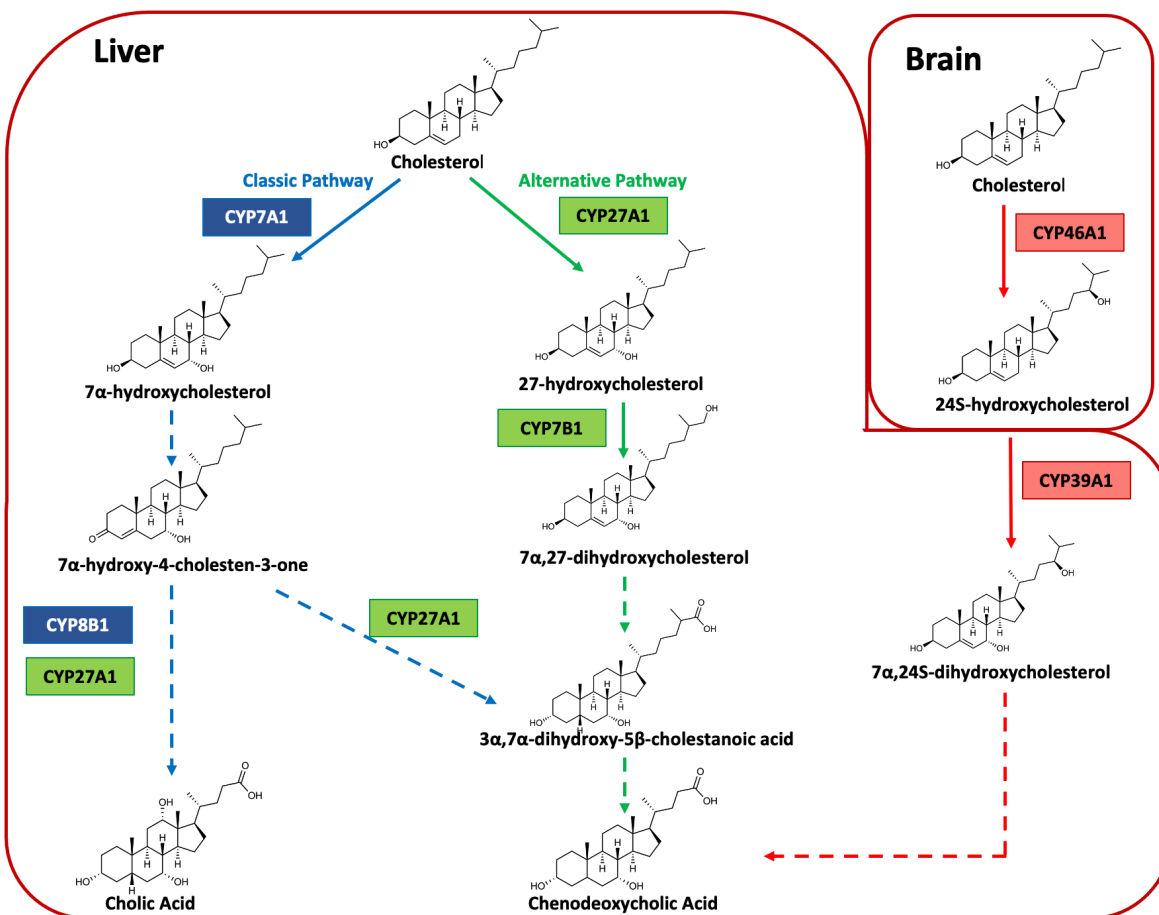


Figure 1.6 Cytochrome P450 enzymes in bile acid synthesis. CYP7A1, CYP7B1, CYP8B1, CYP27A1, and CYP39A1 facilitate cholesterol metabolism through two pathways: the classic and alternative pathways.

This thesis focuses on CYP8B1 and CYP27A1, as dysregulation of these enzymes can lead to several diseases, such as non-alcoholic fatty liver disease, type 2 diabetes, breast cancer, and cerebrotendinous xanthomatosis. Understanding the structure and function of these enzymes can also help in the development of new strategies to treat these human diseases.

1.4.1 Cytochrome P450 8B1

Cytochrome P450 8B1 (CYP8B1), also known as sterol 12 α -hydroxylase, is a protein encoded by the *CYP8B1* gene in humans. CYP8B1 is unique among the CYP family members because it is intronless. This feature simplifies the gene structure, allowing for a more streamlined regulation of its expression. CYP8B1 is primarily localized to the endoplasmic reticulum membrane, where it carries out its catalytic function. The primary function of CYP8B1 is to catalyze the conversion of 7 α -hydroxy-4-cholesten-3-one into 7 α ,12 α -dihydroxy-4-cholesten-3-one (Figure 1.7). This reaction is the major regulator of the balance between the two primary bile acids, cholic acid and chenodeoxycholic acid, which are essential for the emulsification and absorption of dietary lipids. An optimal balance of these two bile acids is essential for maintaining bile acid homeostasis and ensuring the efficient absorption of dietary lipids.

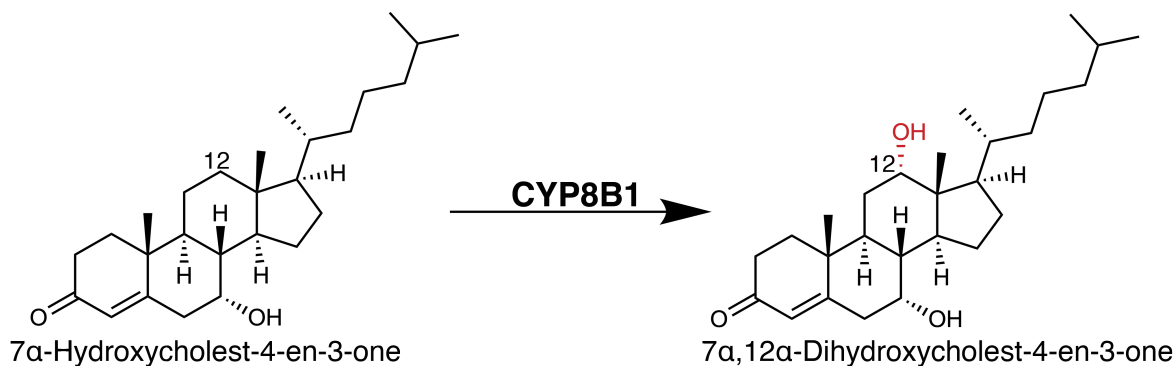


Figure 1.7 Structures and names for CYP8B1 substrate and product. CYP8B1 hydroxylates its substrate at C₁₂ position (red).

The regulation of CYP8B1 activity is a complex process involving feedback mechanisms and various signaling pathways. The enzyme's expression is modulated by several nuclear receptors, including the farnesoid X receptor (FXR) and Hepatocyte nuclear factor 4 α (HNF4 α), which sense changes in bile acid levels and adjust CYP8B1 expression accordingly^{12, 13, 14}. Additionally, bile acids also stimulate the production of inflammatory cytokines in hepatocytes. These cytokines, such as IL-1 β , can subsequently suppress CYP8B1 gene transcription by modulating the nuclear

receptors like HNF4 α . This further refines their role in maintaining bile acid balance and protects the liver during cholestasis¹⁵.

Recent studies have also suggested a potential link between CYP8B1 and chronic liver disease, such as non-alcoholic liver disease (NAFLD) and metabolic disorders, such as obesity and type 2 diabetes¹⁶⁻¹⁸. Altered bile acid composition has been observed in these conditions, with a reduction in CA levels and an increase in CDCA levels. This shift in bile acid composition may impact lipid absorption and metabolism, contributing to the development of liver fat accumulation and metabolic dysfunctions.

CYP8B1 and NAFLD

NAFLD is a common chronic liver disease characterized by a pathophysiological accumulation of lipids in the liver cells, specifically in individuals who consume little or no alcohol. This condition affects a significant proportion of the global population, with prevalence rates varying across different regions and age groups. The disease spectrum can be broadly divided into five stages (Figure 1.8). Simple steatosis (fatty liver) is the earliest and mildest stage of NAFLD, characterized by the accumulation of excess fat (triglycerides) in the liver cells, accounting for more than 5% of the liver's weight¹⁹. At this stage, there is usually no significant inflammation or liver cell damage, and the condition is often asymptomatic. Many individuals with simple steatosis may not progress to more severe stages of NAFLD, particularly if they adopt a healthy lifestyle and manage their underlying risk factors. Non-alcoholic steatohepatitis (NASH) is a more advanced stage of NAFLD in which liver inflammation and liver cell damage occur alongside the accumulation of fat. This stage is marked by the presence of hepatic ballooning, and inflammatory cell infiltration. As a result of chronic liver inflammation and cellular injury in NASH, the liver starts to produce an excess of extracellular matrix proteins, leading to the development of fibrous

scar tissue²⁰. Fibrosis can be graded on a scale of F1 to F4, with F1 indicating mild fibrosis and F4 representing cirrhosis, which is the most advanced stage of NAFLD, characterized by the extensive formation of scar tissue and the disruption of normal liver architecture. Cirrhosis impairs liver function, leading to complications such as portal hypertension, hepatic encephalopathy, and ascites²¹. Patients with cirrhosis are also at an increased risk of developing hepatocellular carcinoma (HCC), a primary liver cancer, which often requires aggressive treatment, including surgical resection, liver transplantation²², or palliative care in advanced cases²³.

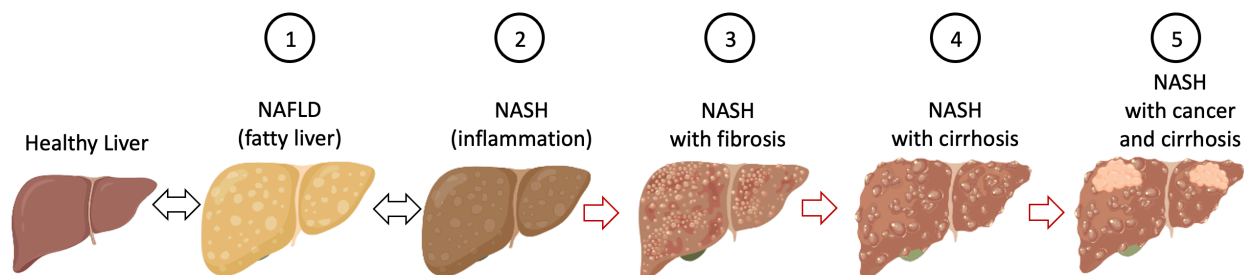


Figure 1.8 NAFLD progression.

NAFLD is closely associated with obesity, insulin resistance, and type 2 diabetes, and is becoming increasingly prevalent worldwide. Recent studies have suggested that dysregulation of CYP8B1 activity may play a critical role in the pathogenesis of NAFLD. For example, it has been shown that the expression of CYP8B1 is upregulated in the livers of patients with NAFLD²⁴, and that inhibition of CYP8B1 activity can ameliorate hepatic steatosis in experimental models of NAFLD¹⁶. Therefore, targeting CYP8B1 may be a promising strategy for the treatment of NAFLD.

CYP8B1 and type 2 diabetes

In addition to its role in the pathogenesis of NAFLD, dysregulation of CYP8B1 activity has also been implicated in the development of type 2 diabetes¹⁸. Type 2 diabetes is a chronic

metabolic disorder characterized by high blood sugar levels (hyperglycemia) resulting from a combination of insulin resistance and inadequate insulin production by the pancreatic β -cells. Insulin is a hormone responsible for regulating blood glucose levels by facilitating glucose uptake into cells to be used for energy or stored for later use. Type 2 diabetes is the most common form of diabetes, accounting for more than 90% of all cases²⁵. While type 2 diabetes can affect people of any age, it is more commonly diagnosed in adults. Several risk factors contribute to the development of type 2 diabetes, including obesity, physical inactivity, family history of diabetes, age, and certain ethnic background. Moreover, individuals with metabolic syndrome, a cluster of conditions including increased blood pressure, high blood sugar, excess body fat around the waist, and abnormal cholesterol or triglyceride levels, are at a higher risk of developing type 2 diabetes²⁶.

Bile acids have been shown to play an important role in glucose homeostasis by activating the farnesoid X receptor (FXR) and the G-protein-coupled receptor TGR5 in the liver and intestine, respectively²⁷. Activation of these receptors leads to increased insulin sensitivity and glucose uptake, and can also suppress gluconeogenesis and promote glucose incorporation into the liver²⁸.²⁹ However, studies have suggested that dysregulation of bile acid synthesis may disrupt these metabolic processes and contribute to the development of insulin resistance and type 2 diabetes. For example, it has been shown that inhibition of CYP8B1 activity can improve glucose tolerance and insulin sensitivity in experimental models of type 2 diabetes³⁰, suggesting that dysregulation of CYP8B1 may contribute to the development of insulin resistance in this disease. Therefore, targeting CYP8B1 may also be a promising strategy for the treatment of type 2 diabetes.

Conclusion

Based on these findings, CYP8B1 has emerged as an attractive therapeutic target for the treatment of NAFLD and type 2 diabetes. However, more research is needed to enable CYP8B1 selective inhibitor design and understand the potential effects of CYP8B1 inhibitors.

Chapter 2 and 3 of this dissertation provide a more comprehensive understanding of CYP8B1 in terms of its protein structure, catalytic function, and ligand binding abilities. Having defined the CYP8B1 active site architecture and identifying features of effective inhibitors should facilitate the identification increasingly selective inhibitors for clinical use. Such inhibitors should both enable a better understanding of the role of CYP8B1 inhibition in normal physiology and provide possible treatments for nonalcoholic fatty liver disease and type 2 diabetes.

1.4.2 Cytochrome P450 27A1

Cytochrome P450 27A1 (CYP27A1), also known as sterol 27-hydroxylase, is a mitochondrial P450 enzyme. It plays a crucial role in the metabolism of cholesterol and other sterols in the body. Specifically, it catalyzes the conversion of cholesterol into 27-hydroxycholesterol, which is then used as a precursor to produce bile acids (Figure 1.6).

Mutations in the CYP27A1 gene are associated with a rare genetic disorder known as cerebrotendinous xanthomatosis. Individuals with cerebrotendinous xanthomatosis have a deficiency in sterol 27-hydroxylase, leading to the accumulation of cholesterol and other sterols in various tissues, including the brain and tendons. This can result in a range of symptoms, including cognitive impairment³¹, ataxia, and tendon xanthomas³².

CYP27A1 and ER α positive breast cancer

Recent studies have also recognized CYP27A1 as a novel drug target for estrogen receptor alpha (ER α) positive breast cancer. ER-positive breast cancer is the most common type of breast

cancer, accounting for approximately 70% of all cases. It is more commonly diagnosed in postmenopausal women but can also occur in premenopausal women. This type of breast cancer tends to grow more slowly than other types and is often sensitive to hormonal therapies, such as selective estrogen receptor modulators (SERMs) and aromatase inhibitors³³. Aromatase inhibitors are the preferred frontline anti-estrogen synthesis drugs in ER α -positive breast cancer, and have shown positive effects, but the relatively rapid development of resistance still hinders durable clinical responses³⁴. This suggests that other estrogen-independent, but possibly ER α -mediated, mechanisms may still promote tumor progression. The CYP27A1 27-hydroxycholesterol product (Figure 1.6) behaves as a selective estrogen receptor modulator. It has agonist activity in breast cancer cells and is capable of promoting the growth of ER-positive tumors³⁵. A study showed that systemic and intratumoral 27-hydroxycholesterol levels and intratumoral CYP27A1 expression levels were elevated in patients with breast cancer³⁴. It is possible that increased intratumoral 27-hydroxycholesterol bypasses the inhibitory effects of aromatase inhibitors. Importantly, 27-hydroxycholesterol is able to act on immune myeloid cells at the distal metastatic sites, creating an immune suppressive environment and promoting breast cancer metastasis³⁶. Inhibition of CYP27A1 significantly reduces metastasis in a mouse model of breast cancer³⁵. Therefore, CYP27A1 is a promising target to prevent tumor progress, resistance, and metastasis in ER α positive breast cancer patients. However, one should balance cancer treatment with the management of symptoms associated with cerebrotendinous xanthomatosis or have a tissue specific delivery to help mitigate the unwanted side effects.

There is no selective inhibitor available for CYP27A and no structure to facilitate such inhibitor design to explore clinical applications. Thus, my goal was to identify CYP27A1 tight-binding ligands, which usually help crystallize P450 enzymes, facilitating the generation of the

first CYP27A1 X-ray structure. This information should promote the design of more selective CYP27A1 inhibitors and allow the exploration of this strategy to treat ER α positive breast cancer.

1.5 CYP3A7 Role in Fetal Development and Xenobiotic Metabolism

Cytochrome P450 enzymes play a pivotal role in the metabolism of a wide variety of endogenous and exogenous compounds. Among these enzymes, the CYP3A subfamily is recognized for its extensive involvement in the biotransformation of drugs and xenobiotics. Notably, CYP3A4 is responsible for the metabolism of approximately 50% of all prescription drugs on the market. This makes it one of the most important drug-metabolizing enzymes in the human body. The broad substrate specificity of CYP3A4 allows it to metabolize drugs from various classes, including but not limited to statins, benzodiazepines, chemotherapeutics, antidepressants, immunosuppressants, and many others³⁷. In addition to inhibition or induction, CYP3A4 is also subject to homotropic cooperativity and heterotropic cooperativity. These mechanisms are forms of allosteric regulation that enhance the catalytic activity of the enzyme. While CYP3A4 has been extensively studied and characterized, another member of the CYP3A subfamily, CYP3A7, remains poorly understood. Despite sharing ~87% sequence identity with CYP3A4, limited research has been conducted on CYP3A7.

CYP3A7 is predominantly expressed in the human fetal liver, with its expression gradually decreasing after birth and being replaced by the more abundant CYP3A4 and CYP3A5 isoforms in adulthood^{38, 39}. The distinct expression pattern of CYP3A7 suggests a specialized role during human development. Recent studies have demonstrated that CYP3A7 is involved in the metabolism of endogenous compounds, such as steroid hormones, which are critical for normal fetal growth and development. Additionally, the enzyme plays a significant role in the biotransformation of exogenous substrates, including various drugs and environmental chemicals.

1.5.1 Steroidogenic pathway and estriol production

CYP3A7 plays a crucial role in the synthesis of estriol, an estrogenic hormone that is predominantly produced during pregnancy. Estriol is one of the three major estrogens, along with estrone and estradiol, and has the weakest estrogenic activity among them⁴⁰. However, its importance lies in its high concentration in maternal circulation during pregnancy, which is indicative of placental and fetal well-being.

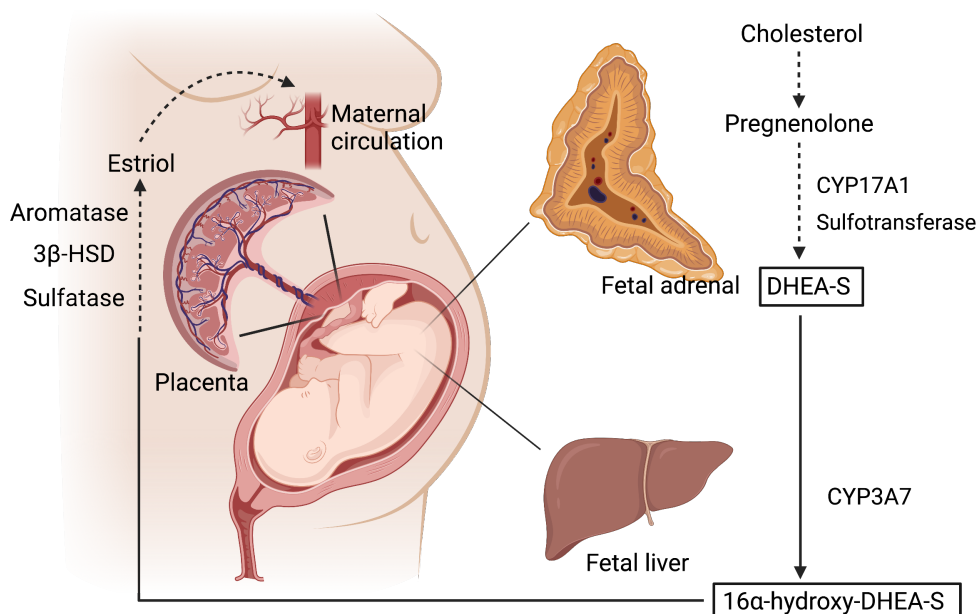


Figure 1.9 Estriol biosynthesis in the human placenta. Dehydroepiandrosterone sulfate (DHEA-S), secreted in prodigious amounts by the fetal adrenal glands, is converted to 16 α -hydroxy-DHEA-S in the fetal liver, which is converted in the placenta to estriol.

Estriol synthesis involves a series of enzymatic reactions that occur primarily in the fetoplacental unit. The fetal liver and the placenta work synergistically to produce estriol from precursors, such as dehydroepiandrosterone 3 sulfate (DHEA-S) and 16 α -hydroxy-DHEA-S, which are mainly derived from the maternal and fetal adrenal glands⁴¹. CYP3A7, specifically expressed in the human fetal liver, catalyzes the 16 α -hydroxylation of DHEAS, converting it to 16 α -hydroxy-DHEAS. This hydroxylated compound then undergoes further metabolism in the

placenta through the action of other enzymes, including 3 β -hydroxysteroid dehydrogenase (3 β -HSD) and aromatase (CYP19A1), resulting in the formation of estriol⁴² (Figure 1.8). The capacity of CYP3A7 to catalyze 16 α -hydroxylation of DHEA-S is considered essential for maintaining the high circulating levels of estriol during pregnancy. Estriol serves as a marker for fetal health⁴³, and its levels are closely monitored throughout pregnancy to detect potential complications, such as placental insufficiency⁴⁴ or intrauterine growth retardation⁴⁵. In addition to its role in estriol synthesis, CYP3A7 is also involved in the metabolism of other steroid hormones, such as progesterone⁴⁶ and testosterone⁴⁷, highlighting its importance in regulating the hormonal balance during fetal development.

1.5.2 Xenobiotic metabolism and drug elimination

CYP3A7, as a member of the CYP3A subfamily, plays a significant role in xenobiotic metabolism and drug elimination, particularly during fetal development. Xenobiotics are foreign substances, including drugs, environmental chemicals, and dietary compounds, that are introduced into the body and require metabolism and elimination to prevent potential toxicity.

CYP enzymes, including CYP3A7, are responsible for phase I metabolism, which involves the oxidation, reduction, or hydrolysis of xenobiotics to form more water-soluble metabolites that can be further processed in phase II metabolism, eventually leading to their elimination from the body. By catalyzing these reactions, CYP3A7 contributes to the detoxification of xenobiotics and plays a crucial role in the fetal defense system against potential teratogens or toxicants⁴⁸.

CYP3A7 exhibits distinct substrate specificity compared to its adult counterparts, CYP3A4 and CYP3A5, which is essential for understanding drug metabolism and disposition during fetal development and in the early stage of life. Studies have shown that CYP3A7 metabolizes several clinically relevant drugs, such as clarithromycin, diltiazem, and nifedipine, although with different

catalytic efficiencies compared to CYP3A4 and CYP3A5⁴⁹. Additionally, CYP3A7 has been reported to metabolize certain environmental chemicals, such as aflatoxin B1⁵⁰ and 6-aminochrysene⁵¹, which underscores its role in protecting the fetus, neonates, and developing infants from harmful exposures. Given this, understanding CYP3A7's role in these processes is critical for developing safe and effective pharmacotherapies for pregnant women and their developing fetuses. For example, in the case of pregnant women with HIV, precise understanding of CYP3A7-mediated drug metabolism can inform the choice of suitable antiviral medications and help optimize dosing schedules during pregnancy. This approach can reduce the risk of mother-to-child HIV transmission while minimizing the chances of adverse drug reactions or ineffective treatment^{52, 53}. Such knowledge is essential in ensuring the health and well-being of both the mother and the unborn child. In addition, underdeveloped pre-term infants are particularly susceptible to fungal infections, necessitating the use of antifungal medications. However, the altered drug metabolism mediated by CYP3A7 can potentially lead to suboptimal treatment outcomes or increased risk of adverse effects⁵⁴. Comprehensive knowledge of CYP3A7-mediated antifungal metabolism is essential for optimizing treatment strategies in this population.

Given the critical role of CYP3A7 in fetal development and fetal and neonatal drug metabolism, chapter 4 of this dissertation provides the atomic-level details of CYP3A7 with DHEA-S, which reveals how CYP3A7 unexpectedly has four binding sites for its native substrate and advances our understanding of this aspect of fetal development. It can also help to discern which small molecules might bind to this enzyme, information which will contribute to our fundamental knowledge to how CYP3A7 binds and metabolizes both endogenous substrates and xenobiotics.

1.6 Conclusions

Cytochrome P450 enzymes are important in two aspects of human health. They play crucial roles in disease physiology, making them ideal targets for novel drug development, and they facilitate the primary step in drug clearance from the body, thereby regulating drug dosage and efficacy. In both contexts, comprehending P450 interactions with drugs at the atomic level using X-ray crystallography is a prerequisite for creating effective new medications. This knowledge sets the foundation for developing innovative therapies for numerous human diseases and enhancing drug treatments for adults, children, and pre-term infants. This deeper understanding of P450 enzymes can lead to safer, more targeted therapies with reduced side effects and improved patient outcomes across various age groups and medical conditions.

Chapter 2 The Structure and Characterization of Human Cytochrome P450 8B1 Supports Future Drug Design for Nonalcoholic Fatty Liver Disease and Diabetes

2.1 Summary

Human cytochrome P450 8B1 (CYP8B1) is involved in the conversion of cholesterol to bile acids. It hydroxylates the steroid ring at C12 to produce the bile acid cholic acid. Previous research has implicated this enzyme as a good drug target for nonalcoholic fatty liver disease and type 2 diabetes, but there are no selective inhibitors known for this enzyme and no structures to guide inhibitor development. Herein, the human CYP8B1 protein was generated and used to identify and characterize a series of azoles, which tend to be poorly selective P450 inhibitors. Structurally-related miconazole, econazole, and tioconazole bound with sub-micromolar dissociation constants and were effective inhibitors of the native reaction. CYP8B1 was co-crystallized with *S*-tioconazole. This inhibitor bound in the active site with its azole nitrogen coordinating the heme iron, consistent with inhibitor binding and inhibition assay data. Additionally, we compared the CYP8B1 active site with similar P450 enzymes to identify features that may facilitate the design of more selective inhibitors. Selective inhibitors could promote a better understanding of the role of CYP8B1 inhibition in these normal physiology and

*The contents of this chapter have been published: **Liu, J.**, Carlson, H.& Scott, E.; The structure and characterization of human cytochrome P450 8B1 supports future drug design for nonalcoholic fatty liver disease and diabetes. *J Biol Chem.* 2022; 298: 102344.

disease states and provide a possible treatment for nonalcoholic fatty liver disease and type 2 diabetes.

2.2 Introduction

Bile acids synthesized in the liver play important roles in normal human physiology and disease. The major human bile acids are cholic acid and chenodeoxycholic acid and their conjugates⁵⁵. All such bile acids are atypical non-planar steroids and amphipathic, with their concave hydrophilic α face dominated by hydroxyl groups and the convex hydrophobic β face projecting methyl groups. Structural variations on this general scaffold result in various bile acids with distinct functionalities. Cholic acid differs from chenodeoxycholic acid in that cholic acid has an additional hydroxyl on the steroidal scaffold. In the classic bile acid synthesis pathway accounting for over 90% of human bile acids, cytochrome P450 8B1 (CYP8B1, sterol 12 α -hydroxylase, E.C.1.14.14.139) installs this hydroxyl on carbon 12 of 7 α -hydroxycholest-4-en-3-one to generate cholic acid⁵⁵. As a result, cholic acid is more polar, while chenodeoxycholic acid is more lipophilic. As a result, CYP8B1 activity controls the ratio of cholic acid to chenodeoxycholic acid and thus the overall hydrophobicity of the bile pool. This hydrophilic/lipophilic balance of bile acids has long been recognized as the major regulator of cholesterol homeostasis and intestinal fat absorption, but these bile acids also have important roles as signaling molecules⁵⁵. Bile acids specifically act on the nuclear farnesoid X receptor and the G protein-coupled bile acid receptor 1⁵⁶. Through these pathways bile acids regulate their own homeostasis, lipid metabolism, glucose homeostasis, and energy expenditure. These capabilities suggested modulation of the bile acid pool as a potential therapeutic strategy for nonalcoholic fatty liver disease (NAFLD) and type 2 diabetes mellitus⁵⁶.

NAFLD is a common disorder in which excess fat accumulates in hepatocytes of individuals who drink little or no alcohol⁵⁷. Associated with obesity, NAFLD can often progress to nonalcoholic steatohepatitis (NASH), fibrosis and cirrhosis requiring liver transplant⁵⁷. In NAFLD patients, cholate-derived bile acids are much higher than chenodeoxycholate-derived bile acids⁵⁸. Cholic acid has the lowest critical micellar concentration (~50 μ M) of all bile acids, is highly efficient for mixed micelle formation with cholesterol and dietary cholesterol absorption⁵⁶. CYP8B1 inhibition would decrease that ratio of the 12 α -hydroxylated or cholic acid bile acids to non-12 α -hydroxylated or chenodeoxycholic acid bile acids. Therefore, the decreased level of cholic acid is expected to result in less intestinal cholesterol and fat absorption. CYP8B1 inhibition would also alter signaling through the farnesoid X nuclear receptor (FXR). Chenodeoxycholic acid is a strong FXR agonist, while cholic acid is weak⁵⁶. In NAFLD, increased chenodeoxycholic acid ratios activate FXR, upregulating genes important for glucose and triglyceride metabolism²⁸. Hepatic FXR activation represses gluconeogenesis and TG synthesis and enhances the free fatty acids (FFAs) β -oxidation and TG clearance²⁸. While a FXR agonist has reduced liver fibrosis⁵⁹ and is under phase III study in patients with NASH⁶⁰, concerns have been raised about FXR effects in other tissues⁶¹. Therefore, it seems likely that tissue specific modulation of FXR would be desirable and CYP8B1 inhibition would accomplish this. Recent mouse *Cyp8b1* knockdown studies also demonstrated significantly decreased steatosis and hepatic lipid content, and a regression in hepatic steatosis⁶². Taken together, CYP8B1 is a potential drug target for NAFLD.

CYP8B1 and type 2 diabetes are connected in two potential ways. First, one study showed that in healthy subjects and type 2 diabetic patients, increased ratio of 12 α -hydroxylated bile acids over non-12 α -hydroxylated bile acids is related to insulin resistance¹⁸. Diabetic mice also exhibit elevated *Cyp8b1* expression⁶³. To evaluate CYP8B1 as a potential therapeutic strategy for

diabetes, knockdown studies were employed⁶⁴. In mice *Cyp8b1* knockdown resulted in increase in free fatty acids in the ileum lumen, increased release of plasma glucagon-like peptide 1 (GLP-1), and improved glucose tolerance, insulin sensitivity, and insulin secretion⁶⁴.

CYP8B1 knockdown using siRNA is a suboptimal therapeutic strategy with substantial delivery difficulties. A more viable strategy would be an orally active small molecule inhibitor selective for CYP8B1. However no selective CYP8B1 inhibitors are currently known. Although Chung et al. recently designed and synthesized a CYP8B1 inhibitor¹⁷, the effectiveness and selectivity of the inhibitor were not determined. Also, there are no CYP8B1 structures to guide such inhibitors development and optimization, which hampers the definition of CYP8B1 roles in both normal physiology and disease states. Identification of a selective CYP8B1 inhibitor is likely to be challenging as one must consider other P450 enzymes, such as CYP8A1 and CYP7A1 with similar amino acid sequences and substrates. The work herein was initiated to support the discovery of selective CYP8B1 inhibitors. To our knowledge this is the first report of generation of purified human CYP8B1^{65,66,67}. This CYP8B1 bound and 12-hydroxylated its native substrate, was used to identify some tight-binding non-selective inhibitors, and to determine the first X-ray structure of this critical human enzyme.

2.3 Experimental Procedures

2.3.1 Expression and purification of CYP8B1 and W281F mutant

The human CYP8B1 cDNA was synthesized with codon optimization for *E. coli* expression (Genscript, Piscataway, NJ). Nucleotides coding for wild type amino acids 1-25 composing the transmembrane helix were truncated and replaced with nucleotides coding for the sequence MAKKTSS. Nucleotides were also added at the C-terminus to code for a six-residue histidine tag

just prior to the stop codon. The resulting sequence was cloned into the pCWori+ vector. For the mutant, an extra mutation W281F was made.

Wild type and W281F expression plasmids were transformed into *E. coli* DH5a cells already containing the pGro7 plasmid for expressing the GroES-GroEL chaperone complex (Takara Bio, San Jose, CA) and plated on a lysogeny broth (LB) agar plate containing 100 µg/ml carbenicillin for pCWori+ selection and 20 µg/ml chloramphenicol for pGro7 selection and grown at 37 °C overnight. A single colony was then inoculated into 5 mL LB media with the same antibiotics and grown for 6-8 hours at 37 °C with shaking. A 50 µL sample of this culture was then introduced into 200 mL LB media and grown overnight with the same antibiotics, with shaking at 37 °C. For expression 900 ml of terrific broth (TB) with 2× potassium phosphate buffer and the same antibiotics in a 2.8-liter Fernbach flask were inoculated with 20 ml of the overnight culture. This culture was incubated at 37 °C and 220 rpm until an optical density at 600 nm (O.D.₆₀₀) of 0.4–0.6 was reached. At that point, 1 mM δ-aminolevulinic acid and 4 mg/mL arabinose were added as a heme precursor and to induce expression of the *groES-groEL* genes, respectively. When an O.D.₆₀₀ of 0.8 was reached, CYP8B1 expression was induced with 1 mM isopropyl β-D-1-thiogalactopyranoside. The temperature and shaking were reduced to 25 °C and 190 rpm for 48-66 hours, after which bacterial cells were pelleted by centrifugation at 6,930 x g at 4 °C for 10 min. The cell pellet was resuspended in resuspension buffer (500 mM potassium phosphate buffer, pH 7.4, 20% (v/v) glycerol, 500 mM sodium chloride) containing 2 tablets of 0.8 x SigmaFast protease inhibitor (Millipore Sigma, St. Louis, MO). The resuspended sample was homogenized using a Dounce homogenizer with pestle A followed by pestle B. Lysozyme was added to 0.3 mg/ml. Cells were then disrupted by ultrasonication (Fisher Scientific Sonic Dismembrator Model 100) 10 times for 30 seconds with 30 seconds interval between every two sonication periods.

CYP8B1 was extracted with 14 mM 3-[(3-cholamidopropyl)dimethyl-ammonio]-1-propane sulfonate (CHAPS) (GoldBio, Saint Louis, MO) for 1 hour at 4 °C. Cell debris and membranes were removed by ultracentrifugation at 12,000 x g for 50 min at 4 °C. The resulting supernatant was loaded on a 30 mL Ni-NTA column (Ni/NTA Superflow, Qiagen, Germantown, MD) equilibrated with 2 column volumes (CV) of loading buffer (100 mM potassium phosphate buffer, pH 7.4, 500 mM NaCl, 20% (v/v) glycerol, 14 mM CHAPS). After loading, the column was first washed with 5 CV loading buffer, followed by 5 CV Ni-NTA wash buffer (100 mM potassium phosphate buffer, pH 7.4, 500 mM NaCl, 20% (v/v) glycerol, 14 mM CHAPS, 5.6 mM histidine) to remove weakly bound contaminants. CYP8B1 was then eluted with 6 CV Ni-NTA elution buffer (10 mM potassium phosphate, pH 7.4, 100 mM NaCl, 20% (v/v) glycerol, 10 mM CHAPS, 80 mM histidine). The eluted CYP8B1 fractions typically had a ratio of absorbance at 420 vs. 280 of 0.7, which were pooled and concentrated to 20-50 mL using an Amicon ultra 50-kDa filter and then diluted 6-fold with CM wash buffer (5 mM potassium phosphate, pH 7.4, 20% (v/v) glycerol, 1 mM ethylenediaminetetraacetic acid (EDTA)) containing 4 mM CHAPS. Two 5 mL HiTrap CM FF column (GE Healthcare) were connected in series for cation-exchange chromatography (total CV=10 mL). Columns were equilibrated with 5 CV CM wash buffer. After loading, these columns were washed with 10 CV CM wash buffer and CYP8B1 subsequently eluted with a gradient from 0 to 500 mM NaCl formed by the CM wash buffer and CM elution buffer (50 mM potassium phosphate, pH 7.4, 50 mM NaCl, 20% (v/v) glycerol, 1 mM EDTA). Fractions with at least equal absorbance at 280 and 420 nm were pooled and concentrated to 1-2 mL using an Amicon ultra 50 kDa filter before injecting onto a size exclusion column (GE Healthcare HiLoad® 16/60 Superdex® 200 pg). This column was equilibrated and run with CM elution buffer. Fractions with at least equal absorbance at 280 and 420 nm were pooled. The purity of the protein was

examined by measuring the ratio of the absorbance of Soret peak vs. the absorbance at 280 nm (typically 1.0) and by SDS-PAGE with a single band. Purified CYP8B1 was also characterized using by UV-visible absorbance spectrum and reduced carbon monoxide-difference spectrum.

2.3.2 Human cytochrome P450 reductase

The human full-length cytochrome P450 reductase with K59Q mutation was synthesized with codon optimization for *E. coli* expression (Genscript). A six-residue histidine tag was added at the C-terminus just prior to the stop codon. This modified cDNA was cloned into pET29a(+) vector, and transformed into *E. coli* C41(DE3)/pGro7 cells. The protein was expressed and purified as described⁶⁸ except that cells were lysed by a homogenizer (Avestin, Inc. EmulsiFlex-C3 High Pressure Homogenizer) instead of a French press.

2.3.3 Crystallization and structural determination

CYP8B1 (10 mg/mL) in CM elution buffer (50 mM potassium phosphate, pH 7.4, 50 mM NaCl, 20% (v/v) glycerol, 1 mM EDTA) was saturated with 30 μ M tioconazole as evidenced by a shift of the Soret peak to 425 nm. CYP8B1 crystals were grown using sitting drop vapor diffusion equilibration. The CYP8B1/tioconazole complex was equilibrated against 5% 2-methyl-2,4-pentanediol, 0.1 HEPES pH 7.5, 10% PEG 10,000 at 25 °C. Crystals formed within 24 hr. Crystals were cryoprotected with mother liquor plus 30% glycerol and flash cooled in liquid nitrogen. Diffraction data were collected on beamline 21-ID-G of the Advanced Photon Source and processed using HKL 2000⁶⁹. The CYP8B1 structure was solved by molecular replacement using Phaser⁷⁰ with a CYP8A1 search model (PDB entry 2IAG). Model building and refinement were performed iteratively with Coot⁷¹ and Phenix.refine⁷², respectively. The ligand (*S*)-tioconazole was generated using elBOW⁷³ in Phenix. Active site void volumes were calculated using

VOIDOO⁷⁴, with probe radius = 1.4 Å and grid spacing of 1.0. Figures were generated with PyMOL⁷⁵.

2.3.4 Ligand binding assay

Ligand binding affinities were determined by observing shifts in the CYP8B1 (in 50 mM potassium phosphate, 20% glycerol) absorbance spectrum as described previously⁵⁴. Clotrimazole, ketoconazole, and liarozole (dissolved in DMSO) were titrated into 1 μM CYP8B1 in a cuvette with 1 cm path length. Because of their higher affinities, econazole, tioconazole, and miconazole (dissolved in DMSO) were titrated into 0.2 μM CYP8B1, and the 7α-hydroxy-4-cholesten-3-one substrate (dissolved in ethanol) was titrated into 0.1 μM CYP8B1 or CYP8B1 W281F in a cuvette with 5 cm path length to increase signal to noise. Changes in absorbance (local absorbance maximum minus minimum) were plotted against ligand concentration and analyzed using the single-site specific binding equation using GraphPad Prism version 8.0.0 for Mac OS X (GraphPad Software, San Diego, CA USA). All titration experiments were repeated in triplicate.

2.3.5 Determination of kinetic parameters

To determine the steady-state kinetic parameters of CYP8B1 and CYP8B1 W281F for 12α-hydroxylation of its native substrate 7α-hydroxycholest-4-en-3-one, *in vitro* activity assays were conducted. A total reaction volume of 1 mL (for WT CYP8B1) or 0.5 mL (for CYP8B1 W281F) contained 0.01 μM CYP8B1 (WT and mutant) and 0.06 μM human cytochrome P450 reductase in 50 mM potassium phosphate buffer, pH 7.4 containing 20% glycerol. CYP8B1 and reductase were mixed and preincubated for 10 min at room temperature before adding 7α-hydroxycholest-4-en-3-one (0.01-10 μM, dissolved in ethanol; total of 0.2% ethanol). Reactions were initiated by the

addition of 200 μ M NADPH and allowed to proceed at 37 °C for 1.5 min (for WT) or 2 min (for CYP8B1 W281F) and terminated with the addition of 1 mL chloroform. For all reactions substrate utilization was within 10%. The internal standard of 40 μ M 11-deoxycortisol (dissolved in DMSO) was added to all reactions. Sterols were extracted twice with 1 mL (for the WT) or 0.5 mL (for the mutant) chloroform, dried under the hood, resuspended in 100 μ L 40% acetonitrile, and injected (60 μ L for WT, 30 μ L for the mutant) onto a reverse-phase HPLC column (Phenomenex, Torrance, CA, Luna®, 5 μ m, C18, 150 x 4.6 mm). Chromatography was performed at 40 °C with a flow rate of 0.8 mL/min using an acetonitrile-water gradient (Phase A: 10% acetonitrile, Phase B: 100% acetonitrile). The following method was used: 0-15 min 40% B, 15-45 min 80% B. Sterols were detected by UV absorbance at 240 nm. Retention times of the internal standard, product, and substrate were: 11-deoxycortisol (internal standard) at 9.9 min, 7 α ,12 α -dihydroxycholest-4-en-3-one at 24.5 min, and 7 α -hydroxycholest-4-en-3-one at 39.5 min. Quantification of the product 7 α ,12 α -dihydroxycholest-4-en-3-one was performed by determining the ratio of the peak area for the product over the peak area of the internal standard using a calibration curve. Initial reaction velocities were plotted against the respective 7 α ,12 α -dihydroxycholest-4-en-3-one concentration and fit to the Michaelis-Menten equation using GraphPad Prism version 8.0.0 for Mac OS X (GraphPad Software, San Diego, CA USA). These experiments were performed in triplicate.

2.3.6 CYP8B1 inhibition assays

Potential inhibitors were initially screened by adding a fixed concentration of 80 μ M to the assays described above and determining the % activity remaining compared to a control reaction without inhibitor. These experiments were performed in duplicate or triplicate.

Subsequently the concentration of azoles leading to 50% inhibition (IC₅₀) of 7 α -hydroxycholest-4-en-3-one metabolism by CYP8B1 was determined. These assays were conducted as described

above with the following modifications: 1) the concentration of the substrate 7α -hydroxycholest-4-en-3-one was held constant at the K_m of 0.5 μ M, 2) inhibitors (dissolved in DMSO) were added at increasing concentrations, 3) the reaction volume was decreased to 500 μ L, 4) the reaction time was increased to 2 min. Quantification of sterol products was also conducted as described in kinetic assay section except that 1) 30 μ L of each sample was injected onto the column and 2) the methods/mobile phases had to be optimized to improve separation of inhibitors other than liarozole. The method for tioconazole was as follows: 0-12 min 40% B, 12-42 min 40-80% B, 42-70 min 80% B, 70-75 min 40% B. For econazole and clotrimazole, the method was as follows: 0-12 min 40% B, 12-52 min 40-80% B, 52-75 min 80% B, 75-80 min 40% B. For miconazole, same method was used, but 10% acetonitrile with 0.03% acetic acid was substituted for 10% acetonitrile for A. The amount of the $7\alpha,12\alpha$ -dihydroxycholest-4-en-3-one product produced with no inhibitor present was set as 100% maximal activity. The amounts of the product produced in the inhibitor-containing samples were scaled to this value and reported as percentages of the maximal activity. These percentages were then plotted against the log inhibitor concentration in GraphPad Prism and fit to the log[inhibitor] vs. response, 4 parameter variable slope equation. These experiments were repeated in triplicate.

2.3.7 Docking 7α -hydroxycholest-4-en-3-one into the CYP8B1 active site

Maestro V.2021-3 and the OPLS4 force field⁷⁶ were used to execute system preparation and the docking protocol. The dielectric constant was set to 1.0. The native substrate 7α -hydroxycholest-4-en-3-one was built and minimized, then prepared with the LigPrep module. The complex of CYP8B1 with *S*-tioconazole bound was stripped of waters and the glycerol molecule. The complex was set up using the Protein Preparation Workflow with the choice to cap all residues at sequence gaps. All hydrogens were minimized while the other atoms were held fixed. The

system was then minimized with the ligand and all residues within 5 Å being free to move. The free residues were surrounded by a 5-Å shell of residues that were constrained with a force constant of 200 kcal/mol•Å². The rest of the protein was held fixed. After this minimization, a 10-Å docking box was centered on *S*-tioconazole. A receptor grid was generated from this structure. The induced-fit docking area was defined by the central atom of *S*-tioconazole. The ligand was then removed and induced-fit docking⁷⁷ was executed with the Glide XP⁷⁸ protocol using default parameters. Residues within 5 Å were refined during the docking of 7 α -hydroxycholest-4-en-3-one. A pose with C12 oriented toward the heme group was the 4th unique pose and had a score of -8.6 kcal/mol. Better scored poses were in unproductive orientations with the A ring's ketone toward the heme and the flexible C17 tail pointed up filling the area occupied by the removed glycerol additive.

2.4 Results

2.4.1 Generation of Recombinant CYP8B1

To generate recombinant CYP8B1 a synthetic cDNA was designed. Most microsomal human cytochrome P450 enzymes have an N-terminal transmembrane helix and hydropathy plot analysis indicated this was likely the case for CYP8B1. As truncation of this hydrophobic sequence typically increases expression and increases solubility favorable for crystallization, the N-terminal 25 amino acids were removed and replaced by a sequence coding for MAKKTSS. Additionally, a sequence coding for a 6-residue histidine tag was appended to the C-terminus. The entire gene was codon-optimized and subcloned into the pCWori+ vector for *E. coli* expression. As is typical for membrane P450 enzymes, the resulting CYP8B1 protein was membrane-bound, likely via a typical secondary membrane-binding site. Thus, addition of detergent was used to solubilize CYP8B1. A three-column purification protocol was developed yielding highly purified protein,

as indicated by SDS-PAGE (Figure 2.1A), which eluted as a monomer on size exclusion chromatography (data not shown). The resulting CYP8B1 protein demonstrated a heme Soret peak with a maximum absorbance at 420 nm (Figure 2.1B). This absorbance profile is consistent with water coordination of the heme iron in the active site. When the protein is reduced and exposed to carbon monoxide, the difference spectrum showed much greater absorbance at 420 nm compared to the absorbance at 450 nm (Figure 2.1C). This was initially concerning given that the 450 nm absorbance is correlated with a catalytically-active form of the enzyme, while 420 nm is sometimes, correlated with an inactive form of cytochrome P450 proteins though this is not consistent between P450 enzymes and can be reversible^{4,6,7}. However, when substrate was added to CYP8B1, the same reduced-carbon monoxide difference spectrum displayed only absorbance at 450 nm (Figure 2.1D). Thus, the presence of substrate appeared to alter the enzyme heme environment toward a state that is typically active. Nonetheless, because of this result it was particularly important to determine if the enzyme could bind ligands and perform catalysis normally.

2.4.2 CYP8B1 Substrate Binding

As is typical for cytochrome P450 enzymes, the ability to bind ligands was evaluated by determining shifts of the heme Soret peak from the initial value. A shift to shorter wavelengths is typically observed when ligands bind in the active site such that they displace a water from the heme iron (type I binding). Conversely, a shift to longer wavelengths is typically observed when ligands not only displace this water but have a ligand nitrogen that coordinates the heme iron (type II binding). While the former is often observed for substrates, the latter typically consistent with inhibition since it blocks O₂ binding at this site as required for catalysis.

Titration of CYP8B1 with its native substrate 7α -hydroxycholest-4-en-3-one (Figure 2.2 A) did yield the expected blue shift in absorbance. The difference spectra indicated decreases in absorbance at 427 nm and increasing absorbance at 392 nm (Figure 2.3), consistent with a type I interaction. Plotting the changes in absorbance vs. ligand concentration revealed that the dissociation constant (K_d) value for this substrate was 18.0 nM (95% CI: 14.9-21.8 nM) (Figure 2.2B, blue). This value is consistent with high affinity of CYP8B1 for its native substrate.

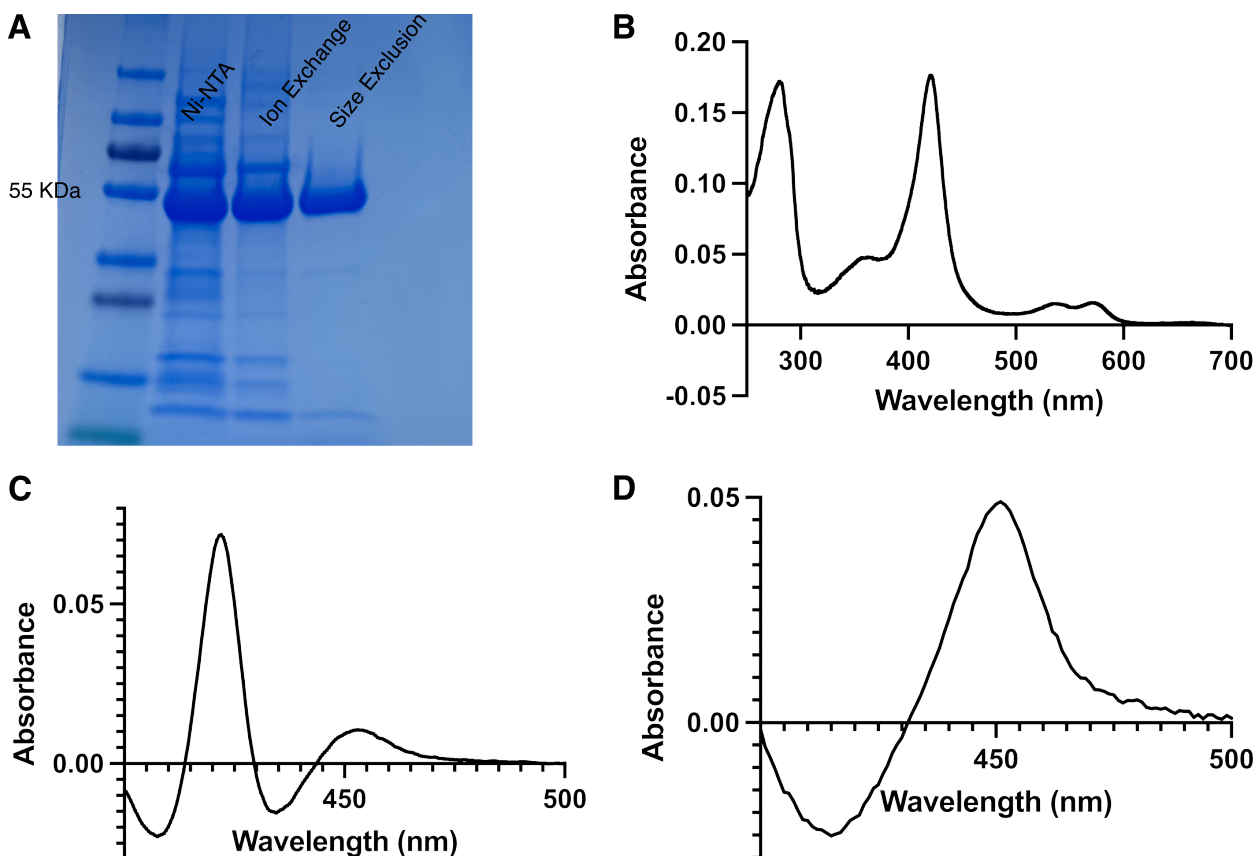


Figure 2.1 Characterization of recombinant, purified wild type CYP8B1. (A) SDS-PAGE, (B) UV-visible absorbance spectrum, indicating heme incorporation with a Soret λ_{\max} at 420 nm, (C) reduced carbon monoxide difference spectrum, and (D) reduced carbon monoxide difference spectrum in the presence of 7α -hydroxycholest-4-en-3-one. *CYP8B1 Catalysis*

CYP8B1 hydroxylates C12 of 7α -hydroxy-4-en-3-one to form $7\alpha,12\alpha$ -dihydroxycholest-4-en-3-one (Figure 2.2 A). The recombinant CYP8B1 herein was able to perform this reaction (Figure

2.2 C, blue, Figure 2.4) with a K_m of 0.5 μM (95% CI 0.4-0.6 μM) and a k_{cat} of 7.4 min^{-1} (95% CI 6.8-8.0 min^{-1}). The resulting CYP8B1 catalytic efficiency (k_{cat}/K_m) is 14.7 ($\mu\text{M} \cdot \text{min}$) $^{-1}$.

2.4.4 Recombinant CYP8B1 W281F Substrate Binding and Catalysis

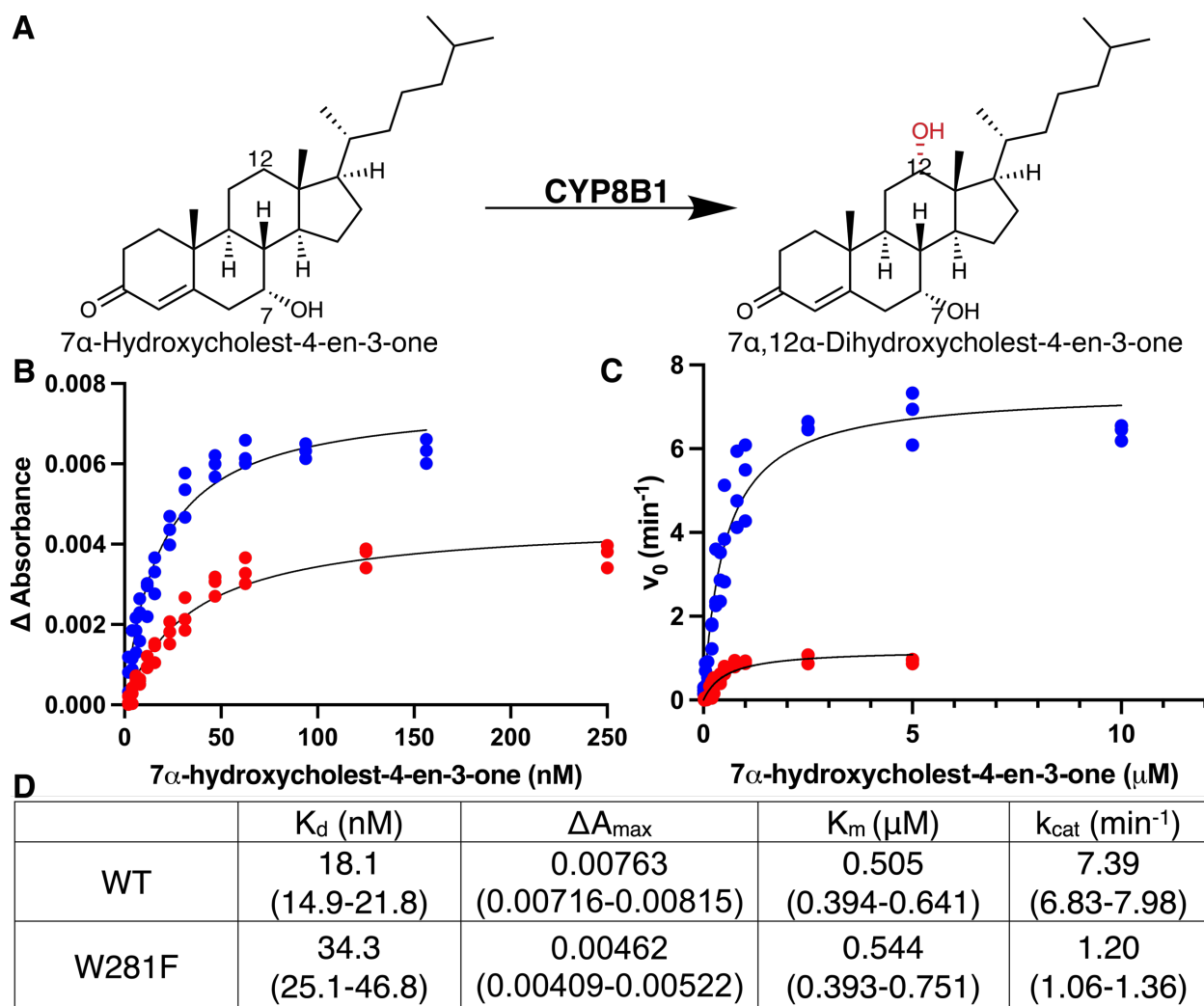


Figure 2.2 Comparisons of WT CYP8B1 (blue) and W281F mutant CYP8B1 (red). A) Structures and names for CYP8B1 substrate and product. Native 7 α -hydroxycholest-4-en-3-one B) binding and C) metabolism to 7 α ,12 α -dihydroxycholest-4-en-3-one. D) Summary of the WT and W281F CYP8B1 7 α -hydroxycholest-4-en-3-one binding and metabolism of 7 α -hydroxycholest-4-en-3-one. Tryptophan 281 in CYP8B1 may be important for the proper protein

function. In CYP7A1 the when the corresponding conserved active site tryptophan (W284 in substrate recognition site 4⁷⁹ or SRS-4 in the I helix) was mutated to phenylalanine, the spectral

shift in response to cholesterol binding was abolished⁸⁰. To investigate the role of W281, CYP8B1 with a W281F mutation was recombinantly generated, expressed, and purified the same way as wild type CYP8B1. This CYP8B1 W281F mutant still bound the native substrate 7 α -hydroxy-4-en-3-one with the same spectral shift as the wild type enzyme (Figure 2.3). However, compared to wild type protein, the W281F mutant demonstrated both lower affinity in the form of a 2-fold higher K_d value (34.3 nM (95% CI 25.1-46.8 nM) and a decreased population of CYP8B1 binding substrate at saturation in the form of a close to 2-fold decrease in A_{max} value (Figure 2.2 B, red; Figure 2.2 D).

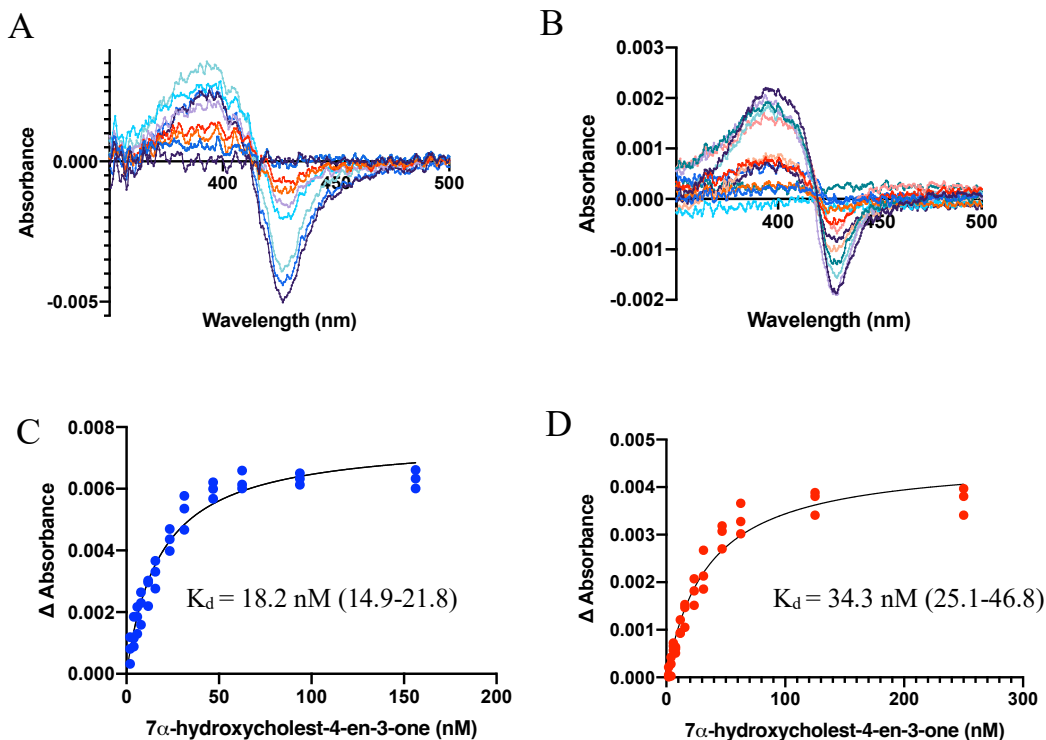


Figure 2.3 Substrate binding. Absorbance changes upon titration of the native substrate 7 α -hydroxycholest-4-en-3-one into A) wild type CYP8B1 and B) the CYP8B1 W281F mutant were fit to a single-site binding equation to determine the respective C) and D) dissociation constants (K_d values) and maximal absorbance changes.

The W281F mutant CYP8B1 was able to convert 7 α -hydroxy-4-en-3-one to 7 α ,12 α -dihydroxy-4-en-3-one (Figure 2.2C, red; Figure 2.4). The K_m for this reaction was 0.54 μ M (95%

CI 0.39-0.75 μM) (Figure 2.2D), which is similar with the K_m of wild type CYP8B1. However, the k_{cat} value for W281F was 1.20 min^{-1} , which is less than one-sixth of the wild type protein. The catalytic efficiency was thus correspondingly reduced more than six-fold to 2.2 ($\mu\text{M}\cdot\text{min}$) $^{-1}$. Altogether, these results confirm that W281 is important in substrate binding and catalysis.

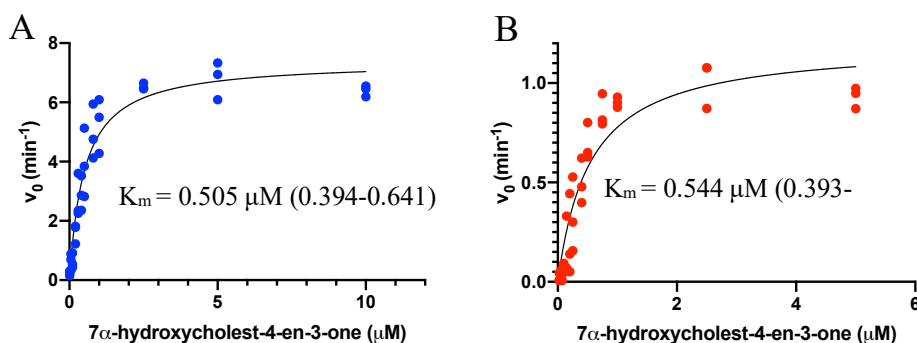


Figure 2.4 CYP8B1 catalytic activity. Metabolism of 7 α -hydroxycholest-4-en-3-one to 7 α ,12 α -dihydroxycholest-4-en-3-one by A) wild type CYP8B1 and B) the CYP8B1 W281F mutant.

2.4.5 CYP8B1 Inhibitor Binding

Since specific inhibitors of CYP8B1 have the potential to be valuable clinically but are largely unknown, an initial strategy was to evaluate the ability of CYP8B1 to bind several non-specific P450 inhibitors containing azole groups, which can often coordinate the heme iron with high affinity. A number of these are commercially available and target other P450 enzymes as clinically useful antifungals (fluconazole, econazole, clotrimazole, miconazole, tioconazole, ketoconazole) or retinoic acid metabolism blocking agents (liarozole). While addition of the triazole-containing fluconazole did not induce a shift of the CYP8B1 Soret peak and thus may not bind, all of the other drugs listed above contain imidazoles and shifted the Soret peak to longer wavelengths (424.5-425.5 nm, type II binding), consistent with an interaction between the CYP8B1 active site heme Fe and the ligand nitrogen. Titrations with each compound were consistent with single site binding with dissociation constants ranging from 60-210 nM for econazole, miconazole, and tioconazole up to 1.3-1.6 μM for clotrimazole, liarozole, and ketoconazole (Table 2.1, Figure 2.5). These

results not only indicated that CYP8B1 can interact typically with type II imidazole-containing ligands, but that it can do so with relatively high affinities.

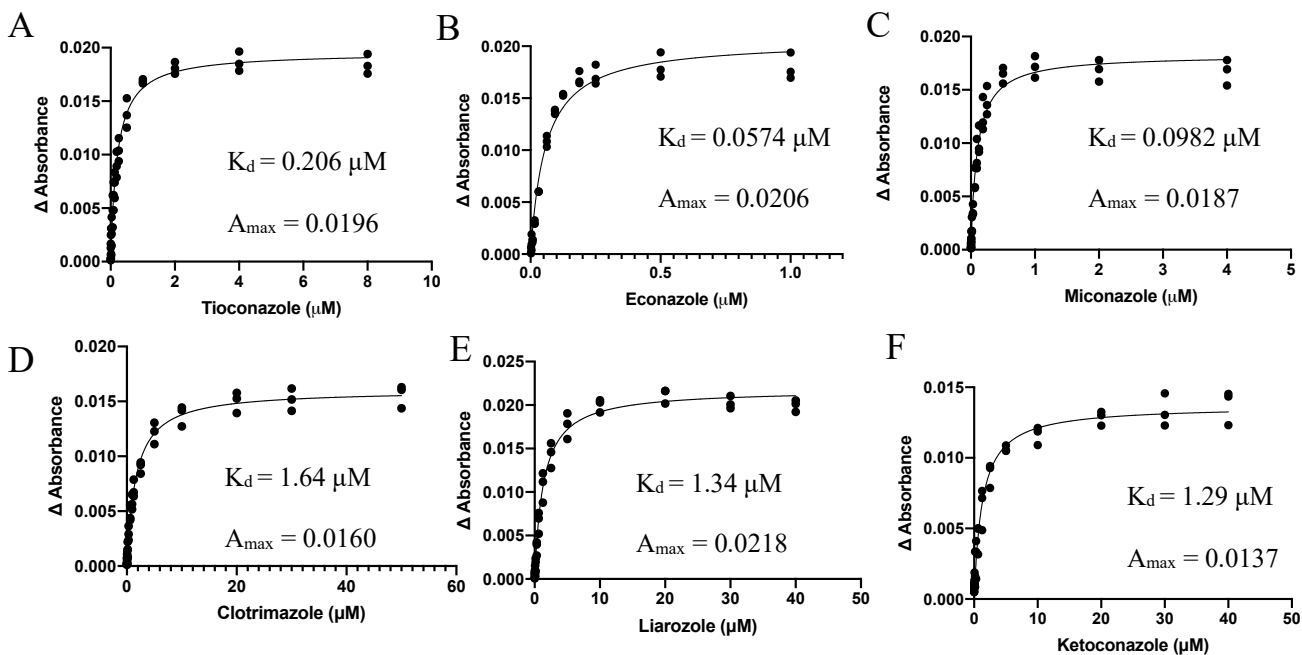
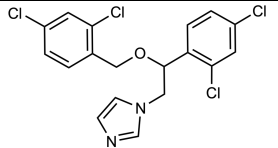
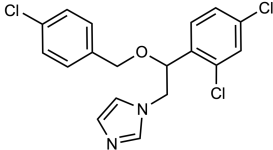
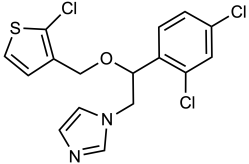
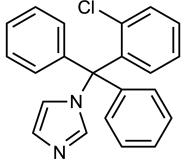
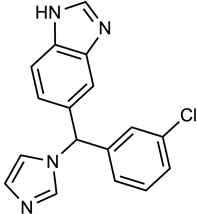
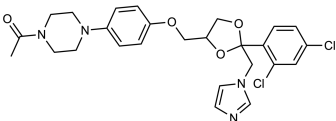
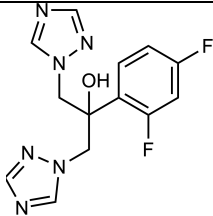


Figure 2.5 CYP8B1 binding of azoles (A) tioconazole, (B) econazole, (C) miconazole, (D) clotrimazole, (E) liarozole, and (F) ketoconazole.

Table 2.1 CYP8B1 binding and inhibition by azoles.

Compound	Structure	Binding		Inhibition	
		Shift in Soret peak	K_d (μM)	turnover at 80 μM (%)	IC_{50} (μM)
Miconazole		Type II	0.098 (0.085-0.11)	0.75	0.460 (0.315-0.629)

Econazole		Type II	0.057 (0.048-0.068)	1.7	0.803 (0.663-0.963)
Tioconazole		Type II	0.21 (0.18-0.24)	1.4	3.94 (3.13-5.06)
Clotrimazole		Type II	1.6 (1.5-1.8)	6.8	7.36 (4.83-14.7)
Liarozole		Type II	1.3 (1.2-1.5)	30	37.7 (25.5-61.8)
Ketoconazole		Type II	1.3 (1.1-1.6)	16	N.D.
Fluconazole		None	N.D	95	N.D.

2.4.6 CYP8B1 Inhibition

To validate that the binding observed for azoles above was inhibitory, CYP8B1 was first evaluated for its ability to generate the native $7\alpha,12\alpha$ -dihydroxycholest-4-en-3-one product in the

presence of a single, high (80 μM) concentration of each azole inhibitor. The remaining activity ranged from less than 1% for miconazole to 30% for liarozole. The only azole that did not significantly inhibit CYP8B1 at this concentration was fluconazole. Most azoles showing significant inhibition at this single high concentration were then evaluated at multiple inhibitor concentrations to determine the half-maximal inhibitory concentration or IC_{50} (Figure 2.6). These IC_{50} values roughly correlated with the K_d values determined above (Table 2.1). Miconazole and econazole are the strongest inhibitors with sub-micromolar IC_{50} values, followed by tioconazole and clotrimazole with IC_{50} values under 10 μM , and liarozole near 40 μM . These results demonstrate that a range of azole inhibitors act on CYP8B1. Identifying structural features of ligands beyond the azole moiety that are compatible with unique features of the rest of CYP8B1 active site should enable the design of more selective inhibitors that might have clinical utility.

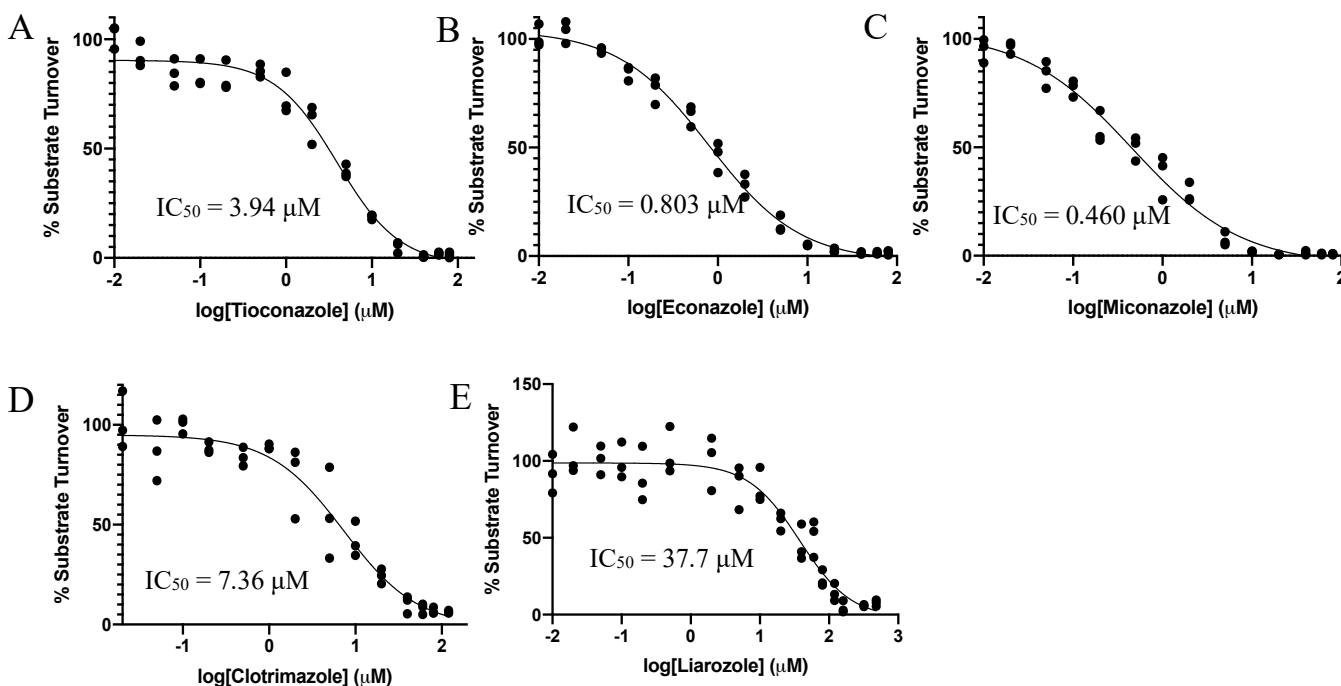


Figure 2.6 CYP8B1 inhibition by azoles (A) tioconazole, (B) econazole, (C) miconazole, (D) clotrimazole, and (E) liarozole.

2.4.7 Structure of CYP8B1 Co-crystallized with the Nonselective Inhibitor (S)-Tioconazole

Table 2.2 X-ray data collection, refinement, and validation statistics.

	CYP8B1/(S)-Tioconazole
Data collection	
Space group	P 2 ₁ 2 ₁ 2 ₁
Cell dimensions	
<i>a</i> , <i>b</i> , <i>c</i> (Å)	58.28, 89.07, 107.85
α , β , γ (°)	90, 90, 90
Resolution (Å)*	41.24-2.60 (2.64-2.60)
Redundancy*	5.9 (5.5)
<i>R</i> _{pim} *	0.053 (0.475)
Mn(I/sd)*	15.8 (1.3)
CC ½*	0.925 (0.585)
Completeness* (%)	98.9 (98.9)
Total Reflections*	104,655
Unique Reflections*	17,925
Refinement	
Resolution (Å)	41.24-2.60 (2.64-2.60)
No. reflections	397,249
<i>R</i> _{work} / <i>R</i> _{free}	0.21/0.27
Molecules per asymmetric unit	1
Number of non-hydrogen atoms / B factor	
Protein	7,429/53.6
Ligand	36/82
Glycerol	14/70
Heme	73/51
Water	17/51
RMS deviations	
Bond lengths (Å)	0.005
Bond angles (°)	0.744
Coordinate error (Maximum-likelihood) (Å)	0.38
Ramachandran plot:	
preferred/allowed/outliers (%)	97.55/2.23/0.22

No structures of human CYP8B1 or close orthologs in other species to guide more selective inhibitor development, but crystallization and structure determination of such membrane P450 enzymes are often facilitated by co-crystallization with high affinity ligands. Thus, structure

determination was pursued with the high affinity azoles identified herein. Screening revealed that CYP8B1 co-crystallized with tioconazole to yielded single, suitably sized oval crystals. X-ray data was collected from a single crystal, solved by molecular replacement employing the structure of human CYP8A1 (PDB: 2IAG) and refined (Table 2.2) to generate a 2.6 Å structure with one molecule in the asymmetric unit.

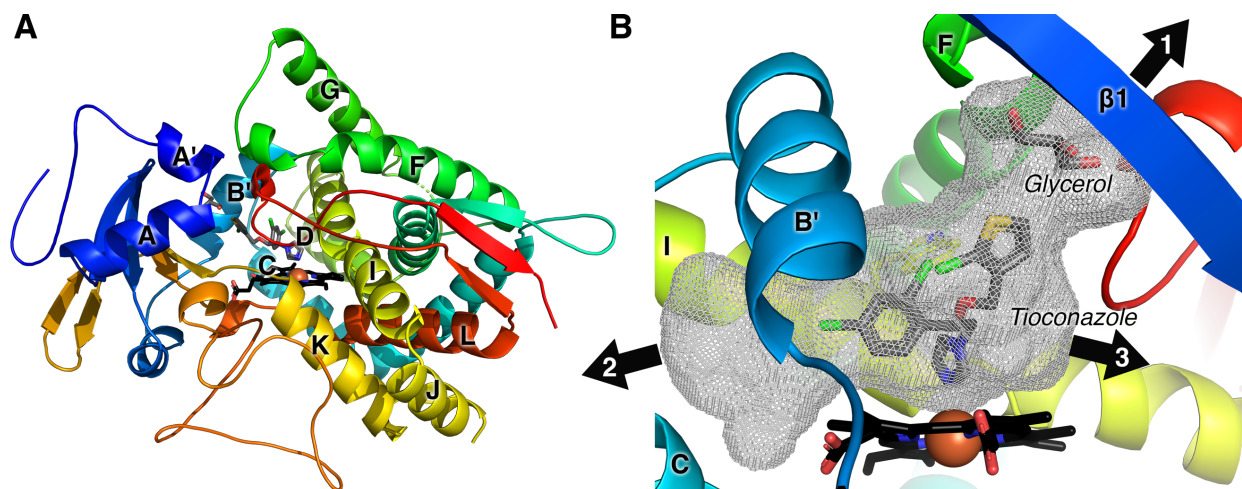


Figure 2.7 CYP8B1 structure. A) Overview of CYP8B1 (ribbons colored red N-terminus to blue C-terminus) in complex with tioconazole and glycerol (grey sticks). The heme is shown in black sticks with a red sphere for the iron. B) Active site cavity (grey mesh). The overall structure reveals a typical cytochrome P450 fold with helices D, E, I, and L surrounding the heme prosthetic group and helices F and G forming the roof of the catalytic domain (Figure 2.7A). The active site adjacent to the heme is large (999 Å³) and relatively flat (due to spatial restriction from W281) but elongated (Figure 2.7B). The active site further opens to the protein exterior and bulk solvent in three directions. A glycerol molecule from the protein buffer occupies part of one channel between the B' and F helices (Figure 2.7B). Two other channels extended through the “roof” of the active site (F' helix and β1), and between B' and C helices.

Consistent with the type II spectral changes observed in the binding studies, (*S*)-tioconazole is clearly bound in the active site with its imidazole nitrogen forming a coordinate covalent bond to

the CYP8B1 heme iron with a distance of 2.56 Å (Figure 2.8A). CYP8B1 was co-crystallized with tioconazole whose stereochemistry was unknown, it was clear from the density that the *S* enantiomer was selectively bound. While the electron density for the azole, phenyl, and thiophene rings are clear, the density is much poorer for the chloro substituents for each of the latter rings, which may suggest flexibility and/or multiple conformations.

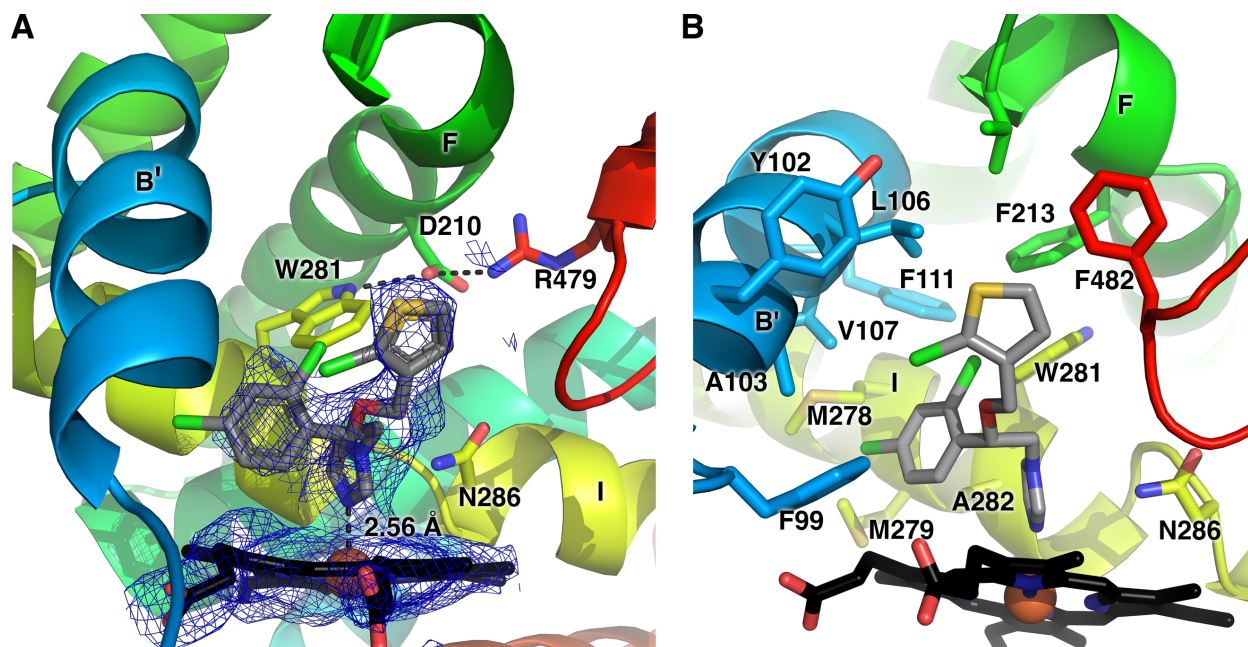


Figure 2.8 CYP8B1 active site illustrating **A) tioconazole ligand simulated annealing composite omit map and B) residues within 5 Å of tioconazole (sticks)**. Coloring as in figure 2.7. Regardless, the active site in the vicinity of the tioconazole ligand is dominated by two primary features (Figure 2.8B). First, it is mainly lined by hydrophobic residues. Residues within 5 Å of tioconazole include F99, Y102, A103, L106, V107, F111, F213, V217, M278, M279, W281, A282, N286, P354, T355, L357, and F482 (Figure 2.8B). These include residues of traditional substrate recognition sites ⁷⁹ (SRS) 1 in or near the B' helix (99, 102, 103, 106, 107, 111), SRS-2 at the end of helix F (213, 217), SRS-4 in the I helix (278, 279, 286), SRS-5 (P354-L357), and SRS-6 or b₄₋₁(F482). This suggests that both hydrophobic and π -stacking and halogen- π interactions would be attractive features in more selective inhibitor. Second, while the

active site is elongated, its depth immediately over the heme is constrained due to the spatial hinderance of W281 and N286 of I helix on one side of the active site (Figure 2.8B). To accommodate (*S*)-tioconazole, the carbon linker between its chiral center and the imidazole bend of almost 90° accommodates the dichlorophenyl and chlorothieryl rings. The indole moiety of W281 interacts with D210, which in turn interacts with R479 near the protein surface. This hydrogen bonding network may be essential for the proper function of CYP8B1, as W281 mutation significantly alters enzyme function (Figure 2.2).

2.4.8 Docking of Native Substrate

While a co-crystal structure with the native substrate has not yet been achieved, the orientation of this 7- α -hydroxycholest-4-en-3-one molecule is of significant interest. Thus, this substrate was docked into the current CYP8B1. After tioconazole was removed, the native substrate was added and docked using induced-fit docking with Glide. One of the top-scoring poses oriented 7- α -hydroxycholest-4-en-3-one in a manner consistent with the known C12-hydroxylation product (Figure 2.9). This pose was the 4th unique pose and had a score of -8.6 kcal/mol. The distance between the heme iron and C12 was 5 Å. The long axis of the steroid nucleus was oriented along with the I helix, but not parallel to it. The steroid α face was directed toward the I helix with the projecting 7 α -hydroxyl projecting right toward W281 in such a way as to suggest this interaction might significantly impact ligand positioning. The steroid b face with its two projecting methyls is generally directed toward the B' helix. Finally, the long C17 hydrocarbon side chain extended out of channel 2 between the B' and I helices (Figure 2.7B). Better scoring poses were in unproductive orientations, roughly orthogonal to the heme plane with the A ring ketone oriented toward the heme and the flexible C17 side chain pointed up into the area occupied by the glycerol.

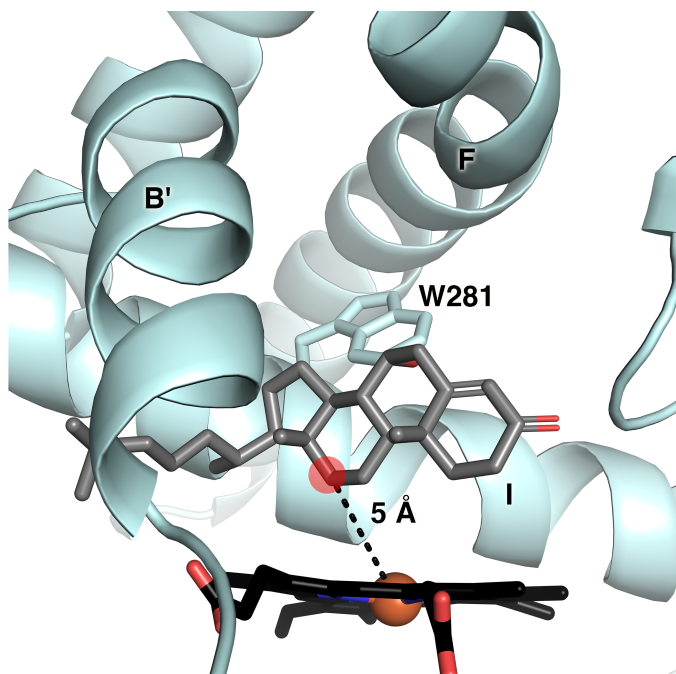


Figure 2.9 The native 7 α -hydroxycholest-4-en-3-one substrate (gray sticks) computationally docked into the CYP8B1 structure (blue ribbons). Heme, black sticks.

2.5 Discussion

2.5.1 Recombinant CYP8B1 Characterization

To our knowledge human CYP8B1 has not previously been recombinantly expressed and purified. However, typical modifications for human membrane P450 engineering, including truncation of the single membrane-spanning N-terminal helix and addition of a C-terminal His tag resulted in good yields of folded protein incorporating the heme prosthetic group that could be highly purified and characterized. Spectral characterization yielded the typical Soret peak for P450 enzymes with water coordinated to the active site heme iron. However, the reduced carbon monoxide difference spectra revealed some interesting observations. Substrate-bound CYP8B1 had the canonical difference peak at 450 nm reflective of normal cysteine thiolate interaction with the heme iron, consistent with catalytically active protein. However in the absence of substrate, the reduced carbon monoxide difference spectrum for CYP8B1 has a peak primarily at 420 nm

with only a small or no peak at 450 nm. Many have suggested that such “P420” protein is catalytically inactive and not reversible to P450^{7, 81}. However over the course of working with many different human P450 enzymes we have observed a number of cases where the “P420” state reverts to a “P450” state in terms of its spectrum and catalytic activity, but none so markedly as CYP8B1. In this case the simple addition of substrate converts almost total “P420” to total “P450”, so it is clearly reversible spectrally. In catalytic assays where substrate would be present, the enzyme is catalytically active with its native substrate. The literature suggests two possible explanations for the “P420” state. One is that the proximal Cys thiolate becomes protonated and dissociates from the heme iron. The other is that this Cys-Fe interaction is substituted for a His-Fe interaction due to some conformational change of the proximal side of the heme⁵. While some P450 enzymes that form the spectral “P420” form have histidines near the proximal cysteine, in CYP8B1 the most reasonably located histidines are all more than 8 Å away from Fe in either 1) the C helix (H124) which can be repositioned in some P450 structures depending on the state⁸²; or 2) His428, found in a flexible loop preceding the proximal cysteine. Regardless of the mechanism, in CYP8B1 substrate binding on the distal site of the heme alters the protein conformation on the proximal side, either via small changes in Cys-Fe interaction or via larger conformational changes to relocate a histidine near the iron.

Further evidence that interactions on the distal side of the heme alter proximal arrangements is found in the W281F mutant. While most mutations are more likely to destabilize proteins, this mutation consistently demonstrated more P450 species and less P420 species in the reduced carbon monoxide difference spectra compared with wild type CYP8B1 (Figure 2.10), but at the same time it impaired substrate binding and significantly reducing catalytic efficiency (Figure 2.2). It is possible that the conformational stability is a tradeoff for catalytic activity.

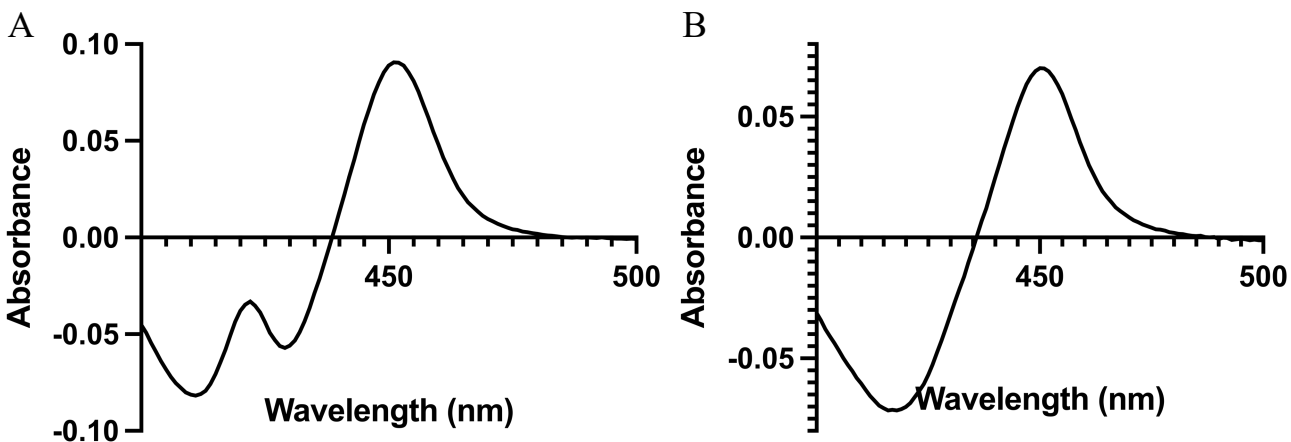


Figure 2.10 W281F CYP8B1 reduced carbon monoxide difference spectrum (A) in the absence of 7 α -hydroxycholest-4-en-3-one and (B) in the presence of 7 α -hydroxycholest-4-en-3-one. Compare to the wild type spectra in Figure 2.1.

2.5.2 CYP8B1 Function

Recombinant, purified CYP8B1 bound both substrate and inhibitors with the typical red-shift and blue-shift of the Soret peak, and consistent with their expected binding modes—water displacement vs. water replacement. The enzyme bound its native substrate with a K_d of 18 nM and catalyzed its 12-hydroxylation with a K_m of 0.5 μ M. Since these two values are only equivalent when the dissociation rate (k_{off}) is large relative to k_{cat} (7.4 min^{-1}), the substrate dissociation rate constant must be quite slow. In many P450 enzyme structures the substrate is observed in an enclosed active site with no channels sufficient for substrate or product passage, thus requiring protein conformational changes with each catalytic cycle. CYP8B1 does have channels between the active site and the exterior bulk solvent when co-crystallized with tioconazole. Thus, either the native substrate is tightly held within the active site despite the existence of these channels, or the protein conformation closes further when substrate is bound to facilitate substrate retention.

The active site residues W281 has previously been suggested to be important in CYP8B1 and several related enzymes. Herein the W281F mutant decreased affinity for its native substrate ~2-

fold but decreased turnover even more drastically, ~6-fold. This data indicates that the major affect is on the catalytic step. The current structure demonstrates that this tryptophan is located directly over the heme iron (Fe-Trp 8.2 Å) and docking suggests it is near the 7aOH substituent of the substrate. altogether this information suggests that W281 is involved in substrate positioning for optimal catalysis. This tryptophan residue is conserved in several other related P450 enzymes, including the CYP8A1 and CYP7A1 active sites and aligns with a tryptophan in CYP7B1, and CYP39A1⁸³. In CYP7A1 and CYP8A1 this tryptophan serves as a “low ceiling” keeper⁸⁴, but also interacts with an asparagine in F-helix, which forms a salt bridge with arginine near the protein surface. In CYP8B1 this triad is conserved among W281, D210, and R479. In CYP7A1 the W283F mutation abolished the spectral response to its native substrate, cholesterol⁸⁰, and impaired catalysis. In CYP7B1 a R486C mutation in this triad correlates with neurodegenerative disease, which is possibly caused by aberrant oxysterol levels⁸⁵. Such information supports the hypothesis that this network is important for proper function in several human cytochrome P450 enzymes.

2.5.3 Towards CYP8B1 Inhibitors

Little attention has been paid to the design and synthesis of selective CYP8B1 inhibitors¹⁷, despite significant evidence that such molecules might be clinically useful in the treatment of non-alcoholic fatty liver disease and type 2 diabetes^{62, 64}. Herein CYP8B1 was demonstrated to bind a relatively broad range of azoles, all with interactions between theazole nitrogen and the heme iron. While such compounds are often poorly selective in discriminating among the 57 human cytochrome P450 enzymes, they often have intrinsically high affinities, modulated the compatibility of the active site with the remainder of the ligand structure. Such is the case here.

The best azoles had affinities under 100 nM and sub-micromolar IC₅₀ values. The three most effective inhibitors, miconazole, econazole, and tioconazole are all very structurally similar,

differing only in substitutions of a thiophene vs. phenyl ring and the specific chlorine substitution pattern. Within this series, the K_d values suggest that the slightly larger phenyl ring and para chlorination of econazole is favorable over the thiophene and ortho chlorination of tioconazole, while additional chlorination at the meta position yields the most effective inhibitor miconazole. While specific halogen interactions are not apparent in the crystal structure with tioconazole, this data suggests that the chlorination substitution pattern should be considered in optimizing binding interactions. If econazole and miconazole bind in similar orientations as that observed for tioconazole, it is possible that their mono- or dichlorophenyl rings interact with F482 via either π - π stacking of halogen- π interactions (Figure 2.8B).

Clotrimazole and liarozole are less effective inhibitors. Their structures are more compact without a methylene bridge between the iron-coordinating imidazole and the rest of the structure. When the methylene is present between the imidazole and the sp^3 carbon from which the other ring systems project, the ligands would be more flexible, which may facilitate conformations whereby the non-imidazole rings are more compatible with the available space in this “low ceiling” binding pocket.

A much larger inhibitor is ketoconazole that still binds with a micromolar K_d value is ketoconazole. While the iron-binding and dichlorophenyl arms of this inhibitor are identical to the tightest-binding compound miconazole, the third arm is significantly elongated. Inspection of this compound and the CYP8B1 active site suggests that the elongated arm might be accommodated by extending out of either of the two channels originating near the two non-imidazole rings of tioconazole.

Finally, despite a core structure somewhat similar to other compounds and two potential iron-coordinating triazoles, fluconazole showed no binding and almost no inhibitory effects to

CYP8B1. This could be due to steric hindrance from the central hydroxyl or due to the fact that triazoles tend to have weaker binding to cytochrome P450 hemes⁵⁴.

Overall, the identification of tight-binding ligands provides an excellent potential starting point for the design of CYP8B1 inhibitors. Additionally, the initial structure-activity relationships discussed herein suggest that affinity can be successfully optimized by modifications of the ligand structure apart from the iron-coordinating group. The next challenge is to identify inhibitor modifications that might provide good selectivity for CYP8B1 over other human cytochrome P450 enzymes.

2.5.4 Analysis of Opportunities for Selectively Targeting CYP8B1

The greatest challenge in clinical CYP8B1 inhibitor design is likely selectivity compared to CYP8A1 and CYP7A1. CYP8A1 (prostaglandin I₂ synthase)⁸⁶ has the highest amino acid sequence identity (41%), but its prostaglandin H₂ substrate is fairly distinct from the CYP8B1 steroidal substrate. CYP7A1 is less identical in terms of amino acid sequence (36%), but acts on the similar steroidal substrate cholesterol. Although CYP7A1 hydroxylates the steroid nucleus at C7 and CYP8B1 hydroxylates C12 there are potential similarities of the active sites. While inhibition of CYP8B1 is desirable for treatment of NAFLD and type 2 diabetes, inhibition of CYP8A1 and CYP7A1 are undesirable as they result in essential hypertension⁸⁷ and hypercholesterolemia⁸⁸, respectively. Thus the first CYP8B1 structure herein will be compared to

structures of both CYP8A1 and CYP7A1, which have been determined previously^{83, 86}.

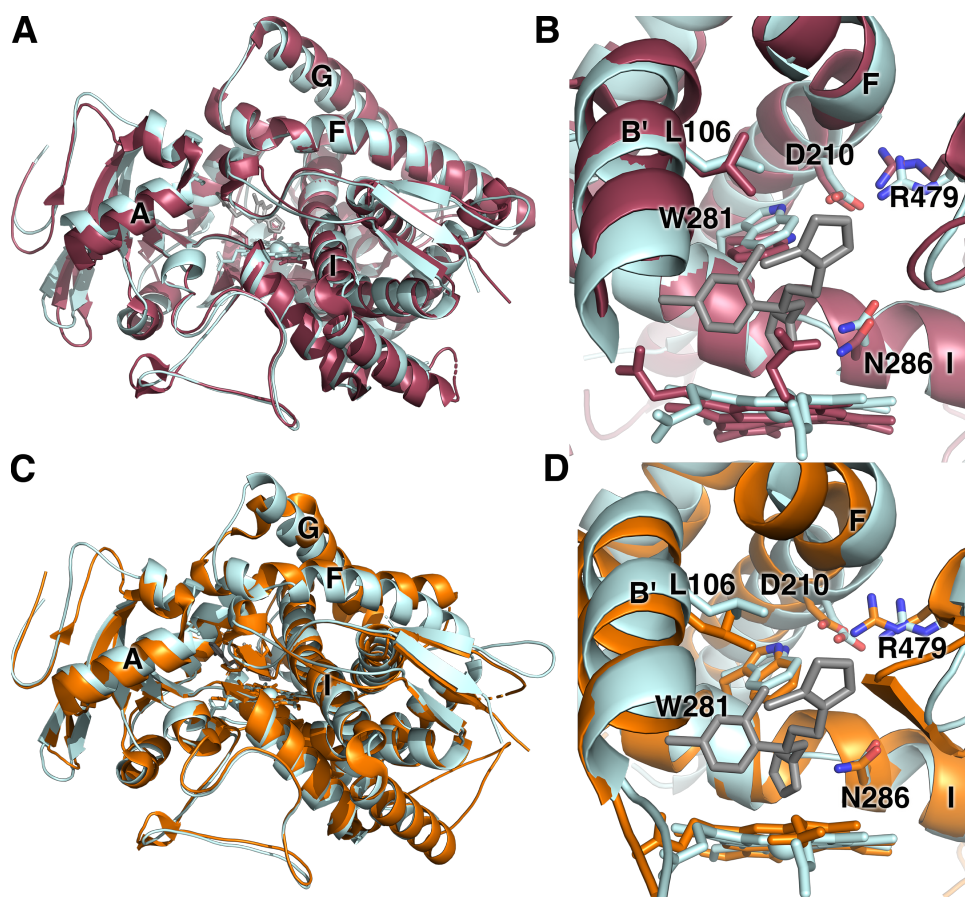


Figure 2.11 Structural comparisons of CYP8B1 (pale cyan) with CYP8A1 (raspberry) and CYP7A1 (orange). Comparisons of CYP8B1 with CYP8A1 A) overall and B) active sites. Comparisons of CYP8B1 with CYP7A1 C) overall and D) active sites.

CYP8A1 converts prostaglandin H₂ to prostacyclin without the typical requirement for cytochrome P450 reductase or NADPH as an electron donor to initiate the reaction⁸⁶. Despite their different substrates and distinctive catalytic reactions, CYP8A1 and CYP8B1 have the most similar overall and active site amino acid sequences of all human cytochrome P450 enzymes. Two human CYP8A1 structures are available, one with the inhibitor minoxidil (PDB 3B6H)⁸⁶ and one which is ligand-free (PDB 1IAG)⁸⁶. These structures have an overall Ca RMSD 0.1 Å with most distinctions occurring on the proximal side of the heme rather than the distal active site cavity⁸⁶. The ligand-free CYP8A1 structure (PDB 2IAG) aligns with the CYP8B1/tioconazole structure

with a Ca RMSD of 1.54 Å (Figure 2.11A). Overlay of the active sites (Figure 2.11B) illustrates the strong conservation of active site residues and orientations, including the tryptophan serving as a “low ceiling” keeper⁸⁴ (W281 in CYP8B1), the asparagine protruding into the active site (N286 in CYP8B1) and the noted interactions between the I helix tryptophan, F helix aspartic acid (D210 in CYP8B1) and surface arginine (R479 in CYP8B1). There are potential notable differences in the topology of the CYP8B1 and CYP8A1 active sites, however. These are primarily related to differences in the heme porphyrin plane and the positioning of the propionates. Largely because of these differences, the volume of the CYP8A1 active site is slightly larger (1237 Å³, Figure 2.12A) with two major differences. First, the CYP8A1 active site extends toward the distal side of the heme below the two propionates (Figure 2.12A, circle 1) Second, additional active site volume is also observed in CYP8A1 between the I and F helices next to W282 (Figure 2.12A, circle 2), which is thought to accommodate the long side chain of prostaglandin H₂, based on a substrate analog structure of zebrafish CYP8A1⁸⁶. Conversely, unique active site cavity volume is observed above the heme plane in CYP8B1 next to channel 3 (Figure 2.7B). Thus inhibitor designs with larger sizes directly over the heme could be exploited to design inhibitors that are more selective for CYP8B1 than for CYP8A1.

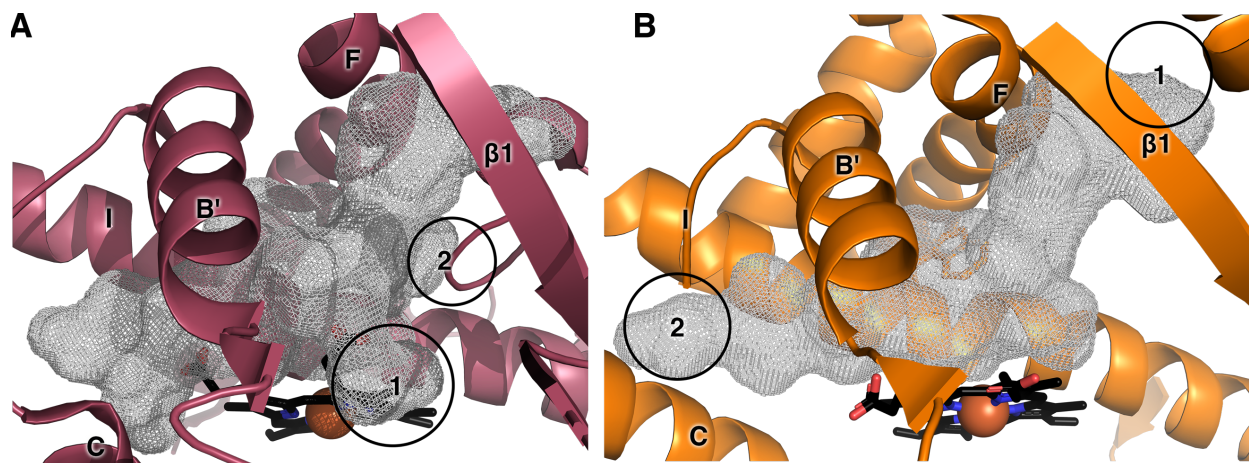


Figure 2.12 Active site cavities (grey mesh) for A) CYP8A1 (raspberry) and B) CYP7A1 (orange). Heme is shown as black sticks with red sphere for iron.

CYP7A1 is the other human P450 enzyme that should probably be a first-line counter target. Although it has lower amino acid sequence identity with CYP8B1 (36%), their steroidal substrates are very similar. CYP7A1 or cholesterol 7 α -hydroxylase catalyzes the first and rate-limiting step in the classic bile acid synthetic pathway⁸³. In addition, CYP7A1 can also hydroxylate cholest-4-en-3-one to form the CYP8B1 substrate 7 α -hydroxy-cholest-4-en-3-one⁸³, suggesting the possibility that high similarities will be observed in their active site architectures. A structure of CYP7A1 with the artificial T104L mutation has been generated in complex with this cholest-4-en-3-one substrate (PDB 3SN5)⁸³. Alignment of the CYP7A1/cholest-4-en-3-one structure with the CYP8B1/tioconazole structure herein similarly yields a low Ca RMSD of 1.35 Å, consistent with relatively close overlay of the overall folds (Figure 2.11C). The most significant differences are observed for the F and G helices and the B' helix. Although active site residue identities are again highly conserved, there are more substantial differences in their placements between CYP7A1 and CYP8B1 (Figure 2.11D) than were observed between CYP8A1 and CYP8B1 (Figure 2.11B), even though the heme plane and propionates are more similar between the former two enzymes. The volume of the CYP7A1 active site is 1035 Å³ (Figure 2.12B), which is more similar with the

CYP8B1 active site volume than CYP8A1. Compared with CYP8B1, the CYP7A1 active site is extends further to the roof of the active site (Figure 2.12B, circle 1) and between helices C and I (Figure 2.12B, circle 2), the latter of which accommodates the long aliphatic chain its hydroxycholest-4-en-3-one substrate. More cavity volume is observed between B' helix and the heme propionate due to the position of B' helix. These differences might be usefully exploited in designing more selective inhibitors.

2.6 Conclusion

CYP8B1 appears to be a promising drug target for the treatment of non-alcoholic fatty liver disease and type 2 diabetes. However, the roles of CYP8B1 in both normal physiology and disease states are still poorly understood and no selective inhibitors have yet been developed as either tool or clinical compounds. Currently, the only study of CYP8B1 depletion was done in mice using *cyp8b1*siRNA, which is a suboptimal therapeutic strategy with substantial delivery difficulties. A selective CYP8B1 inhibitor would be a more desirable probe of the physiology and as a potential drug. The generation, functional characterization, and determination of the first CYP8B1 structure herein should significantly advance this effort. Specific details of the CYP8B1 active site architecture, particularly compared to CYP7A1 and CYP8A1 should facilitate structure-based design of selective CYP8B1 inhibitors. This in turn should promote a better understanding of the role of CYP8B1 inhibition in normal physiology and disease states and potentially provide a possible treatment for nonalcoholic fatty liver disease and type 2 diabetes.

Chapter 3 Pyridine-Containing Substrate Analogs are Restricted from Accessing the Human Cytochrome P450 8B1 Active Site by Tryptophan 281

3.1 Summary

The human oxysterol 12 α -hydroxylase cytochrome P450 8B1 (CYP8B1) is a validated drug target for both type 2 diabetes and non-alcoholic fatty liver disease, but effective selective inhibitors are not yet available. Herein steroidal substrate-mimicking compounds with a pyridine ring appended to the C12 site of metabolism were designed, synthesized, and evaluated in terms of their functional and structural interactions with CYP8B1. While the pyridine nitrogen was intended to coordinate the CYP8B1 active site heme iron, none of these compounds elicited shifts in the CYP8B1 Soret absorbance consistent with this type of interaction. However, when CYP8B1 was co-crystallized with a pyridine-containing inhibitor with the 3-keto- Δ 4 steroid backbone most similar to the endogenous substrate, it was apparent that this ligand was bound in a channel leading to the active site, instead of near the heme iron. Inspection of this structure suggested that tryptophan 281 directly above the heme might restrict binding of potential inhibitors with this design. This hypothesis was supported when a CYP8B1 W281F mutation did allow all three compounds to coordinate the heme iron as designed. These results indicated

*The contents of this chapter have been published: Liu, J., Offei, S., Yoshimoto, F., Scott, E; Pyridine-containing substrate analogs are restricted from accessing the human cytochrome P450 8B1 active site by tryptophan 281. *J Biol Chem.* 2023; 299: 103032.

that the design of next-generation CYP8B1 inhibitors should be compatible with the low-ceiling tryptophan immediately above the heme iron.

3.2 Introduction

In humans cholesterol is converted to two primary bile acids, cholic acid and chenodeoxycholic acid (Figure 3.1). Within this pathway, cytochrome P450 8B1 (CYP8B1) is responsible for determining which bile acid is generated. CYP8B1 is an oxysterol 12 α -hydroxylase enzyme converting 7 α -hydroxycholest-4-en-3-one to 7 α ,12 α -dihydroxycholest-4-en-3-one en route to cholic acid (Figure 3.1) ⁸⁹. In the absence of CYP8B1 12 α -hydroxylation, the primary bile acid produced is chenodeoxycholic acid (Figure 3.1). There are two important distinctions between these two bile acids. First, cholic acid is more hydrophilic than chenodeoxycholic acid and results in higher cholesterol absorption ⁹⁰. As a result the balance of bile acids is recognized as a major regulator of cholesterol uptake and intestinal fat absorption. Second, while both bile acids are regulators of the nuclear farnesoid X receptor (FXR), cholic acid is much weaker than chenodeoxycholic acid. Activation of the FXR receptor increases the clearance of triglycerides and free fatty acids and decreases gluconeogenesis and triglyceride synthesis. As a result of these mechanisms CYP8B1 has been explored as a potential drug target for obesity, type 2 diabetes, and non-alcoholic fatty liver disease. Studies have indicated that mice lacking the gene that encodes for CYP8B1 resist weight gain ⁹¹ and have improved glucose homeostasis through an increase of glucagon like peptide-1 (GLP-1) ³⁰. They also had improved glucose tolerance, insulin sensitivity, and insulin secretion ⁶⁴. Furthermore, *cyp8b1* knockdown led to regression in hepatic steatosis ⁹², an increasingly-common obesity-related state that can progress to steatohepatitis, fibrosis, and cirrhosis, ultimately requiring liver transplant ⁵⁷. Thus, the inhibition of CYP8B1 is a potential therapeutic strategy to treat obesity, type 2 diabetes, and non-alcoholic fatty liver disease.

Several non-specific human CYP8B1 inhibitors have been identified ⁹³. Notably, the azoles miconazole, econazole, and tioconazole all had sub micromolar affinities for CYP8B1 and bound via interaction between an azole nitrogen and the CYP8B1 active site heme iron. However this type of interaction can occur between azoles and many different human P450 enzymes, leading to undesirable off-target effects. Efforts to engineer a more specific CYP8B1 inhibitor were thus undertaken to incorporate heme-coordinating groups into a more substrate-like scaffold. This approach has been successful in developing the prostate cancer drug abiraterone which is an effective FDA-approved inhibitor of the androgen-generating CYP17A1 ⁹⁴. Abiraterone was designed by retaining the CYP17A1 pregnenolone substrate 3 β -hydroxy, D5-steroid backbone and appending a pyridine at the C17 position where CYP17A1 normally hydroxylates. Both binding assays and a co-crystallized structure confirmed that this pyridine nitrogen lone pair coordinates the heme iron in the CYP17A1 active site ¹¹. Therefore, a first round of rationally designed inhibitors for CYP8B1 consisted of steroids similar to its 7 α -hydroxycholest-4-en-3-one substrate modified to incorporate a pyridine substituent at C12 where CYP8B1 hydroxylation occurs. For simplicity this first compound series omitted the C17 hydrocarbon side chain while exploring the effects of different conformations and substituents of the AB ring system and a C17 keto vs. hydroxyl substitution. When one of these compounds was previously given intraperitoneally in the acetate prodrug form to mice on a high fat, high sucrose diet, those animals demonstrated decreased blood glucose levels ¹⁷. This improved insulin resistance was a positive indicator for the reduction of diet-induced obesity.

Herein, we evaluated the ability of this original compound and the two structurally-related potential inhibitors for binding to and inhibition of the intended CYP8B1 target. Instead of the anticipated binding mode with the compounds in the active site with the pyridine coordinating to

the heme iron¹⁷, an X-ray structure of one of the compounds revealed binding much higher above the heme, in an access channel between the protein surface and the active site. Inspection of this structure suggested that access of such compounds further into the active site proper and directly above the heme prosthetic group might have been impeded by steric conflict with the “low ceiling” W281 residue. Indeed, a W281F mutation enabled binding of all three compounds with direct heme coordination. Thus, the current work establishes that CYP8B1 inhibitors seeking to engage the heme iron should be designed to fit under W281.

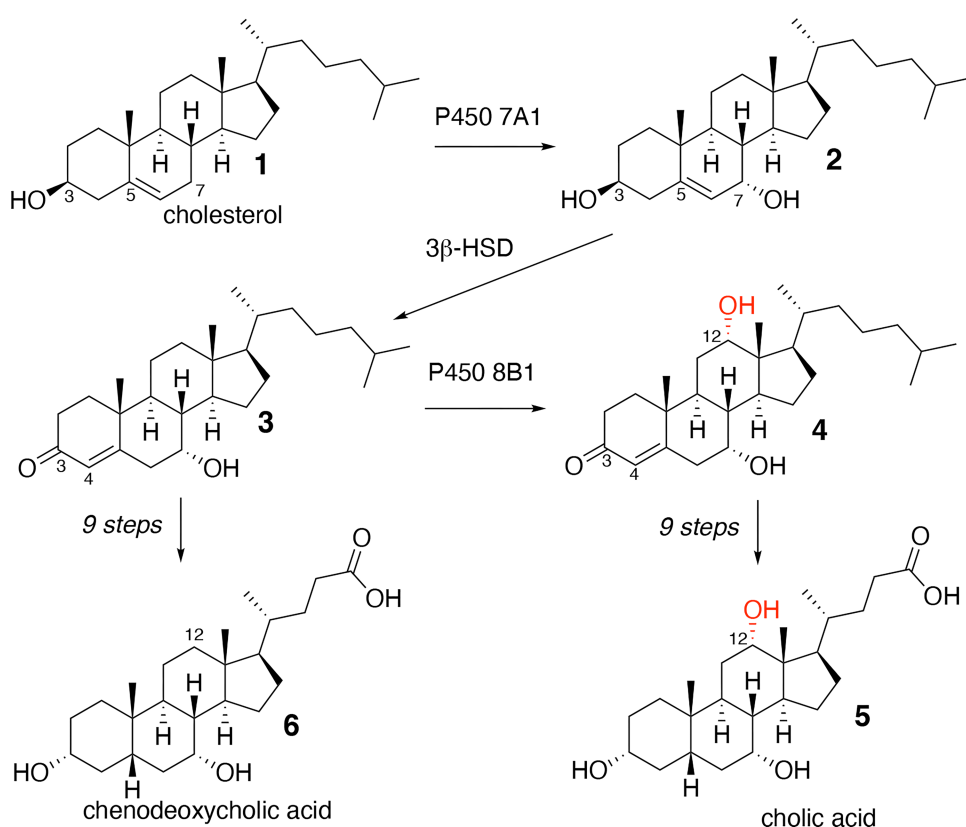


Figure 3.1 Classic pathway for cholesterol conversion to bile acids.

Cholesterol (1) is acted on by the 7 α -hydroxylase CYP7A1 and 3 β -hydroxysteroid dehydrogenase (3 β -HSD) to generate the common bile acid precursor 7 α -hydroxy-cholest-4-en-3-one (3). In the presence of CYP8B1, this common intermediate is 12 α -hydroxylated to yield 7 α ,12 α -dihydroxy-cholest-4-en-3-one (4), which is subsequently modified on the A ring and side chain to generate cholic acid (5). In the absence of CYP8B1 catalysis, the common 7 α -hydroxy-cholest-4-en-3-one intermediate (3) directly undergoes the same modifications of the A ring and side chain to generate acid chenodeoxycholic acid (6). The resulting primary bile acids cholic

acid and chenodeoxycholic acid thus differ only by the 12-OH installed by CYP8B1 but have substantially different lipid absorption and signaling profiles.

3.3 Experimental procedures

3.3.1 Synthesis of 12-(3'-pyridyl)-androsta-4,11-dien-3,17-dione (Compound 8)

Aluminum isopropoxide (6.46 g, 31.7 mmol, 10 eq) and 1-methyl-4-piperidone (7.78 ml, 63.3 mmol, 20 eq) were added to a 500 ml round bottom flask containing the C12-pyridine containing 3 β -hydroxy-D5 steroid **7** (1.15 g, 3.16 mmol, 1 eq) in toluene (250 ml). The reaction was refluxed using a Dean-Stark apparatus where toluene was removed in portions (3 x 20 ml). The volume of the reaction was never reduced below 150 ml. The progress of the reaction was monitored by thin layer chromatography and NMR. After 24 h, a second portion of 1-methyl-4-piperidone (10 ml, 86.6 mmol, 27 eq) was added to the reaction and refluxing continued for another 24 h. The reaction solution was diluted with ethyl acetate (200 ml). The resulting solution was washed with deionized water (3 \times 200 ml). The aluminum isopropoxide suspension that crashed out during the workup was filtered off with a fritted filter funnel under vacuum. The organic layer was concentrated under reduced pressure to form a crude yellow oil. The crude oil was purified by column chromatography (50 % ethyl acetate hexanes \rightarrow 100% ethyl acetate) to yield the 3-keto, D⁴-pyridine product **8** (1 g) with the 1-methyl-4-piperidone as a major contaminant. This mixture was repurified by column chromatography (100% ethyl acetate) to afford the 3-keto, D⁴-pyridine product **8** as a white fluffy solid (180 mg, 0.497 mmol, 16%); R_f: 0.39 (100 % ethyl acetate); $[\alpha]_D^{20} + 239.3^\circ$ [5.6×10^{-4} in CHCl₃]; IR (ATR) 3459.13, 3025.93, 2927.84, 1736.33, 1663.04, 1447.04 cm⁻¹; ¹H NMR (500 MHz, CDCl₃) δ 8.56 (s, 1H), 8.46 (s, 1H), 7.69 (d, $J = 7.35$ Hz, 1H), 7.25 (m, 1H), 5.83 (s, 1H), 5.55 (s, 1H), 2.61 – 2.34 (m, 6H), 2.26 – 1.90 (m, 6H), 1.88 – 1.79 (m, 1H), 1.70 (m, 1H), 1.38 – 1.29 (m, 1H), 1.27 (s, 3H), 1.22 (s, 3H); ¹³C NMR (500 MHz, CDCl₃) δ 214.60, 199.08, 168.41, 149.18, 148.06, 143.06, 136.92, 136.26, 127.88, 125.77, 122.39, 56.42,

51.26, 49.11, 39.18, 36.57, 35.32, 33.74, 33.54, 33.18, 29.47, 20.39, 19.40, 17.96. *The yield of this reaction was low due to the water workup step to remove the 1-methyl-4-piperidone. Because both the pyridine product (**8**) and the 1-methyl-4-piperidone reagent, which was in excess, are soluble in water, some of the desired product is lost in the aqueous layer. Furthermore, during the purification by silica gel column chromatography, the reagent (1-methyl-4-piperidone) co-elutes with the desired product. These mixtures were not isolated to move forward with pure compound in the next step.

3.3.2 Synthesis of 12-(3'-pyridyl)-androsta-4,11-diene 3a,17b-diol (Compound 9)

In a 50 ml round bottom flask containing the 3-keto, D4-steroid (**8**) (39 mg, 0.107 mmol, 1 eq) in methanol and tetrahydrofuran solution (10 ml, 1:1 v/v) was added NaBH₄ (67 mg, 1.77 mmol, 16.5 eq). The reaction was stirred for 20 minutes. The reaction was quenched with the addition of water (20 ml) and extracted with ethyl acetate (3 × 20 ml). The organic layers were combined and concentrated under reduced pressure to afford a crude white solid residue. The crude solid was purified by column chromatography (100 % ethyl acetate → 10% MeOH in CH₂Cl₂) to afford the C3, C17-diol product **9** as a white solid (17.3 mg, 0.047 mmol, 44%); mp 194.6 – 198.5 °C; R_f: 0.33 (100 % ethyl acetate); [α]_D²⁰ - 2050° [2 × 10⁻⁵ in CHCl₃]; IR (ATR) 3282.61, 2918.36, 2849.79, 1588.03, 1435.00, 1259.65 cm⁻¹; ¹H NMR (500 MHz, CDCl₃) δ 8.55 (broad s, 2H), 7.71 (d, *J* = 10.15 Hz, 1H), 7.31 (m, 1H), 5.44 (s, 1H), 5.38 (s, 1H), 4.18 (m, 1H), 4.09 (m, 1H), 2.32 (apparent t, *J* = 11.81 Hz, 2H), 2.21 – 2.14 (m, 3H), 2.03 – 1.84 (m, 2H), 1.82 – 1.74 (m, 3H), 1.66 – 1.58 (m, 3H), 1.52 – 1.33 (m, 4H), 1.08 (s, 3H), 1.07 (s, 3H); ¹³C NMR (500 MHz, CDCl₃) δ 148.86, 147.71, 146.18, 145.83, 136.33, 127.66, 125.55, 123.04, 76.80, 68.02, 57.73, 49.22, 48.21, 38.12, 35.06, 34.24, 32.89, 31.33, 30.94, 29.28, 22.10, 19.87, 15.66.

3.3.3 Expression and purification of WT and W281F mutant CYP8B1

The human CYP8B1 cDNA was synthesized with codon optimization for *E. coli* expression (Genscript, Piscataway, NJ). Nucleotides coding for wild type amino acids 1-25 composing the transmembrane helix were truncated and replaced with nucleotides coding for the sequence MAKKTSS. Nucleotides were also added at the C-terminus to code for a six-residue histidine tag just prior to the stop codon. The resulting sequence was cloned into the pCWori+ vector. For the mutant, an extra mutation W281F was made. Wild type and W281F CYP8B1 were expressed and purified as described ⁹³.

3.3.4 Expression and purification of Human cytochrome P450 reductase

Full-length human cytochrome P450 reductase with K59Q mutation was expressed and purified as described ⁹³.

3.3.5 Ligand binding assay

Ligand binding affinities were determined by monitoring shifts in the CYP8B1 heme absorbance spectrum as described previously ⁵⁴. Compounds **7**, **8**, and **9** (dissolved in DMSO) were titrated into 1 μ M CYP8B1 or W281F CYP8B1 in 50 mM potassium phosphate, 20% glycerol in a 1 cm path length cuvette. Changes in absorbance (local absorbance maximum minus minimum) were plotted against ligand concentration and analyzed using the single-site specific binding equation using GraphPad Prism version 8.0.0 for Mac OS X (GraphPad Software, San Diego, CA USA). All titration experiments were repeated in triplicate.

3.3.6 WT and W281F mutant CYP8B1 inhibition assays

Compounds **7**, **8**, and **9** (dissolved in DMSO) were evaluated for inhibition of ***WT and W281F mutant*** CYP8B1 at a single fixed concentration of 80 μ M as described ⁹³ with the following modifications. The modifications are 1) the concentration of the substrate 7 α -hydroxycholest-4-

en-3-one was held constant at the K_m of 0.5 μM for the WT CYP8B1 and 0.54 μM for the W281F mutant CYP8B1, 2) the reaction volume was decreased to 500 μL . Subsequently, the concentration of compound **9** leading to 50% inhibition (IC_{50}) of 7 α -hydroxycholest-4-en-3-one metabolism by W281F mutant CYP8B1 was determined as described in the CYP8B1 inhibition assays section of reference ⁹³. Quantification of sterol products was conducted as described ⁹³ with chromatography performed on a C18 reverse phase column (Luna 5 μm , C18, 150 x 4.6 mm, Phenomenex, Torrance, CA) using an acetonitrile-water gradient (phase A: 10% acetonitrile, phase B: 100% acetonitrile), except that 30 μL of each sample was injected onto the column. Compound **7**, **8**, and **9** eluted at 8 min, 8.5 min and 7 min, respectively. The remaining activity was determined by comparison to control reactions without inhibitor. These experiments were performed in duplicate or triplicates.

3.3.7 Crystallization and structural determination

Purified CYP8B1 (20 mg/mL) in 50 mM potassium phosphate, pH 7.4, 50 mM NaCl, 20% (v/v) glycerol, 1 mM EDTA was incubated with 400 μM compound **8**. CYP8B1 crystals were grown using sitting drop vapor diffusion equilibration. The CYP8B1/compound **8** complex was equilibrated against 0.1 M sodium malonate pH 8.0, 0.1 M Tris pH 8.0, and 30% w/v polyethylene glycol 1,000 at 25 $^{\circ}\text{C}$. Crystals formed within 24 hr. Crystals were cryoprotected with mother liquor plus 30% glycerol and flash cooled in liquid nitrogen. Diffraction data were collected on beamline BL 12-2 of the Stanford Synchrotron Radiation Lightsource and processed using XDS ⁹⁵. The CYP8B1/compound **8** structure was solved by molecular replacement using Phaser ⁷⁰ with a search model consisting of CYP8B1 crystallized with tioconazole (PDB entry 7LYX) with tioconazole, heme, and water removed. Model building and refinement were performed iteratively with Coot ⁷¹ and Phenix.refine ⁷², respectively. The ligand compound **8** was generated using elbow

⁷³ in Phenix. Active site void volumes were calculated using VOIDOO ⁷⁴, with probe radius = 1.4 Å and grid spacing of 1.0. Figures were generated with PyMOL ⁷⁵.

3.4 Results

3.4.1 Chemical Synthesis of Compounds

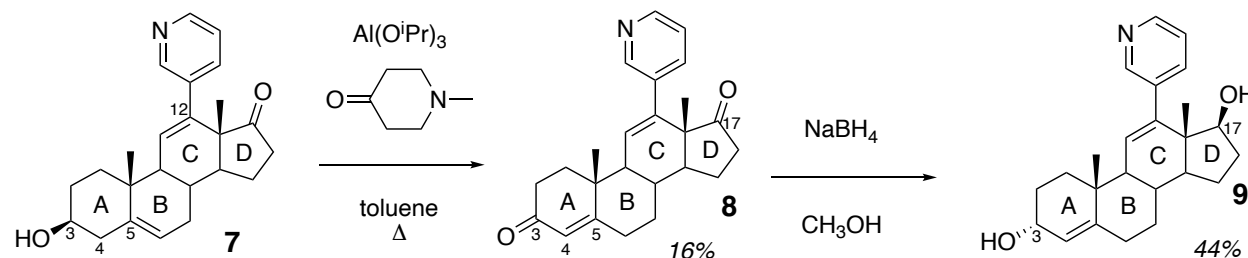


Figure 3.2 Synthesis of three substrate-based 12-pyridine containing steroid analogs as potential inhibitors of CYP8B1. Differences explored include modifications at C3, placement of the double ring Δ4 in the A ring vs. Δ5 in the B ring, and modifications of at C17.

The three CYP8B1-targeted compounds were generally based on this enzyme's 7α-hydroxycholest-4-en-3-one substrate, simplified by replacing the long side chain with either a hydroxyl or ketone. Analogs varied substituents at C3 and positioning of a double bond in either the D4 or D5 position frequently occurring in steroidal compounds, while the C12 pyridine was conserved. The initial compound included 3β-hydroxy, D5, C17-keto, and C12-pyridine components (Figure 3.2, **7**), generated as previously reported ⁹⁶. This compound was treated under Oppenauer conditions to yield the corresponding 3,17-diketone, D4 product (Figure 3.2, **8**). This diketone product was subsequently treated with NaBH₄ to afford the corresponding 3α,17β-dihydroxy D4 sterol (Figure 3.2, **9**).

3.4.2 CYP8B1 Binding of 12-Pyridine Substituted Steroids

Inhibitors that access P450 active sites and have nitrogen heteroatoms that coordinate to the heme cause the heme Soret band absorbance to shift to higher wavelengths because they

replace the heme-coordinated water (~ 418 nm \rightarrow ~ 424 nm). Such shifts in the Soret UV-Vis spectrum are often observed in difference mode and are termed the type II binding mode⁹⁷. In contrast, addition of substrates to P450 enzymes usually bind in the active site close enough to displace this water, causing a spin shift and shifting the λ_{max} to lower wavelengths (e.g. ~ 418 nm \rightarrow ~ 393 nm) and result in type I binding difference spectra⁹⁷.

As expected, the purified, recombinant CYP8B1 used herein demonstrates the expected type I spectral shift when its substrate 7α -hydroxy-cholest-4-en-3-one is added and the expected type II spectral shift when azoles are added, such as the non-selective inhibitor tioconazole⁹³. The compounds designed as CYP8B1 inhibitors herein were expected to bind the heme iron to yield a type II spectral shift, but no significant shifts in the Soret λ_{max} were observed for any of them (Figure 3.3). This was an initial indication that none of the 12-pyridine bearing steroids directly bind to the heme as expected. It further suggested that if the compounds do access the CYP8B1 active site, they are not close enough to the heme to displace the water.

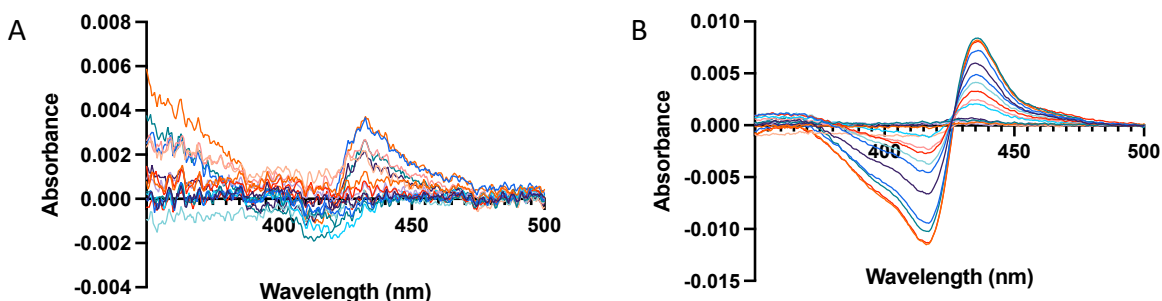


Figure 3.3 UV-visible difference spectra for CYP8B1 wild type ligand binding. Spectra for titrations of CYP8B1 wild type with A) 12-pyridyl compound 8 as an example (0.009 μ M-79.375 μ M) and B) tioconazole (0.000195 μ M-8 μ M) as positive control.

One quite interesting aspect was that after CYP8B1 was first incubated with compound 7 or 8 and then tioconazole was added, the type II spectral shift normally induced by tioconazole addition alone was no longer observed (Figure 3.4). This blockade of tioconazole binding

suggested that these three compounds might still interact with CYP8B1 in another way that didn't result in spectral changes.

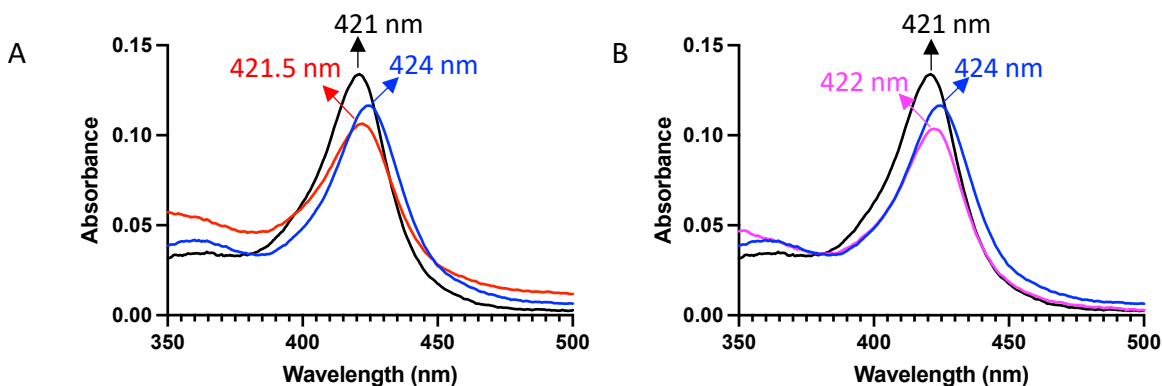


Figure 3.4 UV-visible absolute spectrum for CYP8B1 wild type tioconazole binding in the presence of 12-pyridyl compounds. Spectrum of CYP8B1 wild type with A) no ligand (black, 421 nm), tioconazole in the presence of 280 μ M 12-pyridyl compound 7 (red, 421.5 nm), and tioconazole alone (blue, 424 nm) and B) no ligand (black, 421 nm), tioconazole in the presence of 280 μ M 12-pyridyl compound 8 (magenta, 422 nm), and tioconazole alone (blue, 424 nm)

3.4.3 CYP8B1 Inhibition by 12-Pyridine Substituted Steroids

It is possible to obtain a false negative in the above binding assay for compounds that bind either outside a P450 active site or even those that do access the active site. For example, there are validated P450 substrates that do not cause a shift in the P450 absolute spectrum with the ferric protein. It is likely that such compounds may not move into position near the heme until the P450 goes through later steps in the catalytic cycle, including interaction with its redox partner, reduction to the ferrous form, and/or binding of O_2 ⁹⁸. Thus, the three compounds were next tested at a single high concentration in inhibition assays in which CYP8B1 cycles through each of these states to perform 12 α -hydroxylation of its native 7 α -hydroxycholest-4-en-3-one substrate. While 80 μ M of the non-specific azole inhibitor tioconazole reduced the activity to less than 3.8% of the uninhibited reaction, compounds 7 and 8 had no significant effects on CYP8B1 enzymatic activity and 9 reduced activity by only 34% (Table 3.1).

Table 3.1 Effects of 12-pyridyl steroidal compounds 7, 8, or 9 on the CYP8B1 heme Soret peak and inhibition of its 7 α -hydroxycholest-4-en-3-one 12 α -hydroxylation activity.

Maximal concentrations of compounds 7-9 in the spectral shift assays were 280 μ M. Inhibition was evaluation of in the presence of 80 μ M concentration of compound. Assays were performed in duplicate.

Ligand	Spectral shift	% Activity	Remaining
7 α -hydroxy-4-en-3-one*	420 -> 392 nm	100	
Tioconazole*	420 -> 424 nm	3.77 \pm 2.47	
Compound 7	No	93.7 \pm 2.04	
Compound 8	No	104.6 \pm 6.00	
Compound 9	No	66.1 \pm 1.10	

*7 α -hydroxy-4-en-3-one and tioconazole are substrate and inhibitor controls for type I and type II binding modes, respectively, and have been reported previously⁹³.

Thus, despite compound 7 treatment demonstrating attenuation of obesity-associated glucose intolerance in mice¹⁷, none of the inhibitors significantly inhibited CYP8B1 metabolism of its native substrate. Therefore, the attenuation of obesity-associated glucose intolerance by compound 7 may be via its interaction with enzymes other than CYP8B1.

3.4.4 Structure of CYP8B1 Co-crystallized with Compound 8

To understand whether or how these 12-pyridine steroid compounds bind to CYP8B1, structure determination was pursued with compounds 7 and 8. CYP8B1 co-crystallized with compound 8, yielding single, suitably sized oval crystals. X-ray data was collected from a single crystal, solved by molecular replacement employing the structure of human CYP8B1 in complex with tioconazole (PDB: 7LYX), and refined (Table 3.2) to provide a 2.65 Å structure.

Table 3.2 X-ray data collection, refinement, and validation statistics.

	CYP8B1/Compound 8
Data collection	
Space group	P 2 ₁ 2 ₁ 2 ₁
Cell dimensions	
<i>a</i> , <i>b</i> , <i>c</i> (Å)	62.13, 90.12, 103.02
α , β , γ (°)	90, 90, 90
Resolution (Å)*	39.65-2.65 (2.79-2.65)
Redundancy*	12.5 (9.1)

R_{pim}^*	0.054 (0.602)
Mn(I/sd)*	9.5 (1.3)
CC $\frac{1}{2}$ *	0.998 (0.659)
Completeness* (%)	99.2 (95.4)
Total Reflections	217,070
Unique Reflections	17,297
Refinement	
Resolution (Å)	39.65-2.65 (2.79-2.65)
No. reflections	217,070
$R_{\text{work}} / R_{\text{free}}$	0.22/0.27
Molecules per asymmetric unit	1
Number of non-hydrogen atoms / B factor	
Protein	7,431/63
Ligand	27/20
Heme	49/62
Water	8/60
RMS deviations	
Bond lengths (Å)	0.015
Bond angles (°)	1.1
Coordinate error (Maximum-likelihood) (Å)	0.31
Ramachandran plot:	
preferred/allowed/outliers (%)	96.43/3.57/0

*Highest resolution shell is shown in parenthesis.

This structure retained the characteristic cytochrome P450 fold (Figure 3.5A) and revealed that compound **8** does indeed bind to CYP8B1. Instead of binding in the active site proper near the heme as designed, it is located in an access channel between the protein surface and active site between F, B' and A helices (Figure 3.5B). The absence of an interaction between the pyridine nitrogen and heme iron is consistent with absence of spectral changes in solution. Instead the pyridine nitrogen of compound **8** hydrogen bonds with the side chain hydroxyl of Y102 in the B' helix (2.6 Å, Figure 3.5B). The C3 and C17 keto groups do not form notable interactions with the walls of the CYP8B1 channel. The rest of the interactions are largely hydrophobic. Residues within 5 Å of compound **8** include F49, R50, M53, L72, G73, G74, Q75, F77, F79, L106, V107, L110, F111, F213, V217, Y218, W281, P354, T355, L357, W480, and F482.

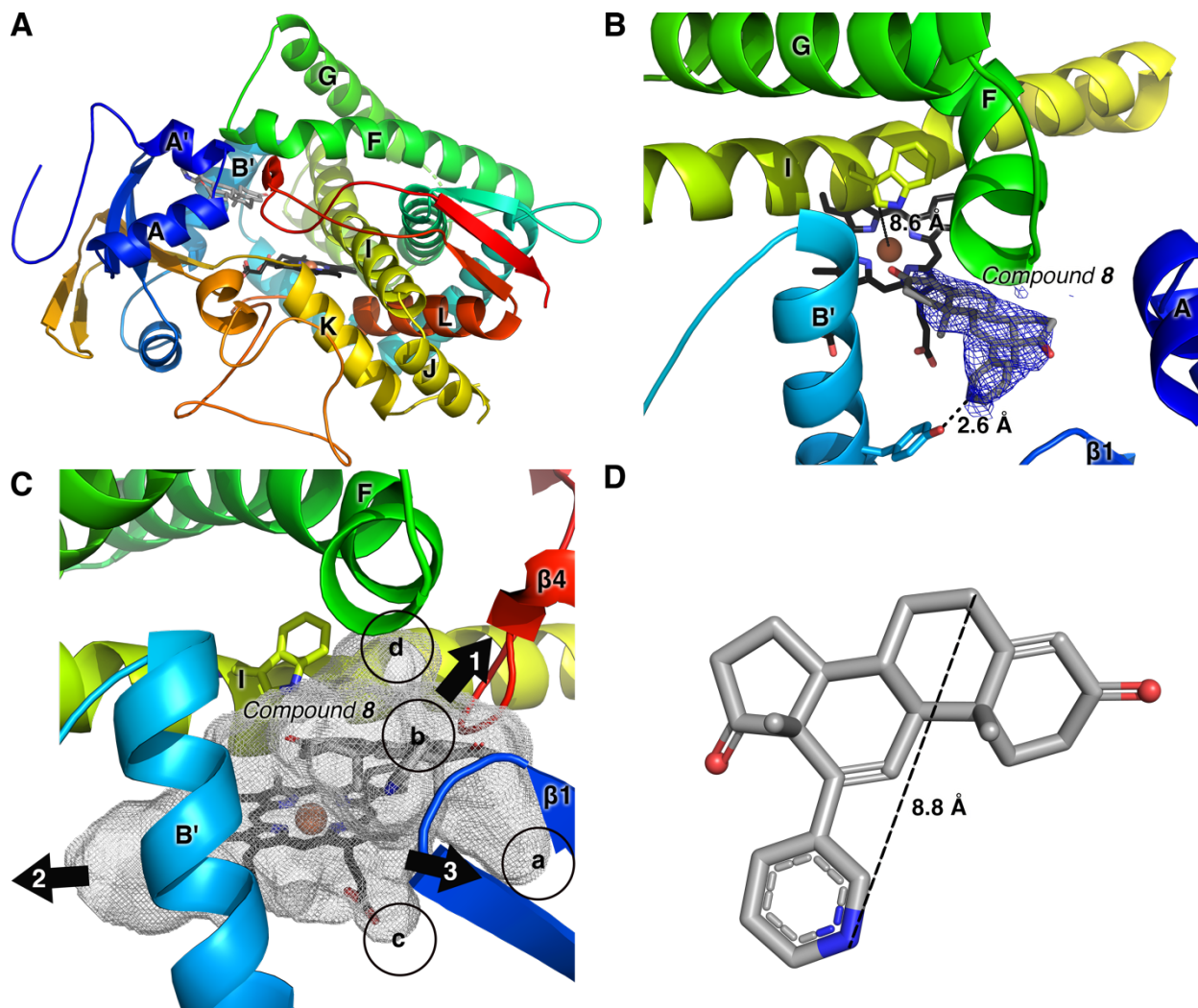


Figure 3.5 Structures of CYP8B1 and 12-pyridyl compound 8. A) Overview of CYP8B1 (ribbons colored red N-terminus to blue C-terminus) in complex with compound **8** (grey sticks). The CYP8B1 heme is shown in black sticks with a red sphere for the iron. B) Simulated annealing composite omit map for compound **8**. C) Active site cavity (grey mesh), with circles a-d indicating areas with additional space compared to the complex with tioconazole, with arrows indicating channels opening to the protein exterior and bulk solvent. D) The distance between the pyridine nitrogen and the C6 on the opposite side of compound **8** is 8.8 Å.

The overall cavity in which **8** resides is contiguous with the active site immediately over the heme and also communicates with the protein exterior in 3 directions. Compound **8** occupies channel 1 between the F helix and $\beta 4$. Two other channels extend between the B' and I helices (channel 2) and between the I helix and $\beta 1$ -4 (channel 3) (Figure 3.5C). Analysis of the crystal structure with **8** was undertaken to discern why this compound did not move further down toward

the heme iron. Visual inspection revealed that the side chain of I helix tryptophan-281 (W281) is positioned 8.6 Å above the heme iron (Figure 3.5B). The distance from the pyridine nitrogen to C6 on the opposite side of this molecule is 8.8 Å (Figure 3.5D). Thus, the W281 side chain indole projection over the iron forms a low active site ceiling and could limit the size of the ligand that can be positioned directly over the heme.

3.4.5 W281F Mutation in P450 8B1 Has Enhanced Interaction with and Inhibition by 12-Pyridine Substituted Steroids

In order to test the hypothesis that W281 of CYP8B1 prevents these three steroidal compounds from binding to the heme iron in the active site, a W281F site directed mutant was expressed and purified. The CYP8B1 W281F protein is functional in that it both binds and metabolizes the normal substrate, although the affinity and turnover are lower than the wild type enzyme. More specifically, *the W281F mutation resulted in a ~2-fold increase in the K_d and a K_m similar to that of the wild type enzyme, but decreased the k_{cat} six-fold*⁹³. While none of the three compounds examined herein bound to the heme iron of the wild type enzyme to yield a spectral change (*vide supra*), all three 12-pyridyl compounds resulted in a type II spectral shift for the W281F mutant, consistent with pyridine direct coordination to the heme iron (Figure 3.6). These observations support that the tryptophan plays a role in ligand binding above the heme active site. The spectral shifts upon CYP8B1 titration with the 12-pyridyl compounds were also used to determine the binding affinities (Figure 3.7A-3.7C). While compounds **7** and **8** demonstrated ~32 μM dissociation constants, compound **9** bound with almost 5-fold higher affinity at 6.75 μM (Figure 3.7E).

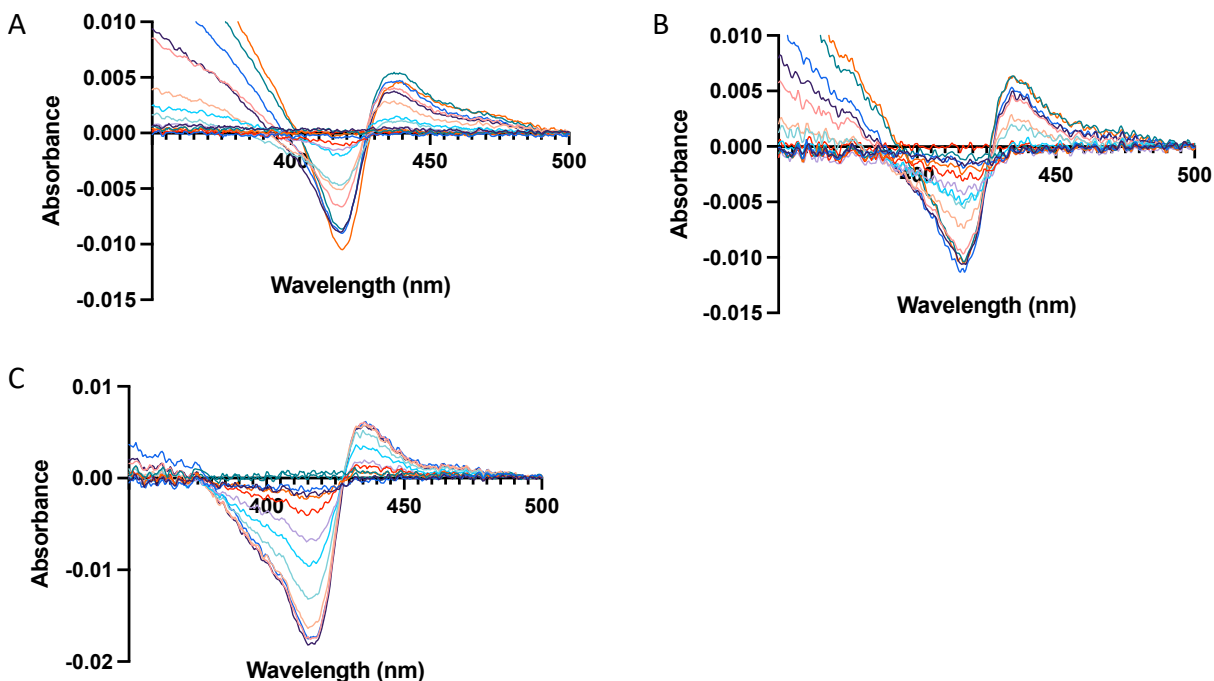
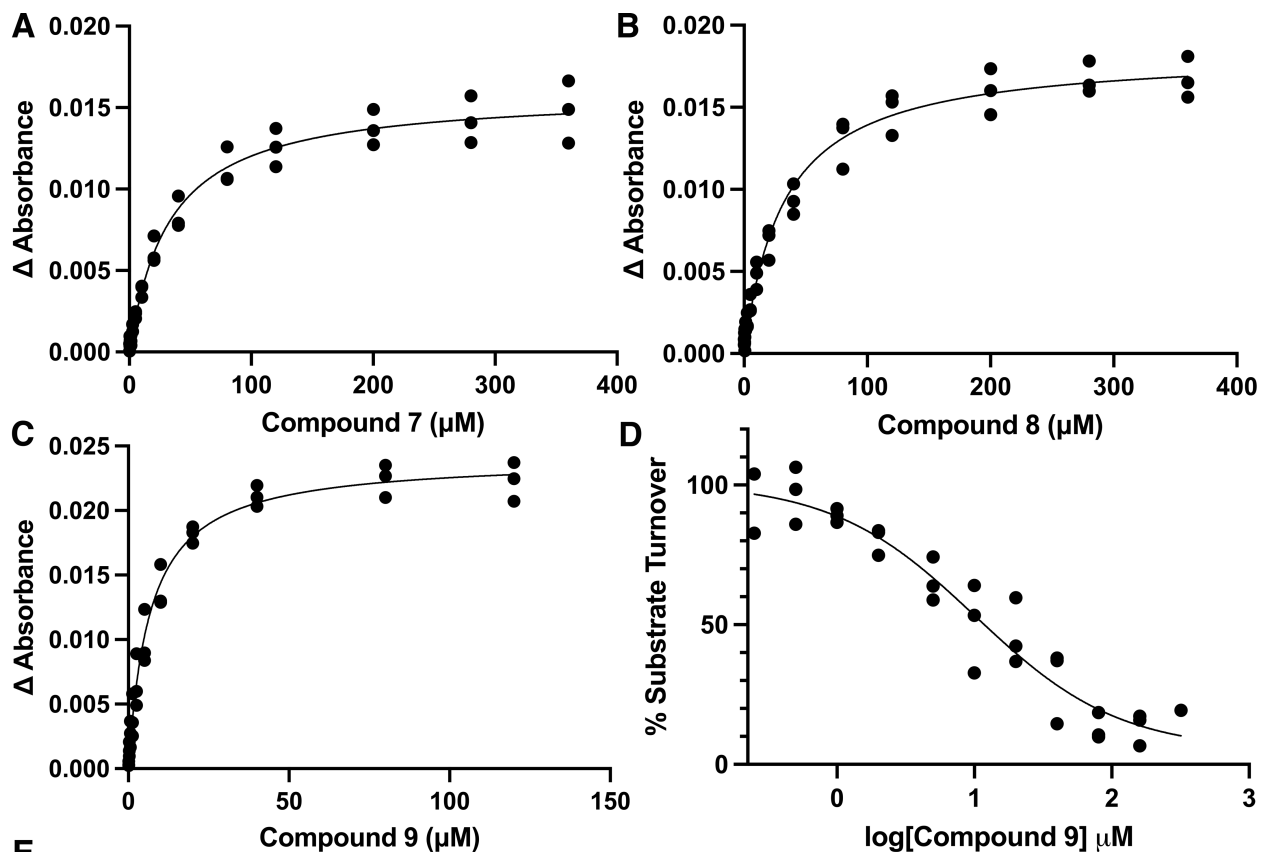


Figure 3.6 UV-visible difference spectra for CYP8B1 W281F mutant binding of compounds A) 7 (0.15625 μ M-360 μ M), B) 8 (0.15625 μ M-360 μ M), and C) 9 (0.15625 μ M-120 μ M).

Further investigation was undertaken to determine if these compounds were also more efficient at inhibition of the W281F mutant than inhibition of wild type CYP8B1. For wild type CYP8B1 80 μ M of compounds 7 and 8 had no significant effects on WT CYP8B1 enzymatic activity and 9 reduced activity by only 34% (Table 3.1). However at this same concentration, 7 and 8 inhibited enzymatic activity of W281F by >40%, while 9 reduced enzymatic activity by 87% (Figure 3.7E). These compounds were then evaluated at multiple inhibitor concentrations to determine the half-maximal inhibitory concentration (IC₅₀). The IC₅₀ of compound with the highest inhibition was 10.2 μ M for 9 (Figures 3.7D and 3.7E). This was consistent with this compound also having the highest affinity. Consistent with their lower affinities, compounds 7 and 8 were much weaker inhibitors, such that their solubility limits precluded reaching high

enough concentrations to determine their IC₅₀ values.



Ligand	K_d (95% CI) (μM)	Remaining activity at 80 μM (%)	IC ₅₀ (95% CI) (μM)
Compound 7	32.5 (26.9-39.4)	52.0 \pm 3.29	N.D.
Compound 8	32.1 (26.3-39.1)	58.3 \pm 1.80	N.D.
Compound 9	6.75 (5.63-8.09)	13.0 \pm 2.78	10.2 (4.68-28.7)

N.D., not determined.

Figure 3.7 W281F mutant CYP8B1 binding and inhibition by the three different 12-pyridyl steroids. Absorbance changes for titration of CYP8B1 mutant W281F with A) Compound 7, B) Compound 8, C) Compound 9. D) inhibition of its 7α -hydroxycholest-4-en-3-one 12α -hydroxylation activity by compound 9. E) Summary of the fitted binding affinities (K_d), inhibition at 80 μM concentration of each compound, and the fitted IC₅₀ of compound 9. Assays were performed in triplicate and all data points

3.5 Discussion

Functionally, compound **8** did not inhibit the wild type enzyme, despite binding in what appears to be a major access channel from the protein surface to the active site. The most likely explanation is that both substrate and **8** bind reversibly in different locations with different

affinities. Substrate binds quite tightly in the active site (K_d 18 nM, ⁹³), while the affinity of **8** binding in the access channel is unknown. Since 80 μ M of **8** does not impede metabolism of substrate (0.5 μ M) the affinity for **8** binding in the channel may be lower than for substrate binding in the active site, *i.e.* substrate is able to outcompete **8**. Thus, the binding assays where **8** in the channel partially prevented substantial binding of tioconazole in the active site (Figure 3.4) were particularly interesting. Tioconazole binding (K_d ~200 nM) is weaker than substrate binding (K_d ~18 nM) ⁹³ and **8** seems to outcompete tioconazole better than substrate. However other explanations are also possible. For example, substrate could enter the active site from another route, bypassing **8**, while tioconazole might use the channel where **8** binds.

Some human cytochrome P450 enzymes are quite malleable in terms of the active site flexibility, allowing the promiscuity to accommodate many different small molecule substrate scaffolds; such is the case for CYP3A4 involved in drug metabolism ¹. Other human cytochrome P450 enzymes are much less promiscuous in terms of the allowable substrates and seem to have less conformational flexibility; this is the case for steroidogenic CYP17A1 despite available structures with a variety of steroidal and non-steroidal ligands ^{10, 11}. As this is only the second structure available for CYP8B1 and the compounds in the two structures have very different scaffolds and bind in different locations, this structure provides a first opportunity to evaluate the conformational flexibility of CYP8B1. A structural comparison of CYP8B1 co-crystallized with tioconazole located in the active site proper (PDB 7LYX, ⁹³) and this new structure with compound **8** binding in an access channel leading to the active site indicates a highly conserved CYP8B1 structure with a root mean square deviation for Ca of 0.72 Å (Figure 3.8A).

While large conformational differences were not observed in the structure overall, smaller shifts were observed for individual helices and for some significant side chains. The B' helix

shifted outward from the active site, which provides more space in the channel to accommodate compound **8** (Figure 3.8B). In addition, first shell active site side chains F209, D210, F213, F216, F236, F277, W281 and F482 projecting from the F, G, and I helices and β 4 region adopted different rotamers in the two structures, which also contributes to some remodeling of the active site (Figure 3.8C). Six of these residues are phenylalanines, which are common in hydrophobic cytochrome P450 active sites and often adopt different rotamers to accommodate different ligand structures. However perhaps most notably, the W281 side chain indole was flipped by 180° in the CYP8B1/compound **8** structure compared to the structure with tioconazole (Figure 3.8D). In the tioconazole structure the W281 indole moiety interacts with D210 in the F helix, which itself interacts with R479 in the β 4 region. The interaction among this triad appears to be critical in stabilizing the interaction of these three disparate secondary structure elements and the W281 mutation significantly reduces enzyme turnover⁹³. However, when **8** binds in this region, the W281 indole flip disrupts this triad and also likely results in expansion of the active site.

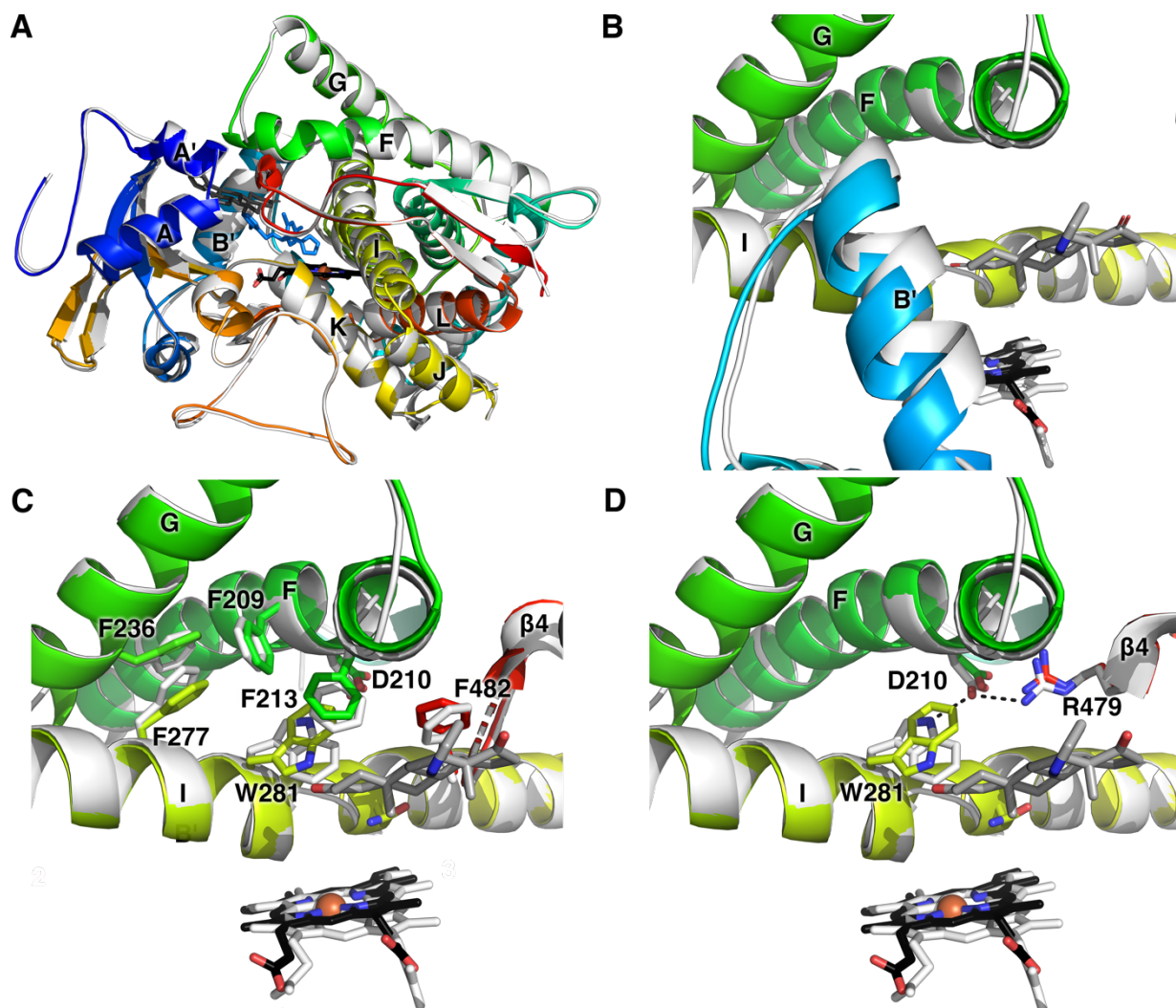


Figure 3.8 Comparisons of CYP8B1 structures binding 12-pyridyl compound **8 and tioconazole.** The CYP8B1/**8** structure is shown as rainbow-colored ribbons progressing from red N-terminus to blue C-terminus and **8** as grey sticks. The CYP8B1/tioconazole structure is shown in grey ribbons with tioconazole as blue sticks. Heme is in black sticks with red sphere. A) The overview demonstrates the differential placement of tioconazole (blue sticks) binding the heme iron and **8** (grey sticks) 11.2 Å from the iron. B) The backbone of the B' helix (blue) is shifted away from the heme, providing additional space for binding of **8**. C) These two structures reveal differential sides chain rotamers for several residues in the F, G, and I helices and β4 region surrounding the active site. These include F209, D210, F213, F216, F236, F277, W281 and F482. D) A network between W281, D210, and R479 (dashed lines) that is present when tioconazole is bound is disrupted when **8** binds and the W281 side chain indole flips by 180°.

Overall the outward shift of the B' helix and changes in the active site rotamers combine to yield an active site for the CYP8B1/compound **8** structure that is ~1639 Å³ (Figure 3.5C), which is more than 1.5 times larger than the active site volume of the CYP8B1/tioconazole structure (999

Å³). The extra cavity volume mainly came from the space between β1 and β4 regions (Figure 3.5C, circles a and b), space between B' helix and heme (Figure 3.5C, circle c), and space between F and I helices (Figure 3.5C, circle d). While this analysis suggests that CYP8B1 has a moderately flexible central ligand-binding cavity, this structural comparison may not be the full extent of the flexibility. A previous study showed that ketoconazole with molecular weight of 531.431 g/mol was also able to bind and inhibit CYP8B1⁹³. This information is likely to be useful for further CYP8B1 inhibitor design and optimization.

A significant finding was that while there are aspects of the central cavity that are flexible, W281 may impose a significant restraint on ligand binding in the region immediately over the heme. In the previous CYP8B1/(*S*)-tioconazole structure, this ligand could fit under W281 because the carbon linker between the chiral center and the imidazole bends almost 90° to accommodate the dichlorophenyl and chlorothienyl rings⁹³. However, compound **8** has a rigid planar structure. The pyridine ring is expected to bind 90° orthogonal to the heme plane and the distance between its pyridine nitrogen and C6 is 8.8 Å even with the flipped indole side chain in the current structure (Figure 3.5D). Thus these C12-pyridine steroids are likely too large to access the active site of CYP8B1, a hypothesis that was supported by their increased ability to bind to the heme iron and inhibit the W281F mutant. In contrast, the distance between C12 and C5 of the CYP8B1 substrate, 7α-hydroxycholest-4-en-3-one, is 5.3 Å⁹⁹ and docking of this substrate into the tioconazole structure suggests that it can bind in the available space in an orientation consistent with the observed 12α-hydroxylation⁹³. Crystal structures of CYP8A1 and CYP7A1 reveal that this conserved tryptophan residue is also 7-9 Å away from the iron in the heme active site, consistent with the concept that this key tryptophan plays an important role in substrate recognition in all three active sites.

3.6 Conclusion

In conclusion, three 12-pyridyl steroid compounds were synthesized and their interaction was tested against human CYP8B1. One of the compounds, bearing a 3-keto, D⁴ steroid backbone (compound **8**), was successfully crystallized with the enzyme. The compound did not coordinate to the active site heme iron as designed, but rather farther away from the heme in a channel. The structure of the CYP8B1 complex with this ligand allowed for a deeper understanding of how CYP8B1 binds ligands. While flexibility was noted for the B' helix and a number of active site side chains, I helix tryptophan 281 was identified as a residue that appeared to limit the vertical dimension of the active site. This concept was supported in that mutation of W281 to phenylalanine did permit all three 12-pyridyl compounds to directly coordinate the heme iron in the active site proper. Therefore, the 12-pyridyl steroid ligands are likely too long (8.8 Å) to be accommodated to bind in the wild type CYP8B1 active site. The outcomes of this study deepen our understanding of the structure-function properties of human CYP8B1 and should facilitate more specific inhibitor designs with the potential to treat metabolism-related diseases including obesity, type 2 diabetes, and NAFLD.

Chapter 4 Cytochrome P450 3A7 Structure Reveals Four Binding Sites for Its Native Substrate Dihydroepiandrosterone Sulfate

4.1 Summary

Human fetal cytochrome P450 3A7 (CYP3A7) is involved in both xenobiotic metabolism and the estriol biosynthetic pathway. Although much is understood about cytochrome P450 3A4 (CYP3A4) and its role in adult drug metabolism, CYP3A7 is poorly characterized in terms of its interactions with both categories of substrates. Herein, a crystallizable mutated form of CYP3A7 was saturated with its primary endogenous substrate dehydroepiandrosterone 3-sulfate (DHEA-S) to yield a 2.6 Å X-ray structure revealing the unexpected capacity to simultaneously bind four copies of DHEA-S. Two DHEA-S molecules are located in the active site proper, one in a ligand access channel, and one on the hydrophobic F'-G' surface normally embedded in the membrane. While neither DHEA-S binding nor metabolism exhibit cooperative kinetics, the current structure is consistent with cooperativity common to CYP3A enzymes. Overall, this information suggests that mechanism(s) of CYP3A7 interactions with steroidal substrates are complex.

4.2 Introduction

Cytochrome P450 3A7 (CYP3A7) is a hepatic enzyme expressed during the fetal and neonatal stages of life. Its activity is highest near birth and declines after the first week but continues throughout the first year of life^{38, 39}. During this time, CYP3A7 can play a dual role in the

*The contents of this chapter have been published: Liu, J., Kandel, S., Lampe, J., Scott, E; Cytochrome P450 3A7 structure reveals four binding sites for its native substrate dehydroepiandrosterone sulfate. *J Biol Chem. Accepted.*

generation of key endogenous biomolecules and the metabolism of xenobiotics including drugs and environmental toxins.

During fetal development, CYP3A7 is a key step in the steroidogenic pathway leading to the production of estriol, often called the pregnancy estrogen. This pathway^{42, 100} initiates with conversion of maternal and fetal cholesterol to pregnenolone by the placenta and the fetal adrenal gland, to some extent. Pregnenolone is then metabolized in the fetal adrenal gland to 17 α -hydroxy-pregnenolone and then on to dehydroepiandrosterone (DHEA) before being sulfated to form dehydroepiandrosterone 3-sulfate (DHEA-S) by SULT2A1. CYP3A7 in the fetal liver subsequently hydroxylates DHEA-S to yield 16 α -hydroxy-DHEA-S. The 16 α -hydroxy product is transferred back to the placenta where the sulfate moiety is removed by sulfatase, and the action of hydroxysteroid dehydrogenases and aromatization by CYP19A1 yield estriol⁴². Estriol levels change throughout pregnancy and are thought to play an important role in regulating uteroplacental blood flow and vascularization when reaching the maternal circulation. As pregnancy progresses beyond eight weeks, maternal serum estriol concentrations rise, with final surge of estriol preceding childbirth¹⁰¹. While the specific roles of fetal-derived estriol are unclear, its importance is such that levels of unconjugated estriol have long been used as a key marker of healthy fetoplacental function⁴³. The key role of CYP3A7 is underscored by the fact that its 16 α -hydroxy-DHEA-S product contributes to >90% of placental steroid synthesis¹⁰². Low levels of estriol have been associated with fetal anencephaly¹⁰³ and Down's syndrome¹⁰⁴. There is also some evidence that CYP3A7 may act to protectively decrease levels of DHEA-S¹⁰⁵ or another important endogenous hormone-like substrate, all-trans retinoic acid¹⁰⁶. While CYP3A7 is not normally expressed in adults, individuals carrying the CYP3A7*1C allele containing the proximal PXR/CAR element of CYP3A4 express the isoform throughout their entire life¹⁰⁷. In such adults

there is some evidence that CYP3A7 action may correlate with a variety of diseases linked to steroidal pathways, including breast and endometrial cancers ¹⁰⁸, systemic autoimmune diseases ¹⁰⁹, congenital adrenal hyperplasia ¹¹⁰, ovarian endometriosis ¹¹¹, and polycystic ovary syndrome ¹¹².

The role of CYP3A7 in xenobiotic metabolism is less well understood but is speculated to be the major contributor to drug elimination for the fetus prior to birth, for premature infants, and during the neonatal stage for normal term births. CYP3A7 catalysis has been detected as early as 50 days post-gestation ¹¹³ and increases throughout pregnancy reaching its maximum around birth, then starts to decrease after the first week following birth ¹¹⁴, but is significant until 6-12 months ^{38,39} and has been detected up to 24 months ^{38,115}. In contrast, the primary adult drug-metabolizing cytochrome P450 3A4 (CYP3A4) enzyme displays little activity in the fetus, but slowly increases after birth to ~30% of adult protein levels at one month. While most drugs are typically developed for adult with clearance dominated by CYP3A4 in mind, some are eventually used off-label in infants where CYP3A4 is absent or minimal and CYP3A7 dominates. Although much is understood about CYP3A4 and its roles in adult drug and xenobiotic metabolism, CYP3A7 still requires further characterization in regard to its ability to bind and metabolize endogenous and xenobiotic substrates. While a number of drug substrates have now been identified for CYP3A7 ¹¹⁶, studies suggest that despite high sequence identity (~87%) between CYP3A7 and CYP3A4, these enzymes interact with drugs quite differently, particularly in regard to their respective K_{cat} values ^{49,53}. Such differential interactions of drugs with the CYP3A7 enzyme can lead to harmful side effects and/or ineffective therapy in neonates and infants. Two particular drug classes of concern are antivirals used to prevent mother to child HIV transmission ^{52,53} and antifungals ⁵⁴ used in underdeveloped pre-term infants who are particularly susceptible to fungal infections.

There is also some evidence that CYP3A7 has the capacity to activate some xenobiotic procarcinogens such as aflatoxin B1 ¹¹⁷.

Despite the need to understand how CYP3A7 interacts with both its pregnancy-related steroids and drugs/xenobiotics, only one structure has been determined for this enzyme. Almost all structures of human cytochrome P450 enzymes are constructs with truncation of the N-terminal transmembrane helix and addition of a C-terminal His tag, but while such a “wild type” version of CYP3A7 expresses quite well and is enzymatically functional ⁵⁴, it has proven very resistant to crystallization. After years of effort by multiple groups, a single structure of CYP3A7 also containing six internal mutations has been solved bound to the adventitious ligand dithiothreitol, introduced during protein purification ¹¹⁸. Herein, an X-ray structure was solved for this same hexa-mutant of CYP3A7, but with its native substrate DHEA-S. This structure reveals that CYP3A7 unexpectedly has four binding sites for its native substrate—two in the active site proper and two in a channel leading out to the surface. Analysis of the details of substrate binding advances our understanding how this understudied enzyme contributes to fetal development through the metabolism of DHEA-S. Knowing the chemical topology of the active site in the presence of its main substrate may also help predict its interactions with drugs, toward increasing safe and effective dosing in the fetal and neonatal stages of life.

4.3 Experimental procedures

4.3.1 Materials

The DHEA-S standard and ampicillin were purchased from Cayman Chemical (Ann Harbor, MI). The metabolite standard 16 α -hydroxy-DHEA-S was obtained from Steraloids (Newport, RI). The isopropyl- β -D-1-thiogalactopyranoside (IPTG), glucose-6-phosphate and β -

nicotinamide adenine dinucleotide phosphate (NADP⁺) were acquired from Alfa Aesar (Haverhill, MA). The glucose-6-phosphate dehydrogenase and the internal standard, estriol 3-sulfate, were purchased from Millipore Sigma (Burlington, MA). The 1,2-dilauroyl-*sn*-glycerol-3-phosphocholine, 1,2-dioleoyl-*sn*-glycero-3-phosphocholine, 1,2-dilauroyl-*sn*-glycero-3-phosphoserine were obtained from Avanti Polar Lipids (Alabaster, AL). All other chemicals and solvents used were obtained from standard suppliers and were of reagent or analytical grade.

4.3.2 Expression and Purification of Wild Type and Hexa-mutant CYP3A7

The human CYP3A7 cDNA was synthesized with codon optimization for *E. coli* expression (Genscript, Piscataway, NJ). Nucleotides coding for wild type amino acids 1-25 composing the transmembrane helix were truncated and replaced with nucleotides coding for the sequence MAKKTSS. Nucleotides were also added at the C-terminus to code for a six-residue histidine tag just prior to the stop codon. For the hexa-mutant K421A/K422A/K424A/R69G/C77G/K244E mutations were additionally incorporated. Both wild type and hexa-mutant genes were cloned into the pCWori+ vector for protein expression. Wild type CYP3A7 was expressed and purified as described⁵⁴. The hexa-mutant was expressed and purified as described¹¹⁸ with the following modifications to be more like the wild type protocol. The modifications are: 1) DH5 α /pGro7 cells were used for expression instead of C41 cells; 2) 4 mg/mL arabinose was added to induce GroEL/ES expression; 3) cells were grown at 25 °C, 190 rpm for 48 h after induction; 4) 80 mM histidine was used in the Ni-NTA elution buffer instead of 30 mM; 5) the Ni-NTA column was washed with 4 column volumes (CV) Ni-NTA lysis buffer containing 0.2% Nonidet P-40 and then 5 CV with the latter buffer supplemented with 5 mM histidine; 6) the CM column wash buffer contains 5 mM potassium phosphate, pH 7.2, instead of 50 mM potassium phosphate, pH 7.4; 7) the eluted protein from CM column was injected onto a

size exclusion column (GE Healthcare HiLoad® 16/60 Superdex® 200 pg) equilibrated and run with CM elution buffer.

4.3.3 Expression and Purification of Human Cytochrome P450 Reductase and Cytochrome *b*₅

Full-length human cytochrome P450 reductase (CPR) with the K59Q mutation to reduce proteolysis was expressed and purified as described⁹³. The full-length human cytochrome *b*₅ cDNA was synthesized (Genscript, Piscataway, N) with codon optimization for *E. coli* expression and with the addition of a N-terminal histidine tag. The *b*₅ cDNA cloned into the pET15b plasmid was expressed in C41(DE3) *E. coli* cells. Briefly, an overnight culture (10 mL) was used to inoculate 1 L of Terrific Broth medium containing 200 µg/mL ampicillin and 0.4% glycerol. Culture was grown with shaking at 125 rpm and 24 °C until the optical density at 600 nm reached an optical density of 1.0 at 600 nm, then IPTG (0.2 mM) was added to induce protein expression. The induced culture was incubated for another 15 h at 125 rpm and 24 °C. The bacterial cells were harvested by centrifugation at 4,000 × *g* for 20 min. The recombinant *b*₅ protein was then purified from the bacterial cell pellet as described in¹¹⁹ and using Ni-NTA affinity chromatography. Concentration of the purified *b*₅ protein was determined using an extinction coefficient of 185 mM⁻¹.cm⁻¹ between the ferrous and ferric form¹²⁰.

4.3.4 Ligand Binding Assay

Ligand binding affinities were determined by monitoring shifts in the CYP3A7 heme absorbance spectrum as described previously⁵⁴. DHEA-S (dissolved in DMSO) was titrated into 1 µM wild type or hexa-mutant CYP3A7 in 50 mM potassium phosphate, pH 7.4, 20% glycerol in a 1 cm path length quartz cuvette. Because it binds so tightly, clotrimazole (dissolved in DMSO) was titrated into 0.1 µM wild type or hexa-mutant CYP3A7 in 50 mM potassium phosphate, pH

7.4, 20% glycerol in a 5 cm path length cuvette. Each titration experiment was repeated in triplicate on different days. Changes in absorbance (absorbance maximum minus minimum) were plotted against ligand concentration and fit using the one-site specific binding equation from GraphPad Prism (version 9.3.0 for Mac OS X) (GraphPad Software, San Diego, CA) to determine the maximum absorbance change and dissociation constant.

4.3.5 Wild Type and Hexa-mutant CYP3A7 DHEA-S 16 α -Hydroxylation Kinetic Assay

The purified recombinant wild type and hexa-mutant CYP3A7 enzymes were each reconstituted in a 5x concentrated liposome premix in presence of the human CPR and cytochrome *b*₅ following the procedure described in Shaw et al.¹²¹. A 1 mg/mL liposome stock solution was prepared as 1:1:1 (v/v/v) 1,2-dilauroyl-sn-glycerol-3-phosphocholine, 1,2-dioleoyl-sn-glycerol-3-phosphocholine, 1,2-dilauroyl-sn-glycerol-3-phosphoserine. The 5x protein premix was composed of 1 μ M recombinant CYP3A7, 4 μ M human CPR and 1 μ M human cytochrome *b*₅ in 0.1 mg/mL liposomes, 3 mM glutathione, 0.5 mg/mL CHAPS and 20 mM potassium Hepes (pH 7.4). The kinetic reactions (150 μ L) were carried out by diluting the 5x protein premix in 100 mM potassium phosphate buffer, pH 7.4, and 3 mM MgCl₂, and contained a concentration range of DHEA-S (7.5-360 μ M). After an equilibration at 37 °C for 3 min, the reactions, prepared in triplicate, were initiated by the addition of a NADPH-regenerating system mix consisting of NADP⁺, glucose-6-phosphate and glucose-6-phosphate dehydrogenase (at their respective concentrations in the incubation of 1 mM, 10 mM and 2 IU/mL). The reactions, done under steady state kinetic conditions, were incubated for 30 min at 37 °C under agitation and stopped by the addition of ice-cold methanol (200 μ L) containing 50 ng/mL of estriol 3-sulfate internal standard (IS). Incubations without the NADPH-regenerating system mix served as negative controls. Precipitated proteins were collected by centrifugation of the stopped reaction samples for 20 min at 2,500 \times g and 4 °C.

Supernatants were transferred to high performance liquid chromatography (HPLC) vials, and aliquots of 5 μ L were analyzed by liquid chromatography tandem mass spectrometry (LC-MS/MS). The 16 α -hydroxy- DHEA-S metabolite was quantified based on calibration curves ranging from 1 (or 10) nM to 5000 nM.

The mean metabolite formation rate obtained from triplicate determinations were fit to the Michaelis-Menten (hyperbolic) and Hill (sigmoidal) equations using GraphPad Prism software (version 9.5.1 for Windows). Statistical analysis for the best fit was done based on the second order Akaike Information Criterion (AICc) in GraphPad Prism.

4.3.6 Analytical Method for DHEA-S Hydroxylation

The DHEA-S incubation samples with the recombinant CYP3A7 enzymes were analyzed by LC-MS/MS with a Waters Acquity Ultra-Performance liquid chromatography (UPLC) system interfaced by electrospray ionization with a Waters Xevo TQ-S micro tandem quadrupole mass spectrometer (Waters Corp., Milford, MA) operating in negative ionization mode and multiple reaction monitoring (MRM) scan type. The following source conditions were applied 0.5 kV for the capillary voltage, 150 °C for the source temperature, 450 °C for the desolvation temperature, 50 L/h for the cone gas flow and 900 L/h for the desolvation gas flow. The following mass transitions, collision energies (CEs) and cone voltages (CVs) were used to detect the respective analytes: 383 > 97 (CE = 26 V, CV = 75 V) for the 16 α -hydroxy-DHEA-S, 367 > 97 (CE = 34 V, CV = 80 V) for DHEA-S and 367 > 287 (CE = 28 V, CV = 70 V) for the internal standard estriol 3-sulfate. Analytes were separated on a Waters BEH C18 column (1.7 μ m, 2.1 \times 100 mm) by flowing 5 mM ammonium acetate in water and methanol at 0.4 mL/min. The following gradient was used: 20% organic held for 0.5 min, increased to 45% over 2.5 min, maintained at 45% for 1.5 min, increased to 98% over 1.5 min and held at 98% for 1 min. The MS peaks were integrated

using the QuanLynx software (version 4.1, Waters Corp., Milford, MA). For quantification of the hydroxy metabolite, regression fit was based on the analyte/internal standard peak area ratios calculated from the calibration standards, and the analyte concentration in the incubation was back-calculated using a weighted ($1/x^2$) quadratic least-squares regression (with $\pm 20\%$ error allowed at the low limit of quantification).

4.3.7 Crystallization and Structural Determination

Hexa-mutant CYP3A7 (25 mg/mL) in buffer (50 mM potassium phosphate, pH 7.4, 100 mM NaCl, 10% (v/v) glycerol) was saturated with 500 μ M DHEA-S. Hexa-mutant CYP3A7 crystals were grown using sitting drop vapor diffusion equilibration. The hexa-mutant CYP3A7/DHEA-S complex was equilibrated against 20% (w/v) PEG 3350, 0.2 M Lithium acetate dihydrate, pH 7.9 at 25 °C. In contrast to the previous report ¹¹⁸, sulphate was not required for crystallization and was not observed participating in intermolecular packing with the P21 space group. Crystals formed within 24 h. Crystals were cryoprotected with 70% mother liquor plus 30% glycerol and flash cooled in liquid nitrogen. Diffraction data were collected on beamline BL 9-2 of the Stanford Synchrotron Radiation Lightsource and processed using XDS ⁹⁵. The structure was solved by molecular replacement using Phaser ⁷⁰ with a hexa-mutant CYP3A7 search model (PDB entry 7MK8). Model building and refinement were performed iteratively with Coot ⁷¹ and Phenix.refine ⁷², respectively. The ligand DHEA-S was generated using elbow ⁷³ in Phenix. Figures were generated with PyMOL ¹²². Comparisons between structures were generated using the secondary structure matching algorithm ¹²³ incorporated into Coot ⁷¹. Voids were calculated using VOIDOO ⁷⁴ with a probe radius of 1.7 Å.

4.4 Results

4.4.1 Wild type and Hexa-mutant CYP3A7 Binding of Substrate DHEA-S and Inhibitor

Clotrimazole

In addition to the N-terminal truncation typically employed to facilitate human membrane P450 crystallization, crystallization of CYP3A7¹¹⁸ has additionally required the inclusion of three surface mutations (R69G, C77G, and K244E) to corresponding residues found in CYP3A4 (which does crystallize) and three mutations of long, flexible, high-entropy lysine residues on the proximal surface near where the NADPH-cytochrome P450 reductase binds (K421A, K422A, K424A). In order to assess the functional impacts of these internal mutations, ligand binding affinities were compared for this hexa-mutant and the parental construct designated as the wild type enzyme.

As often observed when substrates bind in the active site and displace the water from the heme iron, addition of the endogenous substrate DHEA-S shifted the Soret peak to shorter wavelengths for both wild type and hexa-mutant CYP3A7. Typically monitored as difference spectra collected during titration with ligand (Figure 4.1), the peak at 387-388 nm and trough at ~420 nm observed with DHEA-S addition is consistent with such a type I binding mode. Plotting the absorbance changes vs. DHEA-S concentration (Figure 4.2 A) revealed that the hexa-mutant demonstrated a 30% larger absorbance shift (λA_{\max}) and a ~2-fold higher affinity (K_d) than the wild type enzyme (Figure 4.2 E). Thus, the endogenous ligand DHEA-S binds to both wild type and hexa-mutant forms of CYP3A7, with slightly different affinities.

Both wild type and hexa-mutant were also evaluated upon addition of the non-selective inhibitor clotrimazole⁵⁴. Soret peak shifts to longer wavelengths are typically observed when the lone-pair electrons from a ligand nitrogen directly coordinate to the heme iron, replacing the water. Such type II binding was observed upon clotrimazole addition to both the wild type and hexa-

mutant CYP3A7. The difference spectra peak at 432-434 nm and the trough at 412 nm (Figure 4.1C-D) were consistent with the imidazole nitrogen heteroatom of clotrimazole coordinating the heme iron in both wild type and the hexa-mutant. Analysis of these spectral shifts (Figure 4.2 B) indicated that the extent of clotrimazole binding (λA_{\max}) was very similar for CYP3A7 wild type and hexa-mutant but the dissociation constant (K_d) was again ~ 2 -fold lower for the hexa-mutant (Figure 4.2 E).

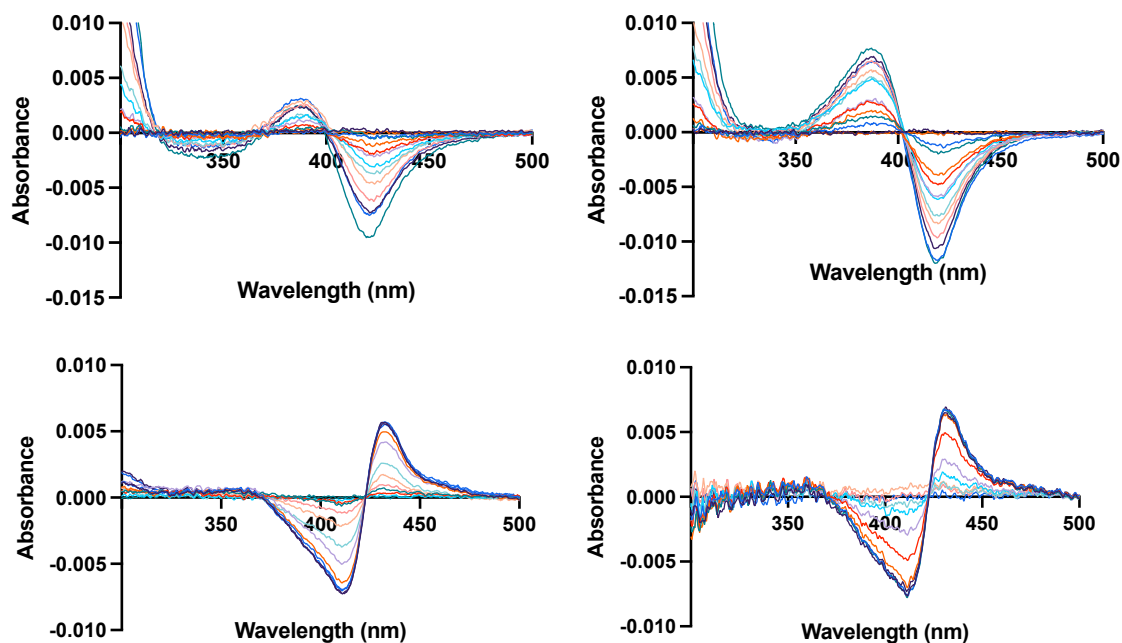


Figure 4.1 UV-vis difference spectra for CYP3A7 wild type and hexa-mutant binding of DHEA-S and clotrimazole. A) Titration of DHEA-S with wild type CYP3A7 yields a peak at 388 nm and a trough at 421.5 nm. B) Titration of DHEA-S with the CYP3A7 hexa-mutant yields a peak at 387 nm and a trough at 419 nm. C) Titration of clotrimazole with wild type CYP3A7 yields a peak at 434 nm and a trough at 412 nm. D) Titration of clotrimazole with CYP3A7 hexa-mutant yields a peak at 432 nm and a trough at 412 nm. Representative spectra shown for the triplicate titrations.

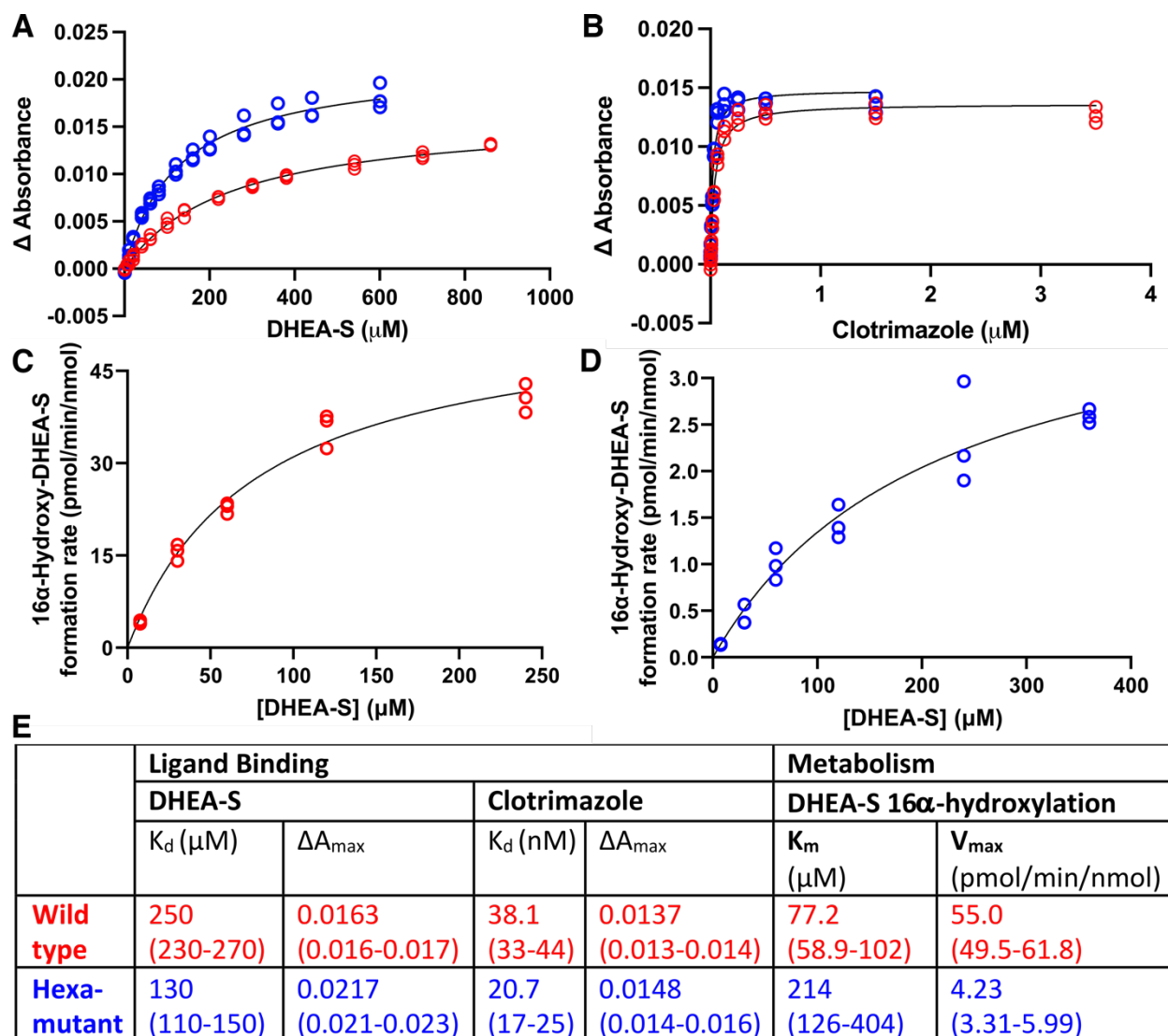


Figure 4.2 Ligand binding and DHEA-S catalysis for CYP3A7 wild type (red) and hexa-mutant (blue). A) DHEA-S type I binding is conserved but the hexa-mutant is more saturated and has a \sim 2-fold higher affinity. B) Clotrimazole type II binding is conserved and binds to a similar extent to both enzymes, but has \sim 2-fold higher affinity for the hexa-mutant. Kinetic parameters of DHEA-S 16 α -hydroxylation by C) wild type and D) hexa-mutant CYP3A7 best fit to the Michaelis-Menten equation with coefficient of determinations (R^2) of 0.979 and 0.938, respectively. E) Values for steady-state binding and catalytic parameters with 95% confidence intervals in parenthesis. All experiments were performed in triplicate.

The observation that both the DHEA-S substrate and an azole-containing inhibitor cause spectral changes with the recombinant CYP3A7 enzyme is important in that this was not observed in a previous report¹¹⁸. However, those former studies were accomplished with 1.5 μ M CYP3A7

in a buffer containing 1 mM dithiothreitol, which was later discovered to indirectly interact with the heme iron via an intervening water molecule. This type of interaction would mean that dithiothreitol binding is spectrally indistinguishable from the unliganded, water-coordinated form and the dithiothreitol could have largely outcompeted binding of ligands with lower affinities. The current results, obtained in buffer without dithiothreitol, confirmed that both the wild type and the hexa-mutant bind the DHEA-S endogenous substrate or the non-specific inhibitor clotrimazole, although the hexa-mutant showed slightly higher affinity for both ligands.

4.4.2 Kinetics of DHEA-S Metabolism

In order to further evaluate functional differences that might occur due to the internal six mutations required to crystallize CYP3A7, DHEA-S metabolism to 16 α -hydroxy-DHEA-S was also evaluated for both proteins. The wild type and the hexa-mutant CYP3A7 similarly converted DHEA-S to a single product (Figure 4.3) corresponding to the authentic 16 α -hydroxy-DHEA-S standard which was quantified with calibration standards prepared in matrix. This product was not observed when the co-factor NADPH was omitted (Figure 4.3B). Product formation rate was plotted as a function of DHEA-S concentration (Figure 4.2 C-D) and data were fitted to both the Michaelis-Menten (hyperbolic) and Hill (sigmoidal) kinetic models to obtain the kinetic parameters K_m and V_{max} (Table 4.1). The models were compared using the Akaike Information Criterion (AIC) and difference of the second-order Akaike Information Criterion (AICc) supported the simplest (Michaelis-Menten) model (Table 4.1). According to the Michaelis-Menten model, wild type CYP3A7 has a K_m of 77.2 μ M and a V_{max} of 55.0 pmol/min/nmol P450, while the hexa-mutant has a K_m of 214 μ M and a V_{max} of 4.23 pmol/min/nmol P450 (Figure 4.2 E). This suggests that the six internal mutations were detrimental to product formation, reducing the V_{max} by ~13-fold and increasing the K_m by ~2.8-fold.

Table 4.1 The difference of AICc is representative of the difference between the simpler model (Michaelis-Menten) minus the alternative model (Hill). A negative number for the difference of AICc means that the simpler model has the lower AICc and is preferred.

	Model fit	K_m/S_{50} (μM)	V_{max} (pmol/min/nmol)	R^2	Correct fit probability	Difference of AICc
Wild type	MM	77.2	55.0	0.979	76.6%	-2.38
	Hill	62.0 (n=1.2)	49.8	0.981	23.4%	
Hexa-mutant	MM	214	4.23	0.938	83.6%	-3.26
	Hill	161 (n=1.1)	3.69	0.939	16.4%	

Abbreviations: AICc, second order Akaike Information Criterion; MM, Michaelis-Menten fit; n, cooperativity value for the affinity to the enzyme.

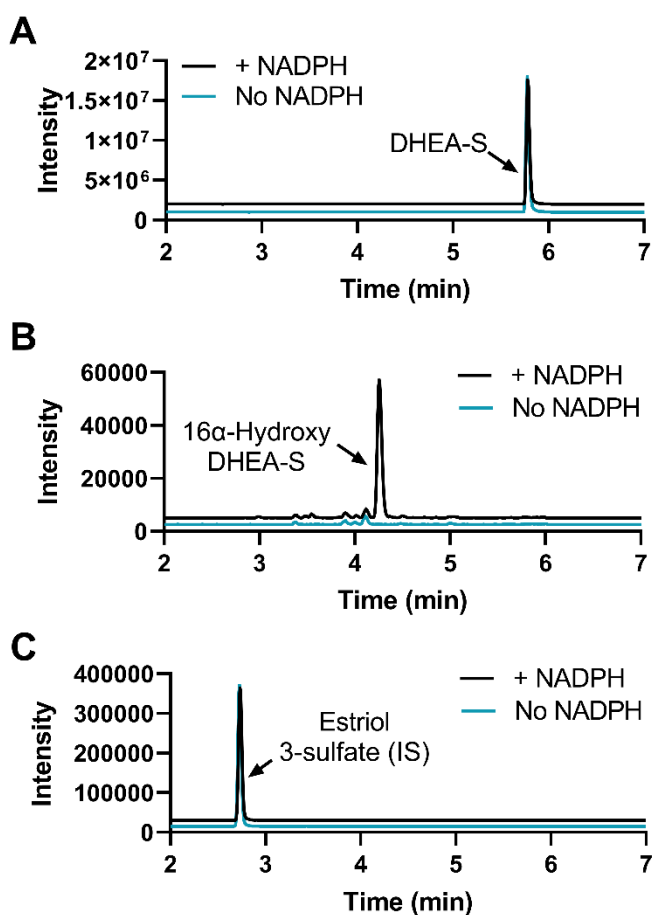


Figure 4.3. DHEA-S metabolism by CYP3A7. Representative MRM chromatograms for DHEA-S (7.5 μM) (A), its 16 α -hydroxy metabolite (B) and the internal standard estriol 3-sulfate (C) in incubations with the wild type CYP3A7 in the presence and absence of the co-factor NADPH.

4.4.3 Structure of Hexa-mutant CYP3A7 Co-crystallized with DHEA-S

Human CYP3A7 modified by truncation of the N-terminal transmembrane helix and addition of a His-tag at the C-terminus like almost all other crystallized human P450 enzymes is recombinantly expressed in good yields and highly purified with good stability but has been resistant to crystallization despite significant efforts by multiple labs. Only recently was the first CYP3A7 structure reported after incorporating six amino acid mutations in the catalytic domain¹¹⁸. This structure did not include relevant substrates or inhibitors, but the CYP3A7 active site did contain an adventitious dithiothreitol molecule. Herein the same hexa-mutant CYP3A7 protein described in¹¹⁸ was generated and co-crystallized with its native substrate DHEA-S, yielding suitably sized rhombic plates. X-ray data was collected from a single crystal, solved by molecular replacement, and refined (Table 4.2) to yield a 2.6 Å structure.

Table 4.2 X-ray data collection, refinement, and validation statistics.

Parameter	Hexa-mutant CYP3A7/DHEA-S
Data collection	
Space group	P 2 ₁
Cell dimensions	
<i>a</i> , <i>b</i> , <i>c</i> (Å)	114.52, 219.38, 130.45
<i>α</i> , <i>β</i> , <i>γ</i> (°)	90, 102.17, 90
Resolution (Å)*	39.94-2.60 (2.74-2.60)
Redundancy*	7 (6.9)
<i>R</i> _{pim} *	0.046 (0.878)
Mn(I/sd)*	10.3 (1.0)
CC ½*	0.999 (0.473)
Completeness* (%)	99.1 (98.4)
Total Reflections	1,342,003
Unique Reflections	190,994
Refinement	
Resolution (Å)	39.94-2.60 (2.74-2.60)
No. reflections	1,342,003
<i>R</i> _{work} / <i>R</i> _{free}	0.21/0.27
Molecules per asymmetric unit	12
Number of non-hydrogen atoms / B factor	
Protein	45,416/78
Ligand	600/81

Heme	588/71
Water	32/43
Root mean square deviations	
Bond lengths (Å)	0.011
Bond angles (°)	1.2
Coordinate error (Maximum-likelihood) (Å)	0.50
Ramachandran plot:	
preferred/allowed/outliers (%)	92.03/7.46/0.51

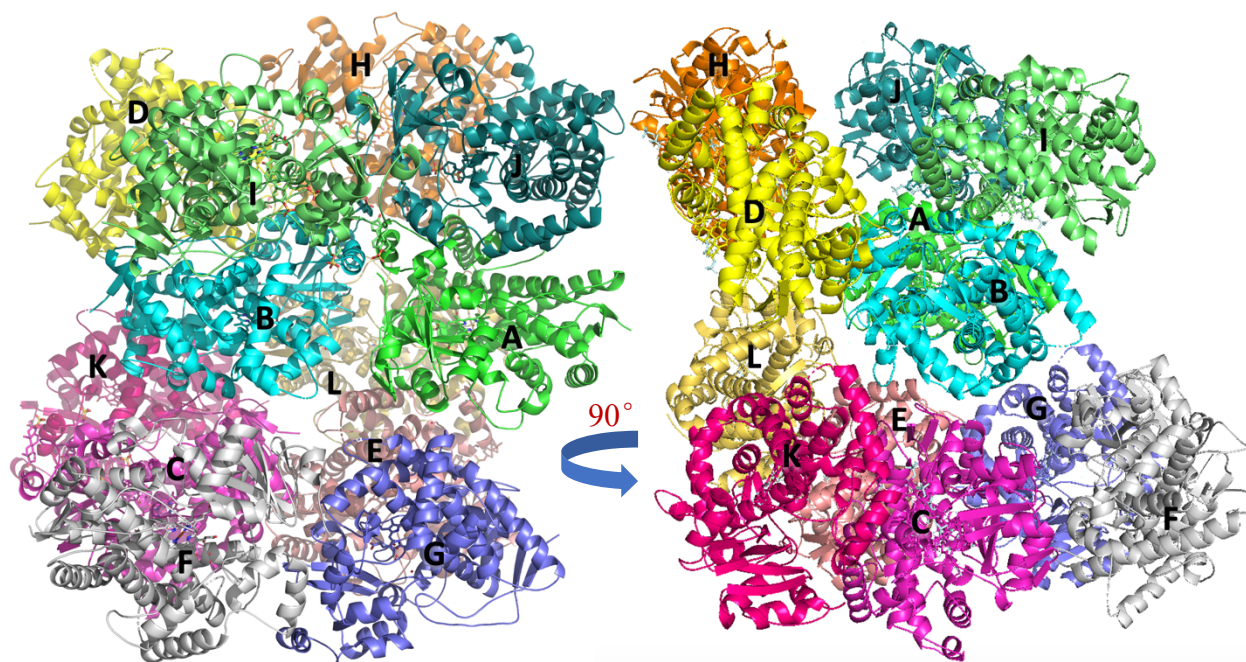


Figure 4.4 Arrangement of 12 molecules shown in two directions. Each molecule is in a unique color with label in black.

As observed previously¹¹⁸, the CYP3A7 hexa-mutant adopted a typical P450 fold with the three CYP3A4-mimicking mutations in the β 1 loop region (R69G and C77G) and G helix (K244E) and the reductase-binding region mutations (K421A, K422A, and K424A) on the K-L loop region (Figure 4.5 A). Of the 12 copies of the hexa-mutant CYP3A7 protein in the asymmetric unit, two distinct types of CYP3A7 molecules were observed. Six molecules (molecules A, B, F, G, K, L) did not have any density present for a ligand (Figure 4.5 A). The remaining six molecules (molecules C, D, E, H, I, and J) *each* had *four* DHEA-S molecules which were readily modeled

with 100% occupancy (Figure 4.5 B). Two DHEA-S molecules were in the active site proper, one closer to the heme (DHEA-S1) than the other (DHEA-S2), one in a channel between the active site and the surface (DHEA-S3), and one on the protein surface (DHEA-S4) (Figure 4.5 B). The arrangement of 12 molecules and crystal packing were shown in Figure 4.4. Seven distinct types of crystal contacts were observed in this assembly. The first two types of interactions involve the dimerization of two liganded molecules. One interface is located on the β 1- β 2 strands of the two molecules, where a salt bridge is formed through the K390 and D380 side chains (Figure 4.6 A). The other interface occurs on the D helix side of the protein. Here, the side chain of N341 from the J-K loop of one molecule forms a hydrogen bond with the P147 ketone backbone of the D helix on the other molecule (Figure 4.6 B). Some additional crystal contacts are present, but they are not well-defined due to the flexibility of the side chains. Two additional interactions involve the dimerization of two unliganded molecules. One interaction is facilitated by hydrophobic contacts between the two parallel G' helices of the two molecules (Figure 4.6 C). Another interaction interface is located at the D helices and J-K loops, both perpendicular to each other, within the two molecules. In this scenario, the N341 side chain of the J-K loop forms hydrogen bonds with the N341 and K342 backbone ketones (Figure 4.6 D). As before, some additional interactions are not well-defined due to the flexibility of the side chains on the protein surface. The final two interactions occur between the liganded and unliganded molecules. The first type of interaction transpires at the interface of the F and F' helices in both molecules, where they form hydrophobic interactions (Figure 4.6 E). The second interaction takes place at the interface of the two perpendicular A helices of the molecules. Here, the E63, K66, and K67 side chains of the unliganded molecule bond with the backbone amide and ketone groups of the β 1, A helix, and A'' helix, respectively, in the liganded molecule (Figure 4.6 F) The last interaction is observed between

the B helix of the liganded molecule and the D helix of the unliganded molecule, where the D88 side chain of the liganded molecule forms a salt bridge with the K143 side chain of the unliganded molecule (Figure 4.6 G).

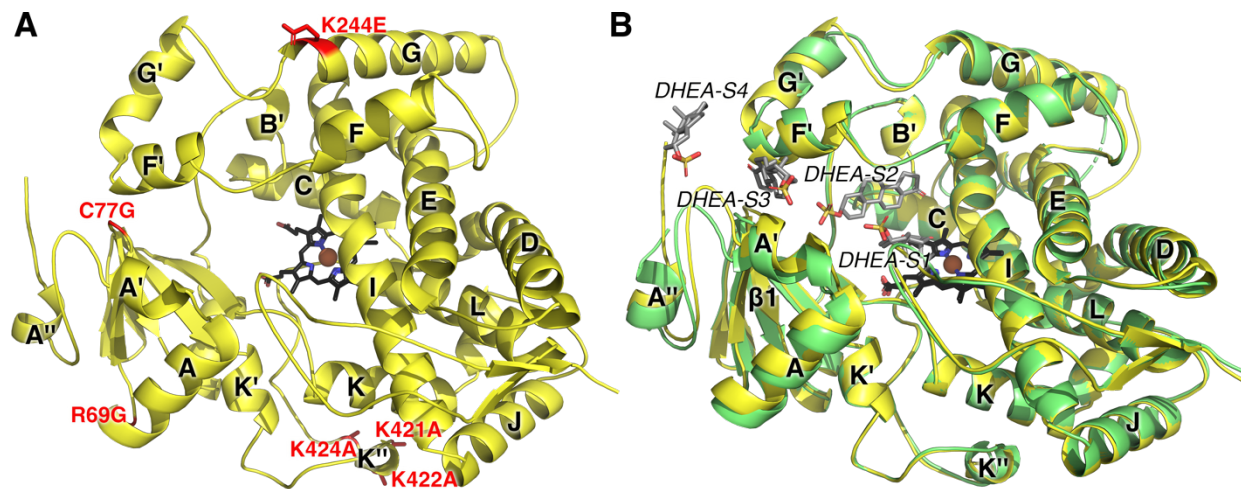


Figure 4.5 Hexa-mutant CYP3A7 structural overview. A) Representative ligand-free molecule with the positions of the K421A/K422A/K424A/R69G/C77G/K244E mutations shown in red sticks. B) Comparison of a ligand-free molecule (yellow ribbons) with a molecule (green ribbons) containing four copies of DHEA-S (shown in sticks with grey carbons). Heme in black sticks with rust sphere for iron.

Pairwise comparisons of CYP3A7 molecules containing DHEA-S ligands (Figure 4.5 B, green) and those without ligand (Figure 4.5 B, yellow) consistently yielded $C\alpha$ root mean square deviations (rmsd) of 0.66-0.85 Å (Table 4.3), while comparisons between ligand-free molecules had rmsd values of 0.35-0.6 (Table 4.3) and comparisons between molecules containing DHEA-S had rmsd values of 0.26-0.39 (Table 4.3). The most significant differences between the liganded and unliganded structures were observed in helices A, A', B, F', G', and G and β 1-2 (Figure 4.5 B). The F', G', and G helices shift slightly in the opposite direction from the A, A', B, and β 1-2 secondary structure elements, slightly opening up the channel at the level of DHEA-S3. However large ligand-triggered structural changes in the backbone were not observed.

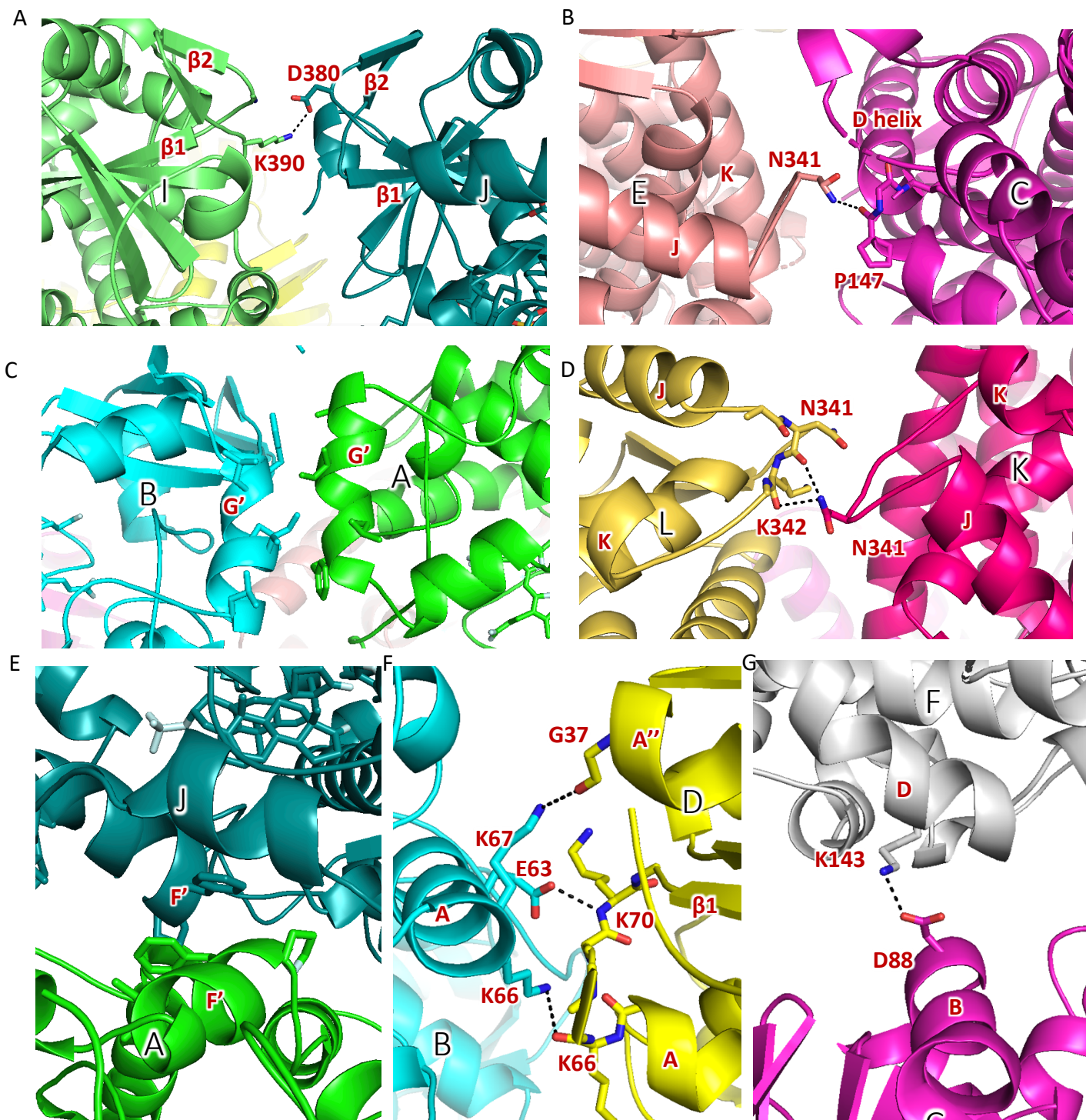


Figure 4.6 Seven distinct crystal contacts observed in CYP3A7 structure. Interactions between (A) molecule I and J through a salt bridge, (B) molecule E and C through hydrogen bonding, (C) molecule B and A through hydrophobic interactions, (D) molecule L and K through hydrogen bonding, (E) molecule A and J through hydrophobic interactions, (F) molecule B and D through hydrogen bonding, and (G) molecule C and F through a salt bridge. Molecule name is label in black. Secondary structures and residue names are labeled in red.

Table 4.3 Ca root mean square deviations (rmsd) between each two molecules (A-L) of CYP3A7 structure.

	A	B	C	D	E	F	G	H	I	J	K	L
A		0.3564	0.7531	0.7236	0.7249	0.3516	0.4108	0.7455	0.7539	0.7436	0.3654	0.5283
B	0.3564		0.6662	0.6777	0.6697	0.3598	0.3574	0.6953	0.6927	0.685	0.3928	0.4926
C	0.7531	0.6662		0.3614	0.3112	0.7235	0.7211	0.2888	0.3863	0.2615	0.7098	0.8181
D	0.7236	0.6777	0.3614		0.3312	0.7141	0.7256	0.3904	0.3441	0.3543	0.7198	0.8309
E	0.7249	0.6697	0.3112	0.3312		0.7167	0.6926	0.3293	0.3252	0.3056	0.7216	0.8025
F	0.3516	0.3598	0.7235	0.7141	0.7167		0.4004	0.7573	0.7379	0.7389	0.3643	0.5251
G	0.4108	0.3574	0.7211	0.7256	0.6926	0.4004		0.7456	0.726	0.726	0.4427	0.479
H	0.7455	0.6953	0.2888	0.3904	0.3293	0.7573	0.7456		0.2831	0.3163	0.7385	0.8464
I	0.7539	0.6927	0.3863	0.3441	0.3252	0.7379	0.726	0.2831		0.3125	0.7634	0.8373
J	0.7436	0.685	0.2615	0.3543	0.3056	0.7389	0.726	0.3163	0.3125		0.7493	0.8236
K	0.3654	0.3928	0.7098	0.7198	0.7216	0.3643	0.4427	0.7385	0.7634	0.7493		0.602
L	0.5283	0.4926	0.8181	0.8309	0.8025	0.5251	0.479	0.8464	0.8373	0.8236	0.602	

The DHEA-S ligands are all well defined by the electron density (Figure 4.7 A), but each has distinct interactions with the protein. Closest to the heme, DHEA-S1 (Figure 4.7 B) is located 4.1 Å above the heme Fe. Its C17 ketone is directed toward heme iron and the C3 sulfate projecting toward the β 4 region. The backbone amide of β 4 G481 is positioned to hydrogen bond (2.5 Å - 3.1 Å) with either of the two oxygen atoms of the DHEA-S1 sulfate. The distance from the site of metabolism, C16, to the heme iron is 5.8 Å (Figure 4.7 B). The rest of the interactions with DHEA-S1 are largely hydrophobic. Residues within 4 Å of DHEA-S1 include: Y57, R105, S119, N214, P215, L216, A305, T309, V369, A370, G480, G481, and L482 (Figure 4.7 C). DHEA-S2 is located above DHEA-S1 in the active site (Figure 4.7 B). The distance from its C17 ketone to the heme iron is 8.7 Å (Figure 4.7 B). The long axis of its steroid nucleus is parallel with the F helix. One side of its steroidal core packs against P215 in the loop between F and F', while the side chain of F108 in the loop between B and B' packs against the opposite side (Figure 4.7 C). One oxygen of the DHEA-S2 sulfate hydrogen bonds with the side chain amino group of K224 (2.6-3.2 Å, Figure 4.7 C). Only one of the CYP3A7 molecules (molecule D) containing DHEA-S suggests that another oxygen atom of this sulfate can form a hydrogen bond with the side chain guanidinium group of R106 (2.65 Å, Figure 4.7 C). Residues within 4 Å of DHEA-S2 include: D76, R105, R106, F108, S119, I120, F213, P215, V220, K224, F241, I301, F304, and E374 (Figure 4.7 C).

DHEA-S3 lies in the access channel close to the protein surface between the A' and F' helices with the ketone at C17 directing towards the F' helix (Figure 4.7 D). The C3 sulfate extends to the surface where one of its oxygen atoms is in position to hydrogen bond (~ 2.6 Å) with the side chain guanidinium group of R243 in an adjacent molecule (Figure 4.7 C). Residues within 4 Å of DHEA-S3 include: F46, L47, A50, L51, and R54 from helix A, D76 from the $\beta 1$ system, amino acids L221, K224, and V225 from helix F', and residues N237, I238, and R243 from the adjacent molecule (Figure 4.7 C). Finally, DHEA-S4 is located above the protein surface next to helices A and F' at the interface between adjacent or symmetry-related molecules (Figure 4.7 C). One sulfate oxygen atom of DHEA-S4 forms a hydrogen bond with the backbone amide of G26 in the adjacent or symmetry-related protein molecule, but the majority of the interactions appear to be hydrophobic. Residues within 4 Å of DHEA-S4 include: P45, F46, and L47 from helix A', V225 and F226 from F', and I232, A235, and L236 from the adjacent protein molecule (Figure 4.7 C). This hydrophobic surface is thought to be embedded in the endoplasmic reticulum membrane.

In addition to the primary channel containing the DHEA-S molecules (Figure 4.7 D, channel 1), three other channels are apparent from the active site to the protein surface (Figure 4.7 D). One channel exits between the B-B' loop and B'-C loop (channel 2). Another passes between the F and I helices (channel 3), and the last one between the B-B' loop and $\beta 1-1$ (channel 4).

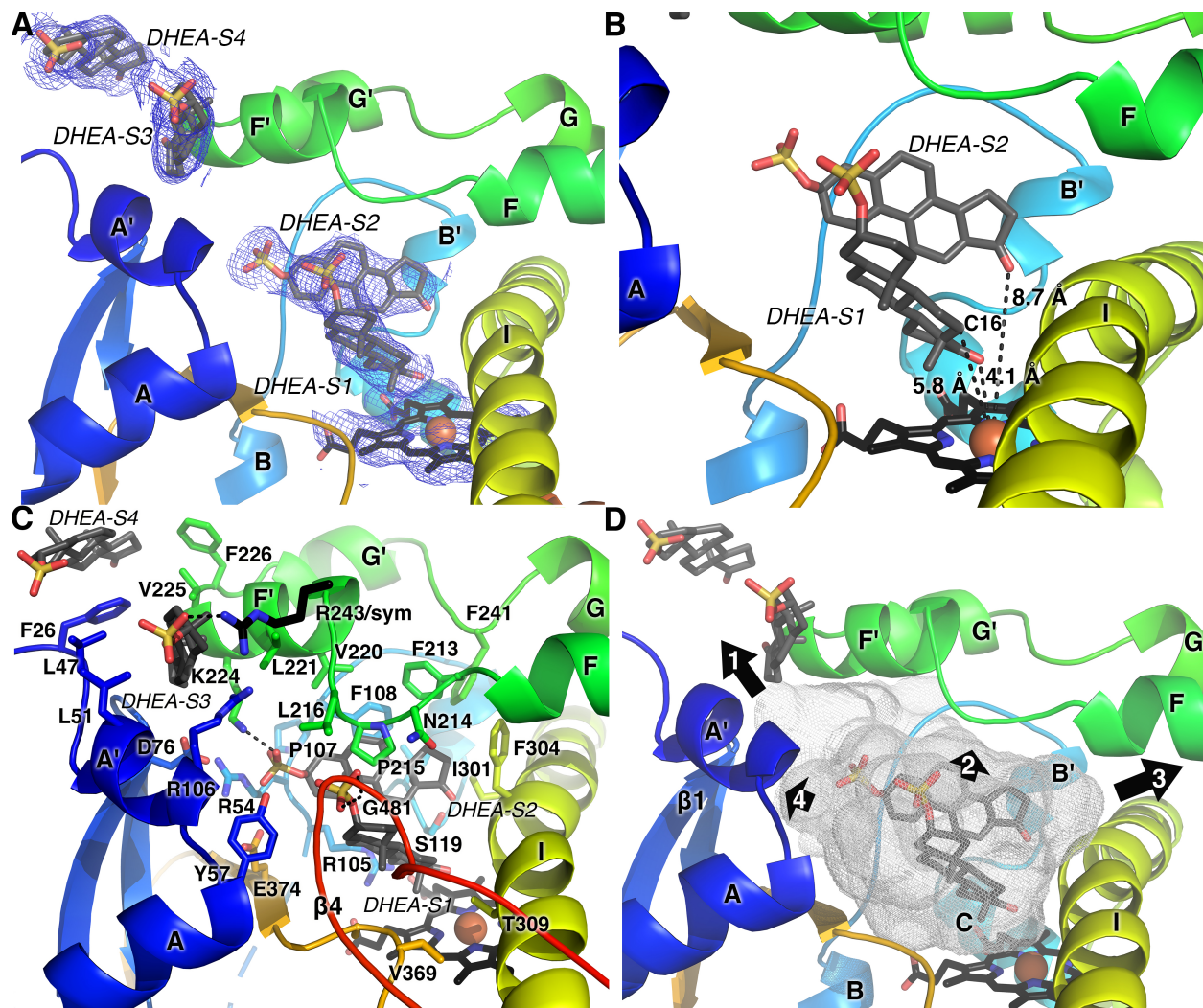


Figure 4.7 Interactions of the DHEA-S substrates (sticks with grey carbons) with the CYP3A7 hexa-mutant (rainbow ribbons from blue N-terminus to red C-terminus). A) Strong electron density (simulated annealing composite omit at 1σ) defines the positioning of all four molecules of the substrate DHEA-S. B) The DHEA-S closest to the heme (DHEA-S1) is oriented with its C17 carbonyl directed toward the heme iron. The second DHEA-S molecule (DHEA-S2) also binds in the active site cavity (grey mesh) but in a different orientation. C) Residues within 4 Å of any of the DHEA-S molecules are shown as sticks, with key sulfate-protein interactions indicated by dashed lines. The sulfate of DHEA-S3 extends to the surface and interacts with Arg243 of a symmetry-related molecule (black sticks). D) Channels from the active site to the protein exterior are indicated by black arrows 1-4.

4.5 Discussion

The first CYP3A7 structure, that of the same hexa-mutant used herein, had two nearly identical molecules ($C\alpha$ rmsd 0.345), both with the buffer component dithiothreitol in the active

site but not directly interacting with the heme or polypeptide ¹¹⁸. The crystal packing differs slightly between the two structures. The CYP3A7/DTT structure contains only two protein molecules in the asymmetric unit ¹¹⁸, whereas our structure hosts 12 molecules. Two types of crystallographic dimers were identified in the DTT structure. One contact area is constituted by the hydrophobic residues from the antiparallel G'-helices, which is also observed in our structure. Another interface is formed by the antiparallel D-helices with a sulfate ion situated in between, linking the two helices via hydrogen bonds and salt bridges. In our structure, we also identified an interface at the D-helix region, but in our case, the two D-helices are oriented perpendicularly to each other. Hydrogen bonds are found either between the D-helix and J-K loop or between both J-K loops in the two molecules. Our structure also presents additional interfaces involving two F-F' regions and A-helices. The discrepancies in crystal packing between the two structures are likely attributed to the different ligands they co-crystallized with. These ligands possibly induce conformational changes in CYP3A7, altering the homogeneity of the protein during crystallization. Superimposing the dithiothreitol structure and representative ligand-free and 4xDHEA-S conformations determined herein results in C α rmsd values of 0.44 Å and 0.723 Å, respectively. Thus, few structural differences occur between the ligand-free and dithiothreitol structures despite different crystallization conditions, different space groups, and different packing interactions in the crystalline lattice. While the C77G, K421A, and K424A mutations did not form intermolecular contacts between molecules in the dithiothreitol complex, herein five of the mutated residues were involved in intermolecular contacts, with the exception being C77G. Regardless, the most substantial differences between the dithiothreitol and 4xDHEA-S structures occur in helices A', B', F', F, G', and G, β 1-1, β 1-2, and their loop regions (Figure 4.8 A). These helices, β sheets and

loops all slightly move outwards to open up the main channel where DHEA-S binds, but particularly in the region of DHEA-S3 (Figure 4.8 A).

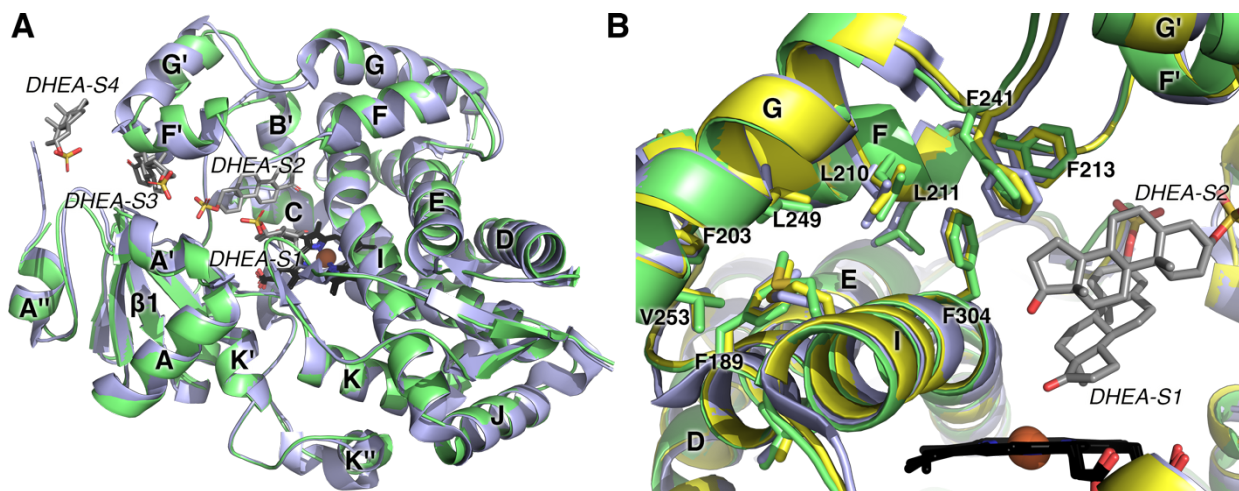


Figure 4.8 Comparisons of CYP3A7 hexamutant structures determined with different liganded states. A) The structure with four DHEA-S molecules bound (green) is quite similar to the previous structure determined with the adventitious ligand dithiothreitol (slate). B) Comparison of the previous dithiothreitol (154 g/mol) complex (slate), the DHEA-S (288 g/mol) complex (green) and the ligand-free structure (yellow) reveal remarkably little changes in active site residue rotamers (DTT not shown).

One feature reported in the previous dithiothreitol structure was that F304 in the CYP3A7 I helix flanking the active site adopts a rotamer positioning the aromatic ring toward the F'/G' active site “roof” where it interacts with two leucines and two other phenylalanines from those structural elements. This was notable because F304 adopts different rotamers in CYP3A4 and CYP3A5. Depending on the size of the active site ligand, different F304 rotamers are observed and it is thought to be a gatekeeper for access of larger ligands into the active site proper. However, comparison of F304 in all three structures now available show that F304 maintains its upward rotamer forming part of this hydrophobic patch (Figure 4.8 B) including residues F189, F203, L210, L211, F213, L249, V253, F241, L295, and M296. This feature of CYP3A7 and related interactions have been suggested to confer greater rigidity to CYP3A7¹¹⁸ associated with decreased substrate metabolism compared to CYP3A4.

The structure herein definitively demonstrates that the hexa-mutant CYP3A7 binds four copies of DHEA-S simultaneously, two in the active site, one in a channel to the surface, and one at the membrane-binding surface. A relevant question is whether this is also the case for the wild type CYP3A7 in the absence of the six internal mutations.

DHEA-S1 is buried in the active site cavity adjacent to the heme and surrounded by highly hydrophobic side chain residues from helices A, F, G, and I and β 1. This active site is exactly where one would expect to find substrate binding and DHEA-S1 is additionally oriented with the C16 site of observed metabolism directed toward the heme iron as would be required for 16α -hydroxylation. This occurs even though there are not notable specific interactions between DHEA-S1 and side chains lining the active site, only the backbone of the β 4 loop. Since DHEA-S1 is closest to the heme iron, this ligand is most likely primarily responsible for the spin change observed as a spectral shift in the DHEA-S binding studies. However, even though the nearest mutation K244E is 25.9 Å away from DHEA-S1, clearly one or more of the ligands indirectly facilitate this spin change because the affinity and saturation as measured by spectral shift are somewhat greater in the hexa-mutant than in the wild type (Figure 4.2 A). Based on proximity and relative orientation, it appears that the presence of DHEA-S2 could facilitate positioning of DHEA-S1 near the iron. If DHEA-S2 were not present, DHEA-S1 would certainly have more freedom to move about large active site cavity, however no evidence of cooperativity was observed in the binding studies consistent with the multiple ligand active site binding model¹²⁴. This may be because the binding of DHEA-S1 and DHEA-S2 are totally independent and binding of one (likely DHEA-S2) is spectroscopically silent. There are other examples of cytochrome P450 enzymes with more than one ligand in the active site, including steroids or synthetic sterol dimers¹²⁵. While this would not explain the lack of observed cooperativity in the DHEA-S oxidation

studies, such catalysis is further complicated by the involvement of cytochrome P450 reductase and cytochrome *b*₅, making a direct comparison of affinities and stoichiometries difficult.

Binding of DHEA-S3 in the channel and DHEA-S4 on the surface were somewhat unexpected and also likely to be spectroscopically silent. The binding site for DHEA-S3 is closest to one of the mutations. DHEA-S3 is located directly above the C77G mutation site on β 1 loop region (Figure 4.5 A and 4.5 B). When the six mutations were modeled back to the corresponding wild type residues, most were easily accommodated. However, regardless of the rotamer modeled, a clash was observed between the Cys77 side chain and DHEA-S3. Thus it is possible that either the wild type enzyme might be incompatible with the binding of DHEA-S3 in the access channel or the wild type might undergo a conformational change to opening up the ligand access channel slightly to accommodate DHEA-S3. It is possible that the cysteine side chain might clash with DHEA-S3. However this primary channel is very similar in CYP3A4 and CYP3A5 without these internal mutations¹¹⁸. DHEA-S4 is located on the protein surface adjacent to the F' and G' helices. The side chains on the outside of these two short helices and the loop in between are highly hydrophobic, which provide a favorable environment for DHEA-S4 to bind. Surrounding the other sides of DHEA-S4 is the same region of four adjacent molecules in the crystalline lattice. Without the convergence of these intermolecular contacts, a large part of DHEA-S4 would be exposed to the hydrophilic solvent and, therefore the binding of DHEA-S4 on the protein surface might be disrupted. However, in the native environment, this hydrophobic surface of the F'-G' region is thought to be embedded in the hydrophobic core of the endoplasmic reticulum membrane and likely to be the dynamic region whereby hydrophobic substrates like steroids pass from the membrane into the cytochrome P450 active site. A number of membrane P450 enzymes have now been observed with channels in the same structural region as the one filled with DHEA-S

molecules here. An early structure of the 87% identical adult CYP3A4 enzyme also defined the steroid progesterone binding site on its F'-G' surface (PDB 1W0F¹²⁶). In that structure the oxygen of progesterone's acetyl side chain hydrogen bonded with the amide nitrogen of D214 in the F-F' loop. This binding area was proposed to serve as an effector or substrate binding site in the original publication¹²⁶. This idea is consistent with a significant body of functional data indicating that CYP3A4 demonstrates both heterotropic and homotropic cooperativity, often with steroids. Testosterone can bind cooperatively to CYP3A4¹²⁷. Progesterone¹²⁸, testosterone¹²⁹, and 17 β -estradiol¹²⁹ metabolism all demonstrate homotropic cooperativity, while progesterone heterotropically stimulates estradiol¹³⁰ and carbamazepine¹³¹ metabolism. Site-directed mutation results also support the importance of this peripheral binding site as mutation of L211 and D214 to Phe and Glu, respectively, affects progesterone cooperativity in both binding and metabolism¹³². Thus, substantial experimental evidence supports progesterone high affinity binding on the peripheral surface and its role as a CYP3A4 allosteric activator, enhancing CYP3A4 activity towards other substrates¹³³

Much less information is available regarding the phenomenon of cooperativity in CYP3A7 catalysis. Herein the internal mutations clearly cause a ~13-fold decrease in the V_{\max} and 3-fold increase in the K_m for DHEA-S 16 α -hydroxylation. This is not surprising as three of the mutations to promote crystallization (K421A/K422A/K424A) are part of the proximal surface where electrostatic interactions with NADPH-cytochrome P450 reductase allow it to bind and deliver electrons required for catalysis. When electrons are delivered using cumene hydroperoxide as an alternate, the kinetic constants are similar to the wild type enzyme¹¹⁸. Despite this reduced activity for the hexa-mutant, neither it or the more-active wild type CYP3A7 demonstrated sigmoidal steady-state kinetics; the data yielded a hyperbolic curve best fit to the Michaelis-Menten equation

rather than a cooperative model with a Hill coefficient (Figure 4.2 and Table 4.1). Examination of higher concentrations were limited by substrate solubility and lower concentrations by relatively low turnover, but a previous report similarly reported that DHEA-S metabolism was hyperbolic¹³⁴.

However this same report also discovered that the presence of DHEA-S strongly activated CYP3A7-mediated 10,11-epoxidation of the anticonvulsant carbamazepine (5*H*-dibenzo[*b,f*]azepine-5-carboxamide) in a concentration-dependent manner¹³⁴. This report concluded that while DHEA-S and carbamazepine are both substrates, they do not inhibit each other's metabolism. However, DHEA-S decreases the K_m of carbamazepine 3-fold, indicating that one molecule of each substrate could be present simultaneously in the CYP3A7 active site and that either a conformational change induced by DHEA-S or an interaction between DHEA-S and carbamazepine in the active site could be implicated. Carbamazepine is a fused aromatic planar molecule with a molecular weight of 236 g/mol and is thus similar in size and shape to DHEA-S. Thus, the current structure suggests it could bind similarly to one of the two DHEA-S molecules observed in the active site, which would support the multiple ligand active site model. It is also possible that one of the outer DHEA-S3 or DHEA-S4 molecules indirectly alters carbamazepine metabolism in the active site, analogous to progesterone in CYP3A4. However, the authors of the previous study found that the sulfate of DHEA-S was critical in decreasing the K_m for carbamazepine. While DHEA-S3 and DHEA-S4 sulfates do not directly interact with the CYP3A7 monomer, the sulfate of DHEA-S2 makes a direct interaction with Lys224 or R106 in the F' and B' helices, respectively. Both F' and B' are dynamic regions thought to be involved in sequestering ligands in the active site.

4.6 Conclusion

DHEA-S is present in high concentrations in the fetal and neonatal periods and when xenobiotics including drugs are also present, their CYP3A7 intersection could lead to issues multiple different ways. First, it is possible that high DHEA-S levels could competitively inhibit CYP3A7-mediated metabolism of drugs. e.g., Nakamura et al.¹³⁴, suggested the effect of endogenous DHEA-S on CYP3A7-mediated drug metabolism may not be uniform. Second, drugs inhibiting CYP3A7 could interfere with DHEA-S metabolism and lead to renal insufficiency in the neonate and developing infant, leading to adverse effects. Finally, environmental xenobiotics activated by CYP3A7 or cleared by CYP3A7 may play important roles in fetal exposure. Therefore, the structure herein is a step forward toward understanding the complex interactions of CYP3A7 with its primary substrate and identifies multiple binding site that may interact with each other and with other substrates bound simultaneously, but numerous CYP3A7/ligand interactions remain to be examined before this information can be translated to improve pediatric pharmacology.

Chapter 5 Cytochrome P450 27A1

5.1 Summary

Cytochrome P450 27A1 (CYP27A1), also known as sterol 27-hydroxylase, plays a crucial role in the metabolism of cholesterol and other sterols in the body. Specifically, it catalyzes the conversion of cholesterol into 27-hydroxycholesterol, which is then used as a precursor to produce bile acids. Recent studies have also recognized CYP27A1 as a novel drug target for estrogen receptor alpha (ER α) positive breast cancer. The CYP27A1 27-hydroxycholesterol product behaves as a selective estrogen receptor modulator. It has agonist activity in breast cancer cells and is capable of promoting the growth of ER-positive tumors. However, currently there is no CYP27A1 selective inhibitor and no CYP27A1 structure to direct such inhibitor design. Herein, human CYP27A1 was expressed and purified for use in ligand binding and crystallization experiments. Ligand binding analysis of substrates, common P450 inhibitors, and other commercially available drugs identified multiple ligands with submicromolar affinity. While initial crystallization efforts have been unsuccessful to date, the preliminary research described herein has laid the groundwork for future structural and functional investigations of the CYP27A1 active site, with the goal of enabling design of selective CYP27A1 inhibitors for the treatment of ER-positive breast cancer.

5.2 Introduction

CYP27A1 is a mitochondrial enzyme responsible for the hydroxylation of cholesterol, bile-acid intermediates, and vitamin D₃ in the C27 position, serving a crucial role in the metabolism of cholesterol and other sterols in the human body. Cholesterol 27-hydroxylation initiates the alternative bile acid synthesis pathway (Figure 1.6) and has a significant role in cholesterol homeostasis.

Emerging research indicates a possible link between CYP27A1 and breast cancer, and the role of CYP27A1 appears complex and multifaceted. The enzyme appears to contribute to the development and progression of this disease through its interaction with various pathways related to cancer cell growth, proliferation, and migration^{35, 36}. The 27-hydroxycholesterol, primary CYP27A1 metabolite is an endogenous selective estrogen receptor modulator that can drive the growth of breast cancer cells¹³⁵. This is particularly significant in ER-positive breast cancer, which makes up about 70% of all breast cancers and relies on estrogen to grow. In this way, high levels of 27-hydroxycholesterol could potentially drive the growth of these cancers, even in the presence of estrogen-blocking therapies. Additionally, 27-hydroxycholesterol, through its activation of liver X receptors, can influence immune response within the tumor microenvironment¹³⁶. High levels of 27-hydroxycholesterol have been linked with decreased cytotoxic T cell response, which is critical in combating tumor growth. By dampening the immune response, high levels of 27-hydroxycholesterol may contribute to immune evasion by cancer cells, promoting tumor progression and metastasis¹³⁶. Furthermore, recent studies have indicated that when breast carcinoma MCF7 cells are exposed to 27-hydroxycholesterol, they exhibit lower expression of E-cadherin and β -catenin¹³⁷. These findings suggest that 27-hydroxycholesterol may play a role in the development of epithelial-mesenchymal transition, a process associated with cancer

progression and metastasis. In addition, increased concentrations of 27-hydroxycholesterol have been reported in both plasma and breast cancer tissues in in vivo models³⁶. This underscores the potential significance of 27-hydroxycholesterol generated by CYP27A1 in the pathophysiology of breast cancer, emphasizing the need for further investigation into these interactions and their implications for breast cancer prognosis and treatment.

In summary, CYP27A1, through its role in cholesterol metabolism and particularly through its production of 27-hydroxycholesterol, may contribute to the growth, immune evasion, and metastasis of breast cancer cells. It has been reported that breast cancer metastasis was reduced in mice with a myeloid specific knockout of CYP27A1¹³⁶. This suggests that it could serve as a potential therapeutic target. Previous studies have expressed and purified CYP27A1^{138, 139}, explored CYP27A1's function in cholesterol metabolism¹⁴⁰, and its ligand interactions with commercially available drugs^{141, 142}, contributing valuable insights into its biological role and potential as a therapeutic target. Despite this, as of previous research, no selective inhibitor has been developed for CYP27A1 and no structure to facilitate such inhibitor design to explore clinical applications. Herein, I successfully expressed and purified human CYP27A1, and identified some CYP27A1 tight-binding ligands for co-crystallization, which often facilitate the generation of crystal formation and lead to the first CYP27A1 X-ray structure. This information should promote the design of more selective CYP27A1 inhibitors and allow the exploration of this strategy to treat ER α positive breast cancer.

5.3 Experimental procedures

5.3.1 Expression and purification of CYP27A1

The human CYP27A1 cDNA was synthesized with codon optimization for *E. coli* expression (Genscript, Piscataway, NJ). Nucleotides coding for wild type amino acids 1-25 were truncated

and replaced with nucleotides coding for the sequence MAKKTSS. Nucleotides were also added at the C-terminus to code for a six-residue histidine tag just prior to the stop codon. The resulting sequence was cloned into the pCWori+ vector.

The resulting pCWCYP27A1dH6 plasmid was transformed into *E. coli* DH5 α cells already containing the pGro7 plasmid for expressing the GroES-GroEL chaperone complex (Takara Bio, San Jose, CA) and plated on a lysogeny broth (LB) agar plate containing 100 μ g/ml carbenicillin for pCWori+ selection and 20 μ g/ml chloramphenicol for pGro7 selection and grown at 37 °C overnight. A single colony was then inoculated into 5 mL LB media with the same antibiotics and grown for 6-8 hours at 37 °C with shaking. A 50 μ L sample of this culture was then introduced into 200 mL LB media and grown overnight with the same antibiotics, with shaking at 37 °C. For expression 900 ml of terrific broth (TB) with 2 \times potassium phosphate buffer and the same antibiotics in a 2.8-liter Fernbach flask were inoculated with 20 ml of the overnight culture. This culture was incubated at 37 °C and 220 rpm until an optical density at 600 nm (O.D.₆₀₀) of 0.4–0.6 was reached. At that point, 1 mM δ -aminolevulinic acid and 4 mg/mL arabinose were added as a heme precursor and to induce expression of the *groES-groEL* genes, respectively. When an O.D.₆₀₀ of 0.8 was reached, CYP27A1 expression was induced with 1 mM isopropyl β -D-1-thiogalactopyranoside. The temperature and shaking were reduced to 25 °C and 190 rpm for 48-66 hours, after which bacterial cells were pelleted by centrifugation at 6,930 x g at 4 °C for 10 min. The cell pellet was resuspended in resuspension buffer (500 mM potassium phosphate buffer, pH 7.4, 20% (v/v) glycerol, 500 mM sodium chloride) containing 2 tablets of SigmaFast protease inhibitor (Millipore Sigma, St. Louis, MO). The resuspended sample was homogenized using a Dounce homogenizer with pestle A followed by pestle B. Lysozyme was added to 0.3 mg/ml before cells were twice disrupted by a homogenizer (Avestin, Inc. EmulsiFlex-C3 High Pressure

Homogenizer). CYP27A1 was then extracted from bacterial membrane with 14 mM 3-[(3-cholamidopropyl)dimethyl-ammonio]-1-propane sulfonate (CHAPS) (GoldBio, Saint Louis, MO) for 1 hour at 4 °C. Cell debris and membranes were removed by ultracentrifugation at 12,000 x g for 50 min at 4 °C. The resulting CYP27A1-containing supernatant was loaded on a 30 mL Ni-NTA column (Ni/NTA Superflow, Qiagen, Germantown, MD) equilibrated with 2 column volumes (CV) of loading buffer (100 mM potassium phosphate buffer, pH 7.4, 500 mM NaCl, 20% (v/v) glycerol, 14 mM CHAPS). After loading, the column was first washed isocratically with 5 CV loading buffer, followed by 5 CV Ni-NTA wash buffer (100 mM potassium phosphate buffer, pH 7.4, 500 mM NaCl, 20% (v/v) glycerol, 14 mM CHAPS, 8 mM histidine) to remove weakly bound contaminants. CYP27A1 was then eluted with 6 CV Ni-NTA elution buffer (10 mM potassium phosphate, pH 7.4, 100 mM NaCl, 20% (v/v) glycerol, 10 mM CHAPS, 100 mM histidine). The eluted CYP27A1 fractions typically had a ratio of absorbance at 417 nm/280 nm of 1.0, which were pooled and concentrated to 20-50 mL using an Amicon ultra 50-kDa filter and then diluted 6-fold with CM wash buffer (5 mM potassium phosphate, pH 7.4, 20% (v/v) glycerol, 1 mM ethylenediaminetetraacetic acid (EDTA)) containing 4 mM CHAPS. Two 5 mL HiTrap CM FF column (GE Healthcare) were connected in series for cation-exchange chromatography (total CV=10 mL). Columns were equilibrated with 5 CV CM wash buffer. After loading, these columns were washed with 10 CV CM wash buffer and CYP27A1 subsequently eluted with a gradient from 0 to 500 mM NaCl formed by the CM wash buffer and CM elution buffer (50 mM potassium phosphate, pH 7.4, 500 mM NaCl, 20% (v/v) glycerol, 1 mM EDTA) over 8 CV and a step by CM elution buffer over 2 CV. Fractions with at least equal absorbance at 280 and 417 nm were pooled and concentrated to 1-2 mL using an Amicon ultra 50 kDa filter before injection onto a size exclusion column (GE Healthcare HiLoad® 16/60 Superdex® 200 pg). This column was

equilibrated and run isocratically with CM elution buffer. Fractions with higher absorbance at 417 nm than 280 nm were pooled. The purity of the resulting protein was examined by measuring the ratio of the absorbance of Soret peak at 417 nm vs. the absorbance at 280 nm (typically 1.3) and by SDS-PAGE, which usually showed a single band. Purified CYP27A1 was also characterized using its UV-visible absorbance spectrum and reduced carbon monoxide-difference spectrum.

5.3.2 Ligand binding assay

Ligand binding affinities were determined by observing shifts in the CYP27A1 (in 50 mM potassium phosphate, 20% glycerol) absorbance spectrum as described previously⁵⁴. All ligands (dissolved in DMSO) were titrated into 1 μ M CYP27A1 in a cuvette with 1 cm path length, except for 7 α -hydroxycholest-4-en-3-one (dissolved in ethanol), which was titrated into 0.2 μ M CYP27A1 in a cuvette with 1 cm path length. Changes in absorbance (local absorbance maximum minus minimum) were plotted against ligand concentration and analyzed using the single-site specific binding equation using GraphPad Prism version 9.3.0 for Mac OS X (GraphPad Software, San Diego, CA USA). All titration experiments were done once.

5.3.3 Screening of CYP27A1 Crystallization Conditions

Immediately after CYP27A1 purification and quantitation, CYP27A1 was saturated with a ligand; substrate 7 α -hydroxy-cholest-4-en-3-one and inhibitor clotrimazole were used for crystallization screening. Saturation was confirmed by UV-Vis spectral shift from 417 to 413 nm for the substrate or to 425 nm for the inhibitor. Using the heme Soret peak for quantitation, the protein was concentrated by centrifugation. Sitting-drop 96-well crystallization trays were set using robotic assistance (Gryphon, ARI) and a series of sparse-matrix screening kits for crystallization solutions (Crystal Screen, PEGRx, SaltRx (Hampton), Wizard Classic (Rigaku);

JCSG+, MacroSol, ProPlex, MIDASplus (Molecular Dimensions). Concentrations ranging from 10 to 30 mg/mL were surveyed. Detergent (final concentration of 0.5 and 1 CMC of CHAPS and 0.5 CMC of Cymal-5) and detergent-free conditions were tested. Trays were stored at 25 °C and monitored 24 hours after setting, then intermittently for up to three months. To date, CYP27A1 has not formed crystals.

5.4 Results and discussion

5.4.1 Generation of Recombinant CYP27A1

To generate recombinant CYP27A1, a synthetic cDNA was designed. The N-terminal 25 amino acids were removed and replaced by a sequence coding for MAKKTSS. Additionally, a sequence coding for a 6-residue histidine tag was appended to the C-terminus. The entire gene was codon-optimized and subcloned into the pCWori+ vector for *E. coli* expression. As is typical for membrane P450 enzymes, the resulting CYP27A1 protein was membrane-bound, likely via a typical secondary membrane-binding site. Thus, addition of detergent was used to solubilize CYP27A1. CHAPS was selected for the initial purification as it worked well for CYP8B1 purification. A three-chromatography purification protocol was developed yielding relatively purified protein (Figure 5.1), as indicated by SDS-PAGE (Figure 5.2A). The protein eluted mainly as a tetramer on size exclusion chromatography (Figure 5.1C). The resulting CYP27A1 protein demonstrated a heme Soret peak with a maximum absorbance at 417 nm (Figure 5.2B). This absorbance profile is consistent with water coordination of the heme iron in the active site. When the protein is reduced and exposed to carbon monoxide, the difference spectrum showed absorbance at 450 nm, indicating the Cys-Fe bond is intact (Figure 5.2C). However, after SEC column, there was still a band with higher molecular weight (over 100 KDa) observed on the SDS-PAGE. In order to determine whether this band is a resistant dimer of CYP27A1 or other

proteins, the purified CYP27A1 was mixed with 8 M urea, which is a stronger denaturant, to denature the protein before running on an SDS-PAGE¹⁴³. However, the 8M urea/CYP27A1 sample did not seem to show any effects on the additional protein bands, suggesting that this additional protein band is probably from another contamination protein. Additional approaches such as Western blot using Anti-6X His tag® antibodies could be exploited to further investigate whether the uppermost band is the resistant dimer of CYP27A1.

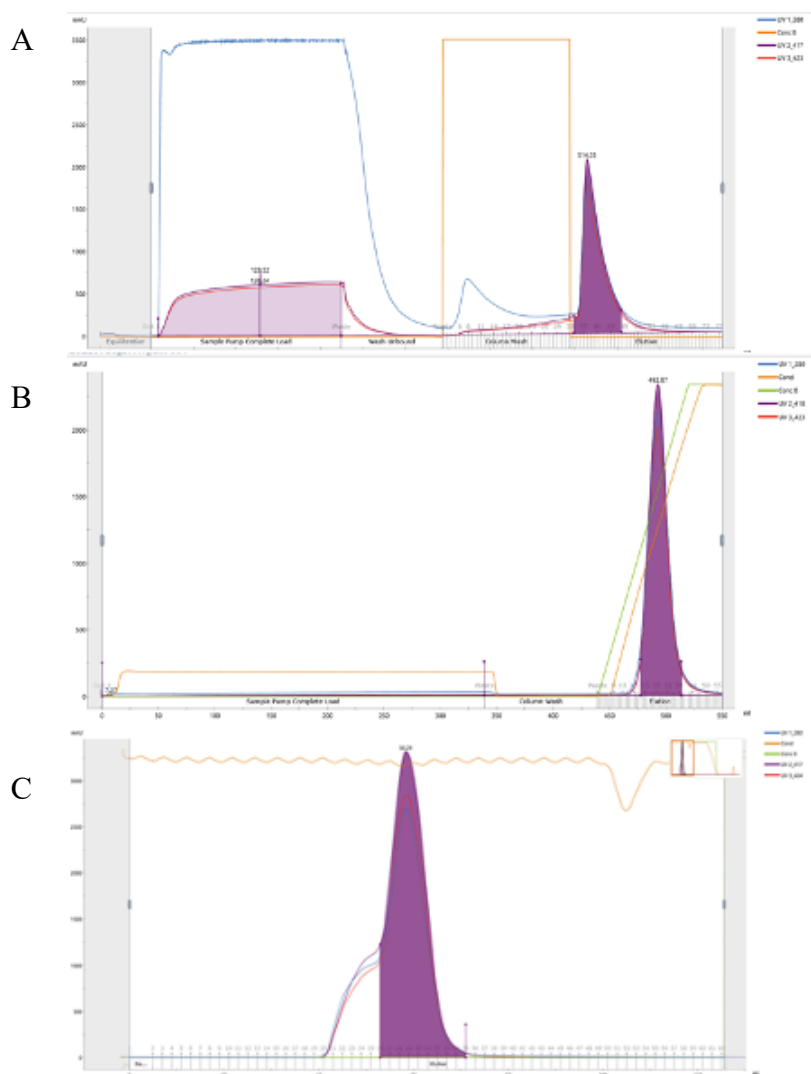


Figure 5.1 Human CYP27A1 purification. CYP27A1 eluted from (A) NiNTA chromatography after a 5 CV 8 mM histidine wash, (B) CM chromatography with a gradient elution, and (C) size exclusion chromatography in tetramers and higher molecular weight oligomers. Pooled fractions in dark purple; absorbance at 417 nm in purple; absorbance at 280 nm in blue.

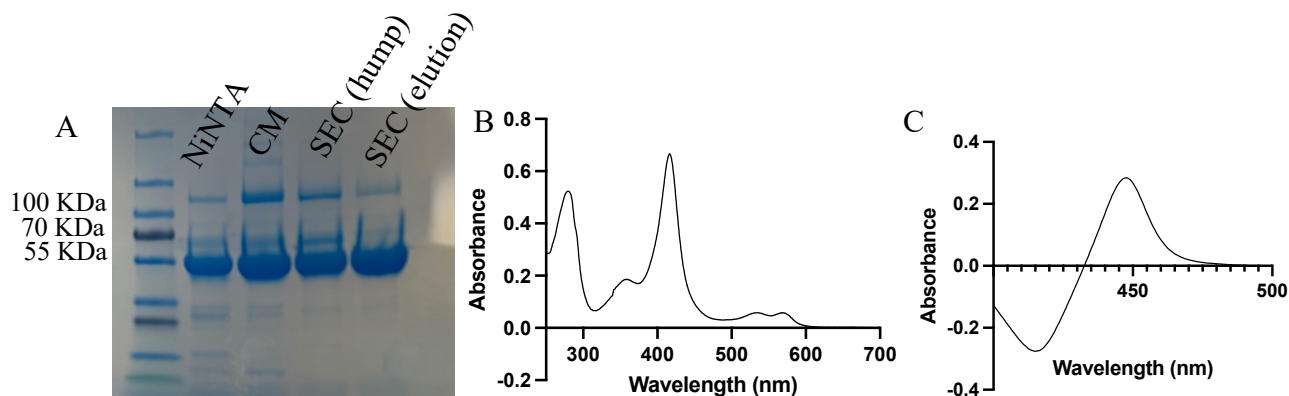


Figure 5.2 Characterization of recombinant, purified CYP27A1. (A) SDS-PAGE with GroEL and upper-most bands, (B) UV-visible absorbance spectrum, indicating heme incorporation with a Soret λ_{max} at 417 nm, (C) reduced carbon monoxide difference spectrum. To enhance the purity

of the protein, several modifications to the purification process could be considered. Firstly, increasing the wash volumes for the NiNTA column may assist in eliminating impurities (Figure 5.1A). Secondly, a more selective approach by only pooling fractions with 417 nm/280 nm and 423 nm/280 nm ratios over 1 could be applied to each step, which would help to isolate only the most desirable protein fractions. Additionally, concentrating the protein to a lower volume before injection onto a size exclusion chromatography column may also enhance resolution. Using an increase SEC column or a larger SEC column could improve the separation between the hump and the elution peak, as depicted in Figure 5.1C. This approach would also be beneficial for removing any remaining GroEL, as SDS-PAGE analysis indicates that a significant amount of GroEL is found within the SEC hump. These suggested changes aim to refine the purification process, reducing impurities and improving the chances of successfully crystallizing the CYP27A1 protein.

5.4.2 CYP27A1 Substrate and Inhibitor Binding

Since tight-binding ligands often help stabilize and crystallize P450 enzymes, facilitating the generation of X-ray structures, ligand binding assays were performed to find such ligands for CYP27A1 co-crystallization. As is typical for cytochrome P450 enzymes, the ability to bind ligands was evaluated by determining shifts of the heme Soret peak from the initial value. A shift

to shorter wavelengths (blue shift) is typically observed when ligands bind in the active site such that they displace a water from the heme iron (type I binding). Conversely, a shift to longer wavelengths (red shift) is typically observed when ligands not only displace this water but have a ligand nitrogen that coordinates the heme iron (type II binding). While the former is often observed for substrates, the latter typically consistent with inhibition since it blocks O₂ binding at this site as required for catalysis.

A variety of substrate and substrate-like ligands were evaluated for their binding affinity to CYP27A1. While titrations of CYP27A1 with its native substrate cholesterol, cholesterol sulfate, 25-hydroxycholesterol, and 4-cholestane-3-one did not yield the expected blue shift in absorbance. However, titrations with 7 α -hydroxycholest-4-en-3-one indicated decreases in absorbance at 420 nm and increasing absorbance at 389 nm, consistent with a type I interaction (Figure 5.3C). Plotting the changes in absorbance vs. ligand concentration revealed that the dissociation constant (K_d) value for this substrate was 136 nM (95% CI: 99.3-185 nM) (Figure 5.3D).

Since specific inhibitors of CYP27A1 have the potential to be valuable clinically but are largely unknown, an initial strategy was to evaluate the ability of CYP27A1 to bind several non-specific P450 inhibitors containing azole groups (econazole, clotrimazole, miconazole, tioconazole, itraconazole, and liarozole), which can often coordinate the heme iron with high affinity. While addition of itraconazole and liarozole did not induce a shift of the CYP27A1 Soret peak and thus may not bind, the other drugs listed above shifted the Soret peak to longer wavelengths (421-423 nm, type II binding) (Figure 5.3A), consistent with an interaction between the CYP27A1 active site heme Fe and the ligand nitrogen. Titrations with each compound were consistent with single site binding with dissociation constants ranging from 0.6-0.7 μ M for miconazole, clotrimazole (Figure 5.3B), and tioconazole, and at 1.8 μ M for econazole (Table 5.1).

It's worth mentioning that miconazole and econazole have almost identical structures. The only difference between these two ligands lies in the number of chlorine substitutions on one of the phenyl ring. However, even this subtle difference results in nearly a three-fold difference in binding affinity. This observation underscores the sensitivity of the CYP27A1 active site and the importance of the positions of the halogen atoms in CYP27A1 ligand recognition.

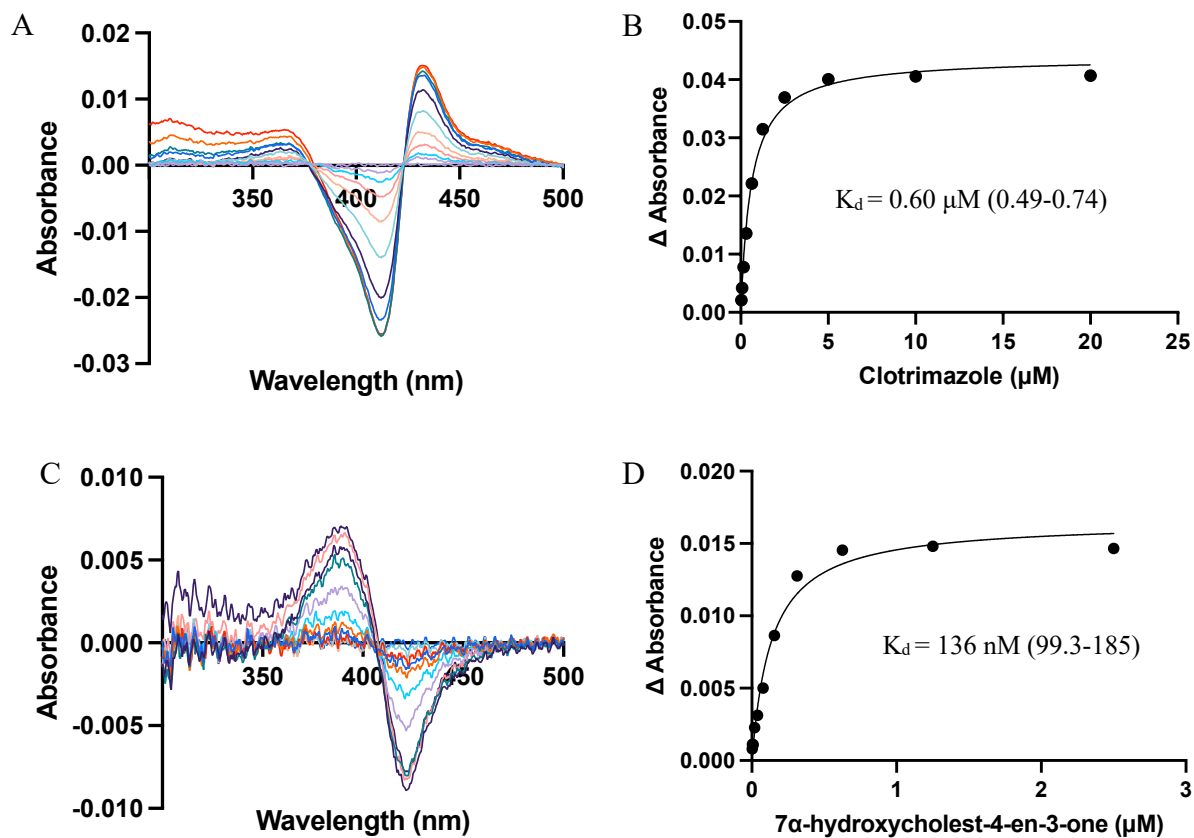


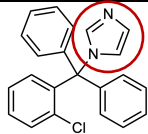
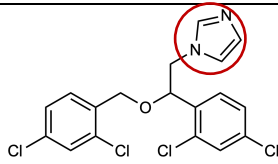
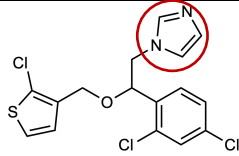
Figure 5.3 CYP27A1 ligand binding. Absorbance changes upon titration of the A) clotrimazole and C) 7α-hydroxycholest-4-en-3-one into CYP27A1 were fit to a single-site binding equation to determine the respective B) and D) dissociation constants (K_d values).

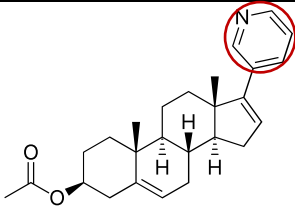
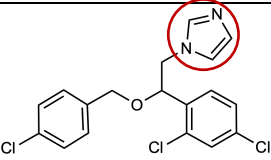
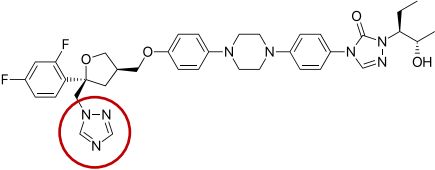
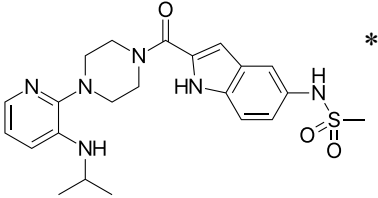
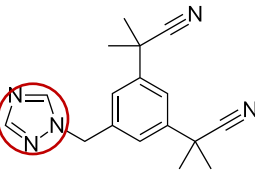
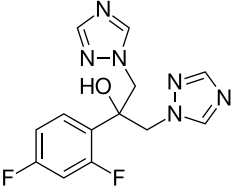
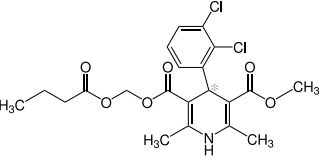
In addition, several commercially available drugs (clevidipine, delavirdine, etravirine, posaconazole, abiraterone, anastrozole, and sorafenib) have been reported with submicromolar K_i for CYP27A1 cholesterol 27-hydroxylation^{142, 141}. Consequently, the binding affinity of these drugs were also evaluated. Posaconazole, abiraterone acetate, anastrozole, and delavirdine induced

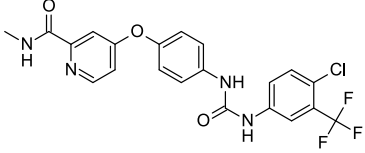
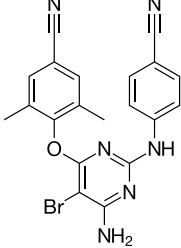
type II shifts of the CYP27A1 Soret peak with binding affinities ranging from 0.95-87 μM (Table 5.1). Titrations of CYP27A1 with clevidipine, sorafenib, and etravirine did not yield a spectral shift, suggesting that these inhibitors may not bind the enzyme through coordinating to the heme iron.

Ligand binding assays conducted on CYP27A1 suggest that this enzyme has a relatively flexible active site. It demonstrated the ability to bind with both small and large molecules, as exemplified by clotrimazole and posaconazole respectively. Additionally, the enzyme's active site showed flexibility in accommodating molecules with either rigid/planar structures like abiraterone or more flexible structures like miconazole. This indicates a broad versatility in the ligand binding capacity of CYP27A1. Moreover, even slight differences in ligand structures resulted in significant differences in binding affinity (econazole and miconazole), suggesting the specificity of the CYP27A1 active site.

Table 5.1 CYP27A1 binding with inhibitors. Groups likely to form Fe-N interactions are circled in red. All titration experiments were done once.

Ligand	Structure	K_d (95% CI) (μM)
Clotrimazole		0.60 (0.49-0.74)
Miconazole		0.70 (0.55-0.88)
Tioconazole		0.72 (0.64-0.82)

Abiraterone acetate		0.95 (0.39-2.2)
Econazole		1.8 (1.5-2.0)
Posaconazole		3.7 (2.4-5.9)
Delavirdine		3.8 (2.9-5.0)
Anastrozole		87 (38-363)
Fluconazole		N.D.
Clevidipine		N.D.

Sorafenib		N.D.
Etravirine		N.D.

N.D. Not determined.

* N-Fe interaction group not known

5.4.3 CYP27A1 crystallization screening

Freshly purified CYP27A1 was saturated with the most tightly-binding ligands, the substrate 7 α -hydroxy-cholest-4-en-3-one and the inhibitor clotrimazole, for co-crystallization in order to improve the stability and homogeneity of the protein. Using robotic assistance (Gryphon, ARI), sitting-drop 96-well crystallization trays were prepared with protein concentrations ranging from 10-30 mg/mL, with or without 9 mM or 18 mM CHAPS or 5 mM Cymal-5. A variety of sparse-matrix screening kits for crystallization solutions were tested. Despite these substantial efforts, CYP27A1 has not been successfully crystallized to date. Most of the drops exhibited heavy precipitation even with the presence of detergents in the protein sample. Additional optimization and screening processes will be necessary to generate CYP27A1 crystals. Potential optimizations could include reducing the protein concentration to 5 mg/mL to decrease precipitation and trying other ligands such as miconazole and tioconazole for co-crystallization. Alternative detergents, such as sodium cholate and Emulgen 913 which have previously been used in CYP27A1 purification^{136, 139}, could also be evaluated for sample preparation. Furthermore, if the purity of the

protein can be improved by optimizing the protein purification process, it may be possible to successfully generate CYP27A1 crystals.

5.5 Conclusion

CYP27A1 is a novel drug target for estrogen ER α - positive breast cancer. The CYP27A1 27-hydroxycholesterol product behaves as a selective estrogen receptor modulator, which is capable of promoting the growth and metastasis of ER-positive tumors. However, currently there is no CYP27A1 selective inhibitor and no CYP27A1 structure to direct such inhibitor design. The CYP27A1 expression, purification, and ligand binding determination herein should significantly advance this effort. The identification of tight-binding CYP27A1 ligands should facilitate the crystallization of this protein, laying the groundwork for future structural and functional investigations of the CYP27A1 active site, enabling design of selective CYP27A1 inhibitors for the treatment of ER-positive breast cancer.

Chapter 6 Conclusion and Future Directions

The aim of the work in this dissertation has been to broaden our understanding of the structure and function of human cytochrome P450 enzymes, specifically CYP3A7, CYP8B1 and CYP27A1. These heme-containing monooxygenases play essential roles in drug metabolism and the pathogenesis of various diseases, making them important targets for potential therapeutic treatments. The comprehensive structural and functional studies conducted have unveiled fundamental insights about these enzymes, establishing a platform for future research and potential therapeutic developments. This will aid in the continued exploration of these enzymes' roles in human health and disease.

The studies presented in Chapters 2 and 3 identified two distinct structures of CYP8B1. These findings serve as a crucial foundation for the development of future CYP8B1 inhibitors and could potentially pave the way for innovative treatments for conditions such as type 2 diabetes and non-alcoholic fatty liver disease. Chapter 2 of this dissertation presents successful expression and purification of the human CYP8B1, along with the first determination of its X-ray structure. The structure was determined in complex with a non-selective inhibitor, tioconazole, which was found to bind in the enzyme's active site, with itsazole nitrogen coordinating with the heme iron, consistent with enzyme inhibition. The research also identified two other azoles, miconazole and econazole, which bind to CYP8B1 with greater affinity than tioconazole and were more effective inhibitors of the enzyme's activity. Comparing the structures of these three azoles provide crucial insights into the design of more effective inhibitors for CYP8B1. Another comparison was

conducted between the active site of CYP8B1 and those of similar P450 enzymes CYP8A1 and CYP7A1, aiming to identify unique features that could be exploited in the design of more selective inhibitors. Furthermore, the research highlighted the role of the Trp281 residue, which appears to play a critical part in the enzyme's binding ability. This claim was substantiated through mutagenesis studies, where the wild type CYP8B1 showed greater binding and catalytic efficiency compared to the W281F mutant CYP8B1, further emphasizing the significance of this residue in the functionality of the enzyme.

The research findings described in chapter 2 provide initial groundwork towards the development of CYP8B1 inhibitors. These inhibitors could improve our understanding of CYP8B1 inhibition in both healthy conditions and disease states. The results may eventually contribute to the creation of new treatments for nonalcoholic fatty liver disease and type 2 diabetes. However, this goal necessitates extensive additional research. With the available CYP8B1 structures, structure-based drug design strategies could be a promising direction for CYP8B1 drug development. Techniques such as ligand-growing or ligand-linking¹⁴⁴ could be utilized for *de novo* structure-based ligand design, a process that involves constructing new molecules informed by the structure of the target enzyme. Additionally, ligand docking could be conducted with CYP8B1 against other structurally similar P450 enzymes to identify more selective CYP8B1 inhibitors. *In vitro* screening offers another promising method for further exploration. By screening all FDA-approved drugs, particularly those belonging to the lipid-lowering and anti-diabetic classes, we can evaluate their binding and inhibitory effect against CYP8B1. This could aid in identifying potential drugs for repurposing, effectively leveraging the safety profiles of existing treatments.

In Chapter 2, a docking model of CYP8B1 with its native substrate, 7 α -hydroxycholest-4-en-3-one, was generated. The docking result illustrated that the long axis of the steroid nucleus was

oriented along with the I helix, with the steroid α face directed towards the I helix (Figure 2.5). To confirm these results, it would be beneficial to solve the X-ray structure of CYP8B1 in complex with 7 α -hydroxycholest-4-en-3-one. The resulting structure would provide vital information about the specific interactions between the enzyme and its substrate. These interactions are integral to the enzyme's functionality and could contribute significantly to our understanding of CYP8B1 in terms of substrate specificity and regioselectivity. Moreover, grasping how CYP8B1 interacts with its natural substrate could inform the design of CYP8B1 inhibitors. Such inhibitors could mimic this interaction, potentially leading to improved drug selectivity.

In Chapter 3, further investigation into selective inhibitors for human CYP8B1 was undertaken. Three steroidal substrate-mimicking compounds, each with a pyridine ring attached at the C12 site of metabolism, were designed, synthesized, and evaluated. These compounds were designed to interact with the enzyme's active site heme iron via the pyridine nitrogen. However, none of them induced shifts in the CYP8B1 Soret absorbance, a spectral characteristic that would indicate such an interaction. When CYP8B1 was co-crystallized with one of these compounds, the ligand was found not bound to the heme iron, but in a channel leading to the active site. Upon further examination of this structure, the significance of Trp281 was further emphasized. This residue, situated directly above the heme, appeared to hinder potential inhibitors from binding. Confirmation of this finding came when a CYP8B1 W281F mutation allowed all three designed compounds to coordinate the heme iron as initially intended. This study concludes that the design of next-generation CYP8B1 inhibitors should take into account the spatial restrictions imposed by the tryptophan residue situated above the heme iron. Optimization of these analogs should focus on minimizing the size of the attached functional group to allow for a better fit in this 'low-ceiling' active site. One potential approach could involve replacing the pyridine ring at the C12 position

of these substrate analogs with an aziridine group, which is directly attached to the C ring of the steroid core at the C11 and C12 positions (Figure 6.1A). Alternatively, the C ring of the steroid core could be replaced with the pyridine group (Figure 6.1B). Such modifications could possibly enhance the interaction between the inhibitor and CYP8B1, potentially improving the effectiveness of the inhibitor. Another possible optimization strategy involves designing a larger ligand with a linker, which could occupy both binding pockets of CYP8B1. This approach could potentially enhance the selectivity of the novel CYP8B1 inhibitors, providing a more specific and effective therapeutic intervention.

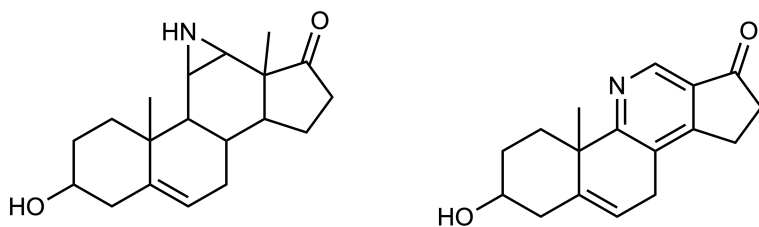


Figure 6.1 Structures of potential next-generation CYP8B1 inhibitors. A) Steroid core with an aziridine attached to the C ring. B) Steroid core with a pyridine replacing the C ring.

The research presented in Chapter 4 unveiled an X-ray structure of a mutated form of CYP3A7, which was saturated with its primary endogenous substrate, dehydroepiandrosterone 3-sulfate (DHEA-S). Surprisingly, this structure indicated that CYP3A7 can bind four copies of DHEA-S simultaneously. Two DHEA-S molecules were found within the active site of the enzyme, one in a ligand access channel, and the fourth on the hydrophobic surface of the protein typically embedded within the membrane. While DHEA-S binding and metabolism did not exhibit cooperative kinetics, this structure is consistent with a previous report suggesting that DHEA-S enhances CYP3A7's metabolism of carbamazepine¹³⁴. Therefore, these findings are a step forward towards understanding the complex interactions between CYP3A7 and its primary substrate,

highlighting multiple binding sites that may simultaneously interact with each other and with other bound substrates.

However, it should be noted that the multiple binding sites were observed in the hexa-mutant CYP3A7. When a homology model of the wild-type CYP3A7 was generated by reverting the six mutations (K421A/K422A/K424A/R69G/C77G/K244E) in the mutant CYP3A7 structure back to the wild type, a clash was observed between Cys77 and DHEA-S3, regardless of the rotamers the Cys77 side chain adopted. This suggests that the wild type enzyme may interact with DHEA-S differently compared to the mutant, potentially impacting the binding locations and substrate interactions. This is consistent with the ligand binding results conducted in Chapter 4, which demonstrated that the hexa-mutant CYP3A7 had ~2-fold higher DHEA-S binding affinity compared to wild type CYP3A7. However, it is also possible that the wild type might undergo a conformational change, opening up the ligand access channel more to accommodate four DHEA-S ligands. Therefore, determining the structure of a wild-type CYP3A7 in complex with DHEA-S would be beneficial. This would help us ascertain whether this multiple ligand binding characteristic is present in the wild-type CYP3A7, thereby improving our understanding of the complex interactions of CYP3A7 with its primary substrate. As noted in Chapter 4, a previous study demonstrated that DHEA-S decreases the K_m of carbamazepine by three-fold¹³⁴, suggesting that both substrates could be present simultaneously in the CYP3A7 active site. It would be intriguing to elucidate a CYP3A7 structure in complex with both DHEA-S and carbamazepine, to investigate if DHEA-S induces a CYP3A7 conformational change or if there is an interaction between DHEA-S and carbamazepine within the active site to enhance carbamazepine metabolism. Such research could further deepen our understanding of CYP3A7's multi-ligand

binding capacity and its role in fetal development and drug metabolism and provide insights into larger context of P450 enzymes heterotropic cooperativity.

Finally, the work presented in Chapter 5 describes the expression, purification, ligand binding, and crystallization screening of CYP27A1. CYP27A1 is involved in the generation of bile acids, and its inhibition represents a validated but unrealized approach to treat diseases such as breast cancer. The absence of a detailed structural information had been a significant hindrance to such inhibitor development. The study of CYP27A1 binding with various substrates and inhibitors in Chapter 4 provided a more comprehensive understanding of the enzyme's function and identified tight-binding ligands for CYP27A1, such as clotrimazole and 27-hydroxycholesterol. Tight-binding ligands usually help crystallize P450 enzymes, and may facilitate the generation of the first CYP27A1 X-ray structure. Despite these initial steps towards determining CYP27A1 structure, additional optimization and screening processes are necessary to generate CYP27A1 crystals. For instance, more ligands could be employed for co-crystallization. Various detergents could be evaluated for sample preparation, and additional screening kits might be utilized for crystallization screening. If obtaining a crystal structure of CYP27A1 proves to be unattainable, an alternative approach would be to create a pharmacophore model of this enzyme. This model would represent the spatial arrangement of ligand features crucial for optimal interaction with CYP27A1, facilitating the discovery of potential CYP27A1 inhibitors.

In conclusion, the work herein has significantly advanced the understanding of the structure and function of three crucial human membrane proteins, offering promising new directions for future work in this field. The two structures of CYP8B1 serve as a foundation for the development of future CYP8B1 inhibitors and could potentially lead to new treatments for type 2 diabetes and non-alcoholic fatty liver disease. Unveiling the structure of CYP3A7 with its native substrate

DHEA-S is a step forward towards understanding how this understudied enzyme contributes to fetal development through the metabolism of DHEA-S. Knowing the chemical topology of the active site in the presence of its main substrate may also help predict its interactions with drugs, toward increasing safe and effective dosing in the fetal and neonatal stages of life. Lastly the CYP27A1 ligand-binding study lays a groundwork in CYP27A1 crystallization and structure determination, facilitating the discovery of potential CYP27A1 inhibitors for the treatment of breast cancer.

Bibliography

- (1) Scott, E. E.; Godamudunage, M. P. Structures of Human Cytochrome P450 Enzymes: Variations on a Theme. In *Dioxygen-dependent Heme Enzymes*, Raven, M. I.-S. a. E. Ed.; Metallobiology, Royal Society of Chemistry, 2018; pp 249 - 273.
- (2) Guengerich, F. P.; Cheng, Q. Orphans in the Human Cytochrome P450 Superfamily: Approaches to Discovering Functions and Relevance in Pharmacology. *Pharmacological reviews* **2011**, *63* (3), 684-699. DOI: 10.1124/pr.110.003525.
- (3) Schenkman, J. B.; Jansson, I. Spectral analyses of cytochromes P450. *Methods Mol Biol* **2006**, *320*, 11-18. DOI: 10.1385/1-59259-998-2:11.
- (4) Omura, T.; Sato, R. The Carbon Monoxide-Binding Pigment of Liver Microsomes. II. Solubilization, Purification, and Properties. *The Journal of biological chemistry* **1964**, *239*, 2379-2385.
- (5) Sun, Y.; Zeng, W.; Benabbas, A.; Ye, X.; Denisov, I.; Sligar, S. G.; Du, J.; Dawson, J. H.; Champion, P. M. Investigations of heme ligation and ligand switching in cytochromes P450 and P420. *Biochemistry* **2013**, *52* (34), 5941-5951, Research Support, N.I.H., Extramural Research Support, U.S. Gov't, Non-P.H.S. DOI: 10.1021/bi400541v.
- (6) Omura, T.; Sato, R. The carbon monoxide-binding pigment of liver microsomes. I. Evidence for its hemoprotein nature. *The Journal of biological chemistry* **1964**, *239*, 2370-2378.
- (7) Manna, S. K.; Mazumdar, S. Reversible inactivation of cytochrome P450 by alkaline earth metal ions: auxiliary metal ion induced conformation change and formation of inactive P420 species in CYP101. *J Inorg Biochem* **2008**, *102* (5-6), 1312-1321. DOI: 10.1016/j.jinorgbio.2008.01.013 From NLM.
- (8) Munro, A.; Girvan, H.; McLean, K. Variations on a (T)heme — Novel Mechanisms, Redox Partners and Catalytic Functions in the Cytochrome P450 Superfamily. *Natural product reports* **2007**, *24*, 585-609. DOI: 10.1039/b604190f.
- (9) Liu, Y.; Denisov, I. G.; Sligar, S. G.; Kincaid, J. R. Substrate-Specific Allosteric Effects on the Enhancement of CYP17A1 Lyase Efficiency by Cytochrome b5. *Journal of the American Chemical Society* **2021**, *143* (10), 3729-3733. DOI: 10.1021/jacs.1c00581.
- (10) Petrunak, E. M.; DeVore, N. M.; Porubsky, P. R.; Scott, E. E. Structures of human steroidogenic cytochrome P450 17A1 with substrates. *The Journal of biological chemistry* **2014**, *289* (47), 32952-32964. DOI: 10.1074/jbc.M114.610998. Petrunak, E. M.; Rogers, S. A.; Aube, J.; Scott, E. E. Structural and Functional Evaluation of Clinically Relevant Inhibitors of Steroidogenic Cytochrome P450 17A1. *Drug metabolism and disposition: the biological fate of chemicals* **2017**, *45* (6), 635-645. DOI: 10.1124/dmd.117.075317 From NLM Medline.
- (11) DeVore, N. M.; Scott, E. E. Structures of cytochrome P450 17A1 with prostate cancer drugs abiraterone and TOK-001. *Nature* **2012**, *482* (7383), 116-119, Research Support, N.I.H., Extramural. DOI: 10.1038/nature10743.

- (12) Calkin, A. C.; Tontonoz, P. Transcriptional integration of metabolism by the nuclear sterol-activated receptors LXR and FXR. *Nat Rev Mol Cell Biol* **2012**, *13* (4), 213-224. DOI: 10.1038/nrm3312 From NLM.
- (13) Kim, I.; Ahn, S. H.; Inagaki, T.; Choi, M.; Ito, S.; Guo, G. L.; Kliewer, S. A.; Gonzalez, F. J. Differential regulation of bile acid homeostasis by the farnesoid X receptor in liver and intestine. *Journal of lipid research* **2007**, *48* (12), 2664-2672. DOI: 10.1194/jlr.M700330-JLR200 From NLM.
- (14) Zhang, M.; Chiang, J. Y. Transcriptional regulation of the human sterol 12 α -hydroxylase gene (CYP8B1): roles of hepatocyte nuclear factor 4 α in mediating bile acid repression. *The Journal of biological chemistry* **2001**, *276* (45), 41690-41699. DOI: 10.1074/jbc.M105117200.
- (15) Jahan, A.; Chiang, J. Y. Cytokine regulation of human sterol 12 α -hydroxylase (CYP8B1) gene. *Am J Physiol Gastrointest Liver Physiol* **2005**, *288* (4), G685-695. DOI: 10.1152/ajpgi.00207.2004 From NLM.
- (16) Chevre, R.; Trigueros-Motos, L.; Castano, D.; Chua, T.; Corliano, M.; Patankar, J. V.; Sng, L.; Sim, L.; Juin, T. L.; Carissimo, G.; et al. Therapeutic modulation of the bile acid pool by Cyp8b1 knockdown protects against nonalcoholic fatty liver disease in mice. *Faseb J* **2018**, *32* (7), 3792-3802. DOI: 10.1096/fj.201701084RR.
- (17) Chung, E.; Offei, S. D.; Aondo Jia, U. T.; Estevez, J.; Perez, Y.; Arman, H. D.; Yoshimoto, F. K. A synthesis of a rationally designed inhibitor of cytochrome P450 8B1, a therapeutic target to treat obesity. *Steroids* **2022**, *178*, 108952. DOI: 10.1016/j.steroids.2021.108952 From NLM Medline.
- (18) Haeusler, R. A.; Astiarraga, B.; Camastra, S.; Accili, D.; Ferrannini, E. Human insulin resistance is associated with increased plasma levels of 12 α -hydroxylated bile acids. *Diabetes* **2013**, *62* (12), 4184-4191. DOI: 10.2337/db13-0639 From NLM.
- (19) Mazzolini, G.; Sowa, J. P.; Atorrasagasti, C.; Kucukoglu, Ö.; Syn, W. K.; Canbay, A. Significance of Simple Steatosis: An Update on the Clinical and Molecular Evidence. *Cells* **2020**, *9* (11). DOI: 10.3390/cells9112458 From NLM.
- (20) Powell, E. E.; Wong, V. W.-S.; Rinella, M. Non-alcoholic fatty liver disease. *The Lancet* **2021**, *397* (10290), 2212-2224. DOI: [https://doi.org/10.1016/S0140-6736\(20\)32511-3](https://doi.org/10.1016/S0140-6736(20)32511-3).
- (21) Sharma, B.; John, S. Hepatic Cirrhosis. In *StatPearls*, StatPearls Publishing Copyright © 2023, StatPearls Publishing LLC., 2023.
- (22) Hartke, J.; Johnson, M.; Ghabril, M. The diagnosis and treatment of hepatocellular carcinoma. *Semin Diagn Pathol* **2017**, *34* (2), 153-159. DOI: 10.1053/j.semmp.2016.12.011 From NLM.
- (23) Laube, R.; Sabih, A. H.; Strasser, S. I.; Lim, L.; Cigolini, M.; Liu, K. Palliative care in hepatocellular carcinoma. *J Gastroenterol Hepatol* **2021**, *36* (3), 618-628. DOI: 10.1111/jgh.15169 From NLM.
- (24) Jiao, N.; Baker, S. S.; Chapa-Rodriguez, A.; Liu, W.; Nugent, C. A.; Tsompana, M.; Mastrandrea, L.; Buck, M. J.; Baker, R. D.; Genco, R. J.; et al. Suppressed hepatic bile acid signalling despite elevated production of primary and secondary bile acids in NAFLD. *Gut* **2018**, *67* (10), 1881-1891. DOI: 10.1136/gutjnl-2017-314307 From NLM.
- (25) Lascar, N.; Brown, J.; Pattison, H.; Barnett, A. H.; Bailey, C. J.; Bellary, S. Type 2 diabetes in adolescents and young adults. *Lancet Diabetes Endocrinol* **2018**, *6* (1), 69-80. DOI: 10.1016/s2213-8587(17)30186-9 From NLM.

- (26) Wu, Y.; Ding, Y.; Tanaka, Y.; Zhang, W. Risk factors contributing to type 2 diabetes and recent advances in the treatment and prevention. *Int J Med Sci* **2014**, *11* (11), 1185-1200. DOI: 10.7150/ijms.10001 From NLM.
- (27) Fiorucci, S.; Distrutti, E.; Carino, A.; Zampella, A.; Biagioli, M. Bile acids and their receptors in metabolic disorders. *Prog Lipid Res* **2021**, *82*, 101094. DOI: 10.1016/j.plipres.2021.101094.
- (28) Jiao, Y.; Lu, Y.; Li, X. Y. Farnesoid X receptor: a master regulator of hepatic triglyceride and glucose homeostasis. *Acta Pharmacol Sin* **2015**, *36* (1), 44-50. DOI: 10.1038/aps.2014.116 From NLM.
- (29) Thomas, C.; Gioiello, A.; Noriega, L.; Strehle, A.; Oury, J.; Rizzo, G.; Macchiarulo, A.; Yamamoto, H.; Matak, C.; Pruzanski, M.; et al. TGR5-mediated bile acid sensing controls glucose homeostasis. *Cell Metab* **2009**, *10* (3), 167-177. DOI: 10.1016/j.cmet.2009.08.001 From NLM.
- (30) Kaur, A.; Patankar, J. V.; de Haan, W.; Ruddle, P.; Wijesekara, N.; Groen, A. K.; Verchere, C. B.; Singaraja, R. R.; Hayden, M. R. Loss of *Cyp8b1* Improves Glucose Homeostasis by Increasing GLP-1. *Diabetes* **2014**, *64*, 1168-1179.
- (31) DeBarber, A. E.; Duell, P. B. Update on cerebrotendinous xanthomatosis. *Curr Opin Lipidol* **2021**, *32* (2), 123-131. DOI: 10.1097/mol.0000000000000740 From NLM.
- (32) Nie, S.; Chen, G.; Cao, X.; Zhang, Y. Cerebrotendinous xanthomatosis: a comprehensive review of pathogenesis, clinical manifestations, diagnosis, and management. *Orphanet J Rare Dis* **2014**, *9*, 179. DOI: 10.1186/s13023-014-0179-4 From NLM.
- (33) Nagini, S. Breast Cancer: Current Molecular Therapeutic Targets and New Players. *Anticancer Agents Med Chem* **2017**, *17* (2), 152-163. DOI: 10.2174/1871520616666160502122724 From NLM.
- (34) Kimbung, S.; Stalhammar, T.; Inasu, M.; Nodin, B.; Elebro, K.; Tryggvadottir, H.; Jirstrom, K.; Rose, C.; Ingvar, C.; Jernstrom, H.; et al. High expression of CYP27A1 in breast cancer is associated with poor tumor pathological features and may differentially predict prognosis depending on menopausal status. *Cancer research* **2019**, *79* (4). DOI: 10.1158/1538-7445.Sabcs18-P2-08-26.
- (35) Kimbung, S.; Chang, C. Y.; Bendahl, P. O.; Dubois, L.; Thompson, J. W.; McDonnell, D. P.; Borgquist, S. Impact of 27-hydroxylase (CYP27A1) and 27-hydroxycholesterol in breast cancer. *Endocr-Relat Cancer* **2017**, *24* (7), 339-349. DOI: 10.1530/Erc-16-0533.
- (36) Baek, A. E.; Yu, Y. R. A.; He, S. S.; Wardell, S. E.; Chang, C. Y.; Kwon, S.; Pillai, R. V.; McDowell, H. B.; Thompson, J. W.; Dubois, L. G.; et al. The cholesterol metabolite 27 hydroxycholesterol facilitates breast cancer metastasis through its actions on immune cells. *Nature Communications* **2017**, *8*. DOI: ARTN 864 10.1038/s41467-017-00910-z.
- (37) Flockhart DA, T., D., McDonald, C., Desta, Z. . The Flockhart Cytochrome P450 Drug-Drug Interaction Table. <https://medicine.iu.edu/internal-medicine/specialties/clinical-pharmacology/drug-interaction-flockhart-table>.
- (38) Stevens, J. C.; Hines, R. N.; Gu, C.; Koukouritaki, S. B.; Manro, J. R.; Tandler, P. J.; Zaya, M. J. Developmental expression of the major human hepatic CYP3A enzymes. *The Journal of pharmacology and experimental therapeutics* **2003**, *307* (2), 573-582. DOI: 10.1124/jpet.103.054841.
- (39) Leeder, J. S.; Gaedigk, R.; Marcucci, K. A.; Gaedigk, A.; Vyhlidal, C. A.; Schindel, B. P.; Pearce, R. E. Variability of CYP3A7 expression in human fetal liver. *The Journal of*

- pharmacology and experimental therapeutics* **2005**, 314 (2), 626-635. DOI: 10.1124/jpet.105.086504.
- (40) LORIAUX, D. L.; RUDER, H. J.; KNAB, D. R.; LIPSETT, M. B. Estrone Sulfate, Estrone, Estradiol and Estriol Plasma Levels in Human Pregnancy. *The Journal of Clinical Endocrinology & Metabolism* **1972**, 35 (6), 887-891. DOI: 10.1210/jcem-35-6-887 (accessed 5/7/2023).
- (41) Kaludjerovic, J.; Ward, W. E. The Interplay between Estrogen and Fetal Adrenal Cortex. *J Nutr Metab* **2012**, 2012, 837901. DOI: 10.1155/2012/837901 From NLM.
- (42) Pasqualini, J. R. Enzymes involved in the formation and transformation of steroid hormones in the fetal and placental compartments. *J Steroid Biochem Mol Biol* **2005**, 97 (5), 401-415. DOI: 10.1016/j.jsbmb.2005.08.004 From NLM Medline.
- (43) Bashore, R. A.; Westlake, J. R. Plasma unconjugated estriol values in high-risk pregnancy. *Am J Obstet Gynecol* **1977**, 128 (4), 371-380. DOI: 10.1016/0002-9378(77)90555-5 From NLM Medline.
- (44) Fejgin, M.; Amiel, A.; Goldberger, S.; Barnes, I.; Zer, T.; Kohn, G. Placental insufficiency as a possible cause of low maternal serum human chorionic gonadotropin and low maternal serum unconjugated estriol levels in triploidy. *Am J Obstet Gynecol* **1992**, 167 (3), 766-767. DOI: 10.1016/s0002-9378(11)91586-5 From NLM.
- (45) Palo, P.; Erkkola, R.; Irjala, K.; Taina, E. Serum free estriol inefficient in the detection of intrauterine growth retardation. *Ann Chir Gynaecol Suppl* **1987**, 202, 20-22. From NLM.
- (46) Quinney, S. K.; Benjamin, T.; Zheng, X.; Patil, A. S. Characterization of Maternal and Fetal CYP3A-Mediated Progesterone Metabolism. *Fetal Pediatr Pathol* **2017**, 36 (5), 400-411. DOI: 10.1080/15513815.2017.1354411 From NLM.
- (47) Kandel, S. E.; Han, L. W.; Mao, Q.; Lampe, J. N. Digging Deeper into CYP3A Testosterone Metabolism: Kinetic, Regioselectivity, and Stereoselectivity Differences between CYP3A4/5 and CYP3A7. *Drug metabolism and disposition: the biological fate of chemicals* **2017**, 45 (12), 1266-1275. DOI: 10.1124/dmd.117.078055 From NLM.
- (48) Topletz, A. R.; Zhong, G.; Isoherranen, N. Scaling in vitro activity of CYP3A7 suggests human fetal livers do not clear retinoic acid entering from maternal circulation. *Scientific reports* **2019**, 9 (1), 4620. DOI: 10.1038/s41598-019-40995-8 From NLM.
- (49) Williams, J. A.; Ring, B. J.; Cantrell, V. E.; Jones, D. R.; Eckstein, J.; Ruterbories, K.; Hamman, M. A.; Hall, S. D.; Wrighton, S. A. Comparative metabolic capabilities of CYP3A4, CYP3A5, and CYP3A7. *Drug metabolism and disposition: the biological fate of chemicals* **2002**, 30 (8), 883-891.
- (50) Hashimoto, H.; Nakagawa, T.; Yokoi, T.; Sawada, M.; Itoh, S.; Kamataki, T. Fetus-specific CYP3A7 and adult-specific CYP3A4 expressed in Chinese hamster CHL cells have similar capacity to activate carcinogenic mycotoxins. *Cancer research* **1995**, 55 (4), 787-791. From NLM.
- (51) Gillam, E. M.; Wunsch, R. M.; Ueng, Y. F.; Shimada, T.; Reilly, P. E.; Kamataki, T.; Guengerich, F. P. Expression of cytochrome P450 3A7 in Escherichia coli: effects of 5' modification and catalytic characterization of recombinant enzyme expressed in bicistronic format with NADPH-cytochrome P450 reductase. *Archives of biochemistry and biophysics* **1997**, 346 (1), 81-90. DOI: 10.1006/abbi.1997.0286 From NLM.
- (52) Kandel, S. E.; Lampe, J. N. Inhibition of CYP3A7 DHEA-S Oxidation by Lopinavir and Ritonavir: An Alternative Mechanism for Adrenal Impairment in HIV Antiretroviral-Treated

- Neonates. *Chemical research in toxicology* **2021**, *34* (4), 1150-1160. DOI: 10.1021/acs.chemrestox.1c00028 From NLM Medline.
- (53) Granfors, M. T.; Wang, J. S.; Kajosaari, L. I.; Laitila, J.; Neuvonen, P. J.; Backman, J. T. Differential inhibition of cytochrome P450 3A4, 3A5 and 3A7 by five human immunodeficiency virus (HIV) protease inhibitors in vitro. *Basic Clin Pharmacol Toxicol* **2006**, *98* (1), 79-85. DOI: 10.1111/j.1742-7843.2006.pto_249.x.
- (54) Godamudunage, M. P.; Grech, A. M.; Scott, E. E. Comparison of Antifungal Azole Interactions with Adult Cytochrome P450 3A4 versus Neonatal Cytochrome P450 3A7. *Drug metabolism and disposition: the biological fate of chemicals* **2018**, *46* (9), 1329-1337. DOI: 10.1124/dmd.118.082032.
- (55) Staels, B.; Fonseca, V. A. Bile acids and metabolic regulation: mechanisms and clinical responses to bile acid sequestration. *Diabetes Care* **2009**, *32 Suppl 2*, S237-245. DOI: 10.2337/dc09-S355.
- (56) Chiang, J. Y. Recent advances in understanding bile acid homeostasis. *F1000Res* **2017**, *6*, 2029-2029. DOI: 10.12688/f1000research.12449.1 PubMed.
- (57) Manne, V.; Handa, P.; Kowdley, K. V. Pathophysiology of Nonalcoholic Fatty Liver Disease/Nonalcoholic Steatohepatitis. *Clin Liver Dis* **2018**, *22* (1), 23-37. DOI: 10.1016/j.cld.2017.08.007 From NLM.
- (58) Puri, P.; Daita, K.; Joyce, A.; Mirshahi, F.; Santhekadur, P. K.; Cazanave, S.; Luketic, V. A.; Siddiqui, M. S.; Boyett, S.; Min, H. K.; et al. The presence and severity of nonalcoholic steatohepatitis is associated with specific changes in circulating bile acids. *Hepatology* **2018**, *67* (2), 534-548. DOI: 10.1002/hep.29359 From NLM.
- (59) Han, C. Y. Update on FXR Biology: Promising Therapeutic Target? *Int J Mol Sci* **2018**, *19* (7). DOI: 10.3390/ijms19072069 From NLM.
- (60) Hindson, J. Obeticholic acid for the treatment of NASH. *Nature Reviews Gastroenterology & Hepatology* **2020**, *17* (2), 66-66. DOI: 10.1038/s41575-020-0264-1.
- (61) Arab, J. P.; Karpen, S. J.; Dawson, P. A.; Arrese, M.; Trauner, M. Bile acids and nonalcoholic fatty liver disease: Molecular insights and therapeutic perspectives. *Hepatology* **2017**, *65* (1), 350-362. DOI: 10.1002/hep.28709 From NLM.
- (62) Chevre, R.; Trigueros-Motos, L.; Castano, D.; Chua, T.; Corliano, M.; Patankar, J. V.; Sng, L.; Sim, L.; Juin, T. L.; Carissimo, G.; et al. Therapeutic modulation of the bile acid pool by Cyp8b1 knockdown protects against nonalcoholic fatty liver disease in mice. *Faseb J* **2018**, *32* (7), 3792-3802. DOI: 10.1096/fj.201701084RR.
- (63) Pathak, P.; Chiang, J. Y. L. Sterol 12 α -Hydroxylase Aggravates Dyslipidemia by Activating the Ceramide/mTORC1/SREBP-1C Pathway via FGF21 and FGF15. *Gene Expr* **2019**, *19* (3), 161-173. DOI: 10.3727/105221619x15529371970455 From NLM.
- (64) Kaur, A.; Patankar, J. V.; de Haan, W.; Ruddle, P.; Wijesekara, N.; Groen, A. K.; Verchere, C. B.; Singaraja, R. R.; Hayden, M. R. Loss of *Cyp8b1* Improves Glucose Homeostasis by Increasing GLP-1. *Diabetes* **2015**, *64* (4), 1168-1179. DOI: 10.2337/db14-0716.
- (65) Ishida, H.; Noshiro, M.; Okuda, K.; Coon, M. J. Purification and characterization of 7 α -hydroxy-4-cholesten-3-one 12 α -hydroxylase. *Journal of Biological Chemistry* **1992**, *267* (30), 21319-21323. DOI: [https://doi.org/10.1016/S0021-9258\(19\)36611-6](https://doi.org/10.1016/S0021-9258(19)36611-6).
- (66) Eggertsen, G.; Olin, M.; Andersson, U.; Ishida, H.; Kubota, S.; Hellman, U.; Okuda, K. I.; Björkhem, I. Molecular cloning and expression of rabbit sterol 12 α -hydroxylase. *The Journal of biological chemistry* **1996**, *271* (50), 32269-32275. DOI: 10.1074/jbc.271.50.32269 From NLM.

- (67) Fan, L.; Joseph, J. F.; Durairaj, P.; Parr, M. K.; Bureik, M. Conversion of chenodeoxycholic acid to cholic acid by human CYP8B1. *Biological Chemistry* **2019**, *400* (5), 625-628. DOI: doi:10.1515/hsz-2018-0379.
- (68) Bart, A. G.; Scott, E. E. Structural and functional effects of cytochrome *b₅* interactions with human cytochrome P450 enzymes. *The Journal of biological chemistry* **2017**, *292* (51), 20818-20833. DOI: 10.1074/jbc.RA117.000220.
- (69) Otwinowski, Z.; Minor, W. Processing of X-ray diffraction data collected in oscillation mode. *Methods Enzymol* **1997**, *276*, 307-326.
- (70) McCoy, A. J.; Grosse-Kunstleve, R. W.; Adams, P. D.; Winn, M. D.; Storoni, L. C.; Read, R. J. Phaser crystallographic software. *Journal of applied crystallography* **2007**, *40* (Pt 4), 658-674. DOI: 10.1107/S0021889807021206.
- (71) Emsley, P.; Lohkamp, B.; Scott, W. G.; Cowtan, K. Features and development of Coot. *Acta Crystallogr. D* **2010**, *66* (Pt 4), 486-501. DOI: 10.1107/S0907444910007493.
- (72) Adams, P. D.; Afonine, P. V.; Bunkoczi, G.; Chen, V. B.; Davis, I. W.; Echols, N.; Headd, J. J.; Hung, L. W.; Kapral, G. J.; Grosse-Kunstleve, R. W.; et al. PHENIX: a comprehensive Python-based system for macromolecular structure solution. *Acta Crystallogr. D* **2010**, *66* (Pt 2), 213-221. DOI: 10.1107/S0907444909052925.
- (73) Moriarty, N. W.; Grosse-Kunstleve, R. W.; Adams, P. D. electronic Ligand Builder and Optimization Workbench (eLBOW): a tool for ligand coordinate and restraint generation. *Acta Crystallogr. D* **2009**, *65* (Pt 10), 1074-1080. DOI: 10.1107/S0907444909029436.
- (74) Kleywegt, G. J.; Jones, T. A. Detection, delineation, measurement and display of cavities in macromolecular structures. *Acta Crystallogr. D* **1994**, *50*, 178-185. DOI: Doi 10.1107/S0907444993011333.
- (75) Mura, C.; McCrimmon, C. M.; Vertrees, J.; Sawaya, M. R. An introduction to biomolecular graphics. *PLoS Comput Biol* **2010**, *6* (8). DOI: 10.1371/journal.pcbi.1000918 From NLM.
- (76) Lu, C.; Wu, C.; Ghoreishi, D.; Chen, W.; Wang, L.; Damm, W.; Ross, G. A.; Dahlgren, M. K.; Russell, E.; Von Bargen, C. D.; et al. OPLS4: Improving Force Field Accuracy on Challenging Regimes of Chemical Space. *Journal of Chemical Theory and Computation* **2021**, *17* (7), 4291-4300. DOI: 10.1021/acs.jctc.1c00302.
- (77) Sherman, W.; Day, T.; Jacobson, M. P.; Friesner, R. A.; Farid, R. Novel procedure for modeling ligand/receptor induced fit effects. *Journal of medicinal chemistry* **2006**, *49* (2), 534-553. DOI: 10.1021/jm050540c From NLM.
- (78) Friesner, R. A.; Murphy, R. B.; Repasky, M. P.; Frye, L. L.; Greenwood, J. R.; Halgren, T. A.; Sanschagrin, P. C.; Mainz, D. T. Extra Precision Glide: Docking and Scoring Incorporating a Model of Hydrophobic Enclosure for Protein-Ligand Complexes. *Journal of medicinal chemistry* **2006**, *49* (21), 6177-6196. DOI: 10.1021/jm051256o.
- (79) Gotoh, O. Substrate recognition sites in cytochrome P450 family 2 (CYP2) proteins inferred from comparative analyses of amino acid and coding nucleotide sequences. *The Journal of biological chemistry* **1992**, *267* (1), 83-90.
- (80) Mast, N.; Graham, S. E.; Andersson, U.; Bjorkhem, I.; Hill, C.; Peterson, J.; Pikuleva, I. A. Cholesterol binding to cytochrome P450 7A1, a key enzyme in bile acid biosynthesis. *Biochemistry* **2005**, *44* (9), 3259-3271. DOI: 10.1021/bi047566a.
- (81) McLean, K. J.; Warman, A. J.; Seward, H. E.; Marshall, K. R.; Girvan, H. M.; Cheesman, M. R.; Waterman, M. R.; Munro, A. W. Biophysical Characterization of the Sterol Demethylase P450 from Mycobacterium tuberculosis, Its Cognate Ferredoxin, and Their Interactions. *Biochemistry* **2006**, *45* (27), 8427-8443. DOI: 10.1021/bi0601609.

- (82) Muralidhara, B. K.; Negi, S.; Chin, C. C.; Braun, W.; Halpert, J. R. Conformational flexibility of mammalian cytochrome P450 2B4 in binding imidazole inhibitors with different ring chemistry and side chains. Solution thermodynamics and molecular modeling. *The Journal of biological chemistry* **2006**, *281* (12), 8051-8061, Research Support, N.I.H., Extramural Research Support, U.S. Gov't, Non-P.H.S. DOI: 10.1074/jbc.M509696200.
- (83) Tempel, W.; Grabovec, I.; MacKenzie, F.; Dichenko, Y. V.; Usanov, S. A.; Gilep, A. A.; Park, H. W.; Strushkevich, N. Structural characterization of human cholesterol 7 α -hydroxylase. *Journal of lipid research* **2014**, *55* (9), 1925-1932. DOI: 10.1194/jlr.M050765.
- (84) Ullrich, V.; Brugger, R. Prostacyclin and Thromboxane Synthase: New Aspects of Hemethiolate Catalysis. *Angewandte Chemie International Edition in English* **1994**, *33* (19), 1911-1919. DOI: <https://doi.org/10.1002/anie.199419111>.
- (85) Goizet, C.; Boukhris, A.; Durr, A.; Beetz, C.; Truchetto, J.; Tesson, C.; Tsaousidou, M.; Forlani, S.; Guyant-Maréchal, L.; Fontaine, B.; et al. CYP7B1 mutations in pure and complex forms of hereditary spastic paraplegia type 5. *Brain* **2009**, *132* (Pt 6), 1589-1600. DOI: 10.1093/brain/awp073 From NLM.
- (86) Li, Y. C.; Chiang, C. W.; Yeh, H. C.; Hsu, P. Y.; Whitby, F. G.; Wang, L. H.; Chan, N. L. Structures of prostacyclin synthase and its complexes with substrate analog and inhibitor reveal a ligand-specific heme conformation change. *The Journal of biological chemistry* **2008**, *283* (5), 2917-2926. DOI: 10.1074/jbc.M707470200.
- (87) Tuder, R. M.; Cool, C. D.; Geraci, M. W.; Wang, J.; Abman, S. H.; Wright, L.; Badesch, D.; Voelkel, N. F. Prostacyclin synthase expression is decreased in lungs from patients with severe pulmonary hypertension. *Am J Respir Crit Care Med* **1999**, *159* (6), 1925-1932. DOI: 10.1164/ajrcm.159.6.9804054 From NLM.
- (88) Pullinger, C. R.; Eng, C.; Salen, G.; Shefer, S.; Batta, A. K.; Erickson, S. K.; Verhagen, A.; Rivera, C. R.; Mulvihill, S. J.; Malloy, M. J.; et al. Human cholesterol 7 α -hydroxylase (CYP7A1) deficiency has a hypercholesterolemic phenotype. *J Clin Invest* **2002**, *110* (1), 109-117. DOI: 10.1172/jci15387 From NLM.
- (89) Murakami, K.; Okada, Y.; Okuda, K. Purification and characterization of 7 α -hydroxy-4-cholesten-3-one 12 α -monooxygenase. *J. Biol. Chem.* **1982**, *257*, 8030-8035. Ishida, H.; Noshiro, M.; Okuda, K.; Coon, M. J. Purification and characterization of 7 α -hydroxy-4-cholesten-3-one 12 α -hydroxylase. *J. Biol. Chem.* **1992**, *267*, 21319-21323.
- (90) Wang, D. Q.-H.; Lammert, F.; Cohen, D. E.; Paigen, B.; Carey, M. C. American Journal of Physiology. *Cholic acid aids absorption, biliary secretion, and phase transitions of cholesterol in murine cholelithogenesis* **1999**, *276*, G751-G760. Woollett, L. A.; Buckley, D. D.; Yao, L.; Jones, P. J. H.; Granholm, N. A.; Tolley, E. A.; Tso, P.; Heubi, H. E. Cholic acid supplementation enhances cholesterol absorption in humans. *Gastroenterology* **2004**, *126*, 724-731. Reynier, M. O.; Montet, J. C.; Gerolami, A.; Marteau, C.; Crotte, C.; Montet, A. M.; Mathieu, S. Comparative effects of cholic, chenodeoxycholic, and ursodeoxycholic acids on micellar solubilization and intestinal absorption of cholesterol. *J. Lipid Res.* **1981**, *22*, 467-473.
- (91) Bertaggia, E.; Jensen, K. K.; Castro-Perez, J.; Xu, Y.; Di Paolo, G.; Chan, R. B.; Wang, L.; Haeusler, R. A. *Cyp8b1* ablation prevents Western diet-induced weight gain and hepatic steatosis because of impaired fat absorption. *Am. J. Physiol. Endocrinol. Metab.* **2017**, *313*, E121-E133.
- (92) Chevre, R.; Trigueros-Motos, L.; Castano, D.; Chua, T.; Corliano, M.; Patankar, J. V.; Sng, L.; Sim, L.; Juin, T. L.; Carissimo, G.; et al. Therapeutic modulation of the bile acid pool by *Cyp8b1* knockdown protects against nonalcoholic fatty liver disease in mice *FASEB J.* **2018**, *32*, 3792-3802.

- (93) Liu, J.; Carlson, H. A.; Scott, E. E. The structure and characterization of human cytochrome P450 8B1 supports future drug design for nonalcoholic fatty liver disease and diabetes. *The Journal of biological chemistry* **2022**, *298* (9), 102344. DOI: 10.1016/j.jbc.2022.102344 From NLM Medline.
- (94) Barrie, S. E.; Potter, G. A.; Goddard, P. M.; Haynes, B. P.; Dowsett, M.; Jarman, M. Pharmacology of novel steroidal inhibitors of cytochrome P45017 α (17 α -hydroxylase/C17–20 lyase). *J. Ster. Biochem. Mol. Biol.* **1994**, *50*, 267-273.
- (95) Kabsch, W. XDS. *Acta Crystallogr. D* **2010**, *66* (Pt 2), 125-132. DOI: 10.1107/S0907444909047337.
- (96) Chung, E.; Offei, S. D.; Jia, U.-T. A.; Estevez, J.; Perez, Y.; Arman, H. D.; Yoshimoto, F. K. A synthesis of a rationally designed inhibitor of cytochrome P450 8B1, a therapeutic target to treat obesity. *Steroids* **2022**, *178*, 108952.
- (97) Jefcoate, C. R. Measurement of substrate and inhibitor binding to microsomal cytochrome P-450 by optical-difference spectroscopy. *Methods Enzymol* **1978**, *52*, 258-279.
- (98) Isin, E. M.; Guengerich, F. P. Substrate binding to cytochromes P450. *Anal Bioanal Chem* **2008**, *392* (6), 1019-1030. DOI: 10.1007/s00216-008-2244-0 From NLM Medline.
- (99) Offei, S. D.; Arman, H. D.; Yoshimoto, F. K. Chemical synthesis of 7 α -hydroxycholest-4-en-3-one, a biomarker for irritable bowel syndrome and bile acid malabsorption. *Steroids* **2019**, *151*, 108559.
- (100) Seron-Ferre, M.; Jaffe, R. B. The fetal adrenal gland. *Annu Rev Physiol* **1981**, *43*, 141-162. DOI: 10.1146/annurev.ph.43.030181.001041 From NLM Medline.
- (101) Kuijper, E. A.; Ket, J. C.; Caanen, M. R.; Lambalk, C. B. Reproductive hormone concentrations in pregnancy and neonates: a systematic review. *Reprod Biomed Online* **2013**, *27* (1), 33-63. DOI: 10.1016/j.rbmo.2013.03.009 From NLM Medline.
- (102) Siiteri, P. K.; MacDonald, P. C. Placental estrogen biosynthesis during human pregnancy. *The Journal of clinical endocrinology and metabolism* **1966**, *26* (7), 751-761. DOI: 10.1210/jcem-26-7-751 From NLM Medline.
- (103) Frandsen, V. A.; Stakemann, G. The Site of Production of Oestrogenic Hormones in Human Pregnancy. 3. Further Observations on the Hormone Excretion in Pregnancy with Anencephalic Foetus. *Acta Endocrinol (Copenh)* **1964**, *47*, 265-276. From NLM Medline.
- (104) Newby, D.; Aitken, D. A.; Howatson, A. G.; Connor, J. M. Placental synthesis of oestriol in Down's syndrome pregnancies. *Placenta* **2000**, *21* (2-3), 263-267. DOI: 10.1053/plac.1999.0469 From NLM Medline.
- (105) Schuetz, J. D.; Kauma, S.; Guzelian, P. S. Identification of the fetal liver cytochrome CYP3A7 in human endometrium and placenta. *J Clin Invest* **1993**, *92* (2), 1018-1024. DOI: 10.1172/JCI116607 From NLM Medline.
- (106) Marill, J.; Cresteil, T.; Lanotte, M.; Chabot, G. G. Identification of human cytochrome P450s involved in the formation of all-trans-retinoic acid principal metabolites. *Molecular pharmacology* **2000**, *58* (6), 1341-1348.
- (107) Sim, S. C.; Edwards, R. J.; Boobis, A. R.; Ingelman-Sundberg, M. CYP3A7 protein expression is high in a fraction of adult human livers and partially associated with the CYP3A7*1C allele. *Pharmacogenet Genomics* **2005**, *15* (9), 625-631. DOI: 10.1097/01.fpc.0000171516.84139.89 From NLM Medline.
- (108) Fishman, J.; Schneider, J.; Hershcope, R. J.; Bradlow, H. L. Increased estrogen-16 alpha-hydroxylase activity in women with breast and endometrial cancer. *Journal of steroid biochemistry* **1984**, *20* (4B), 1077-1081. DOI: 10.1016/0022-4731(84)90021-9 From NLM

- Medline. Hevir, N.; Sinkovec, J.; Rizner, T. L. Disturbed expression of phase I and phase II estrogen-metabolizing enzymes in endometrial cancer: lower levels of CYP1B1 and increased expression of S-COMT. *Molecular and cellular endocrinology* **2011**, *331* (1), 158-167. DOI: 10.1016/j.mce.2010.09.011 From NLM Medline.
- (109) Lahita, R. G.; Bradlow, H. L.; Kunkel, H. G.; Fishman, J. Increased 16 alpha-hydroxylation of estradiol in systemic lupus erythematosus. *The Journal of clinical endocrinology and metabolism* **1981**, *53* (1), 174-178. DOI: 10.1210/jcem-53-1-174 From NLM Medline. Merrill, J. T.; Dinu, A. R.; Lahita, R. G. Autoimmunity: The Female Connection. *Medscape Womens Health* **1996**, *1* (11), 5. From NLM Publisher.
- (110) Moreira, R. P.; Jorge, A. A.; Gomes, L. G.; Kaupert, L. C.; Massud Filho, J.; Mendonca, B. B.; Bachega, T. A. Pharmacogenetics of glucocorticoid replacement could optimize the treatment of congenital adrenal hyperplasia due to 21-hydroxylase deficiency. *Clinics (Sao Paulo)* **2011**, *66* (8), 1361-1366. DOI: 10.1590/s1807-59322011000800009 From NLM Medline.
- (111) Hevir, N.; Ribic-Pucelj, M.; Lanisnik Rizner, T. Disturbed balance between phase I and II metabolizing enzymes in ovarian endometriosis: a source of excessive hydroxy-estrogens and ROS? *Molecular and cellular endocrinology* **2013**, *367* (1-2), 74-84. DOI: 10.1016/j.mce.2012.12.019 From NLM Medline.
- (112) Goodarzi, M. O.; Xu, N.; Azziz, R. Association of CYP3A7*1C and serum dehydroepiandrosterone sulfate levels in women with polycystic ovary syndrome. *The Journal of clinical endocrinology and metabolism* **2008**, *93* (7), 2909-2912. DOI: 10.1210/jc.2008-0403 From NLM Medline.
- (113) Yang, H. Y.; Lee, Q. P.; Rettie, A. E.; Juchau, M. R. Functional cytochrome P4503A isoforms in human embryonic tissues: expression during organogenesis. *Molecular pharmacology* **1994**, *46* (5), 922-928. From NLM Medline.
- (114) Lacroix, D.; Sonnier, M.; Moncion, A.; Cheron, G.; Cresteil, T. Expression of CYP3A in the human liver--evidence that the shift between CYP3A7 and CYP3A4 occurs immediately after birth. *European journal of biochemistry / FEBS* **1997**, *247* (2), 625-634. DOI: 10.1111/j.1432-1033.1997.00625.x From NLM Medline.
- (115) Hines, R. N. Ontogeny of human hepatic cytochromes P450. *Journal of biochemical and molecular toxicology* **2007**, *21* (4), 169-175. DOI: 10.1002/jbt.20179 From NLM Medline. Zane, N. R.; Chen, Y.; Wang, M. Z.; Thakker, D. R. Cytochrome P450 and flavin-containing monooxygenase families: age-dependent differences in expression and functional activity. *Pediatr Res* **2018**, *83* (2), 527-535. DOI: 10.1038/pr.2017.226 From NLM Medline. Shuster, D. L.; Risler, L. J.; Prasad, B.; Calamia, J. C.; Voellinger, J. L.; Kelly, E. J.; Unadkat, J. D.; Hebert, M. F.; Shen, D. D.; Thummel, K. E.; et al. Identification of CYP3A7 for glyburide metabolism in human fetal livers. *Biochemical pharmacology* **2014**, *92* (4), 690-700. DOI: 10.1016/j.bcp.2014.09.025 From NLM Medline.
- (116) Li, H.; Lampe, J. N. Neonatal cytochrome P450 CYP3A7: A comprehensive review of its role in development, disease, and xenobiotic metabolism. *Archives of biochemistry and biophysics* **2019**, *673*, 108078. DOI: 10.1016/j.abb.2019.108078 From NLM Medline.
- (117) Li, Y.; Yokoi, T.; Katsuki, M.; Wang, J. S.; Groopman, J. D.; Kamataki, T. In vivo activation of aflatoxin B1 in C57BL/6N mice carrying a human fetus-specific CYP3A7 gene. *Cancer research* **1997**, *57* (4), 641-645. From NLM Medline.

- (118) Sevrioukova, I. F. Structural Basis for the Diminished Ligand Binding and Catalytic Ability of Human Fetal-Specific CYP3A7. *Int J Mol Sci* **2021**, *22* (11). DOI: 10.3390/ijms22115831.
- (119) Holmans, P. L.; Shet, M. S.; Martin-Wixtrom, C. A.; Fisher, C. W.; Estabrook, R. W. The high-level expression in *Escherichia coli* of the membrane-bound form of human and rat cytochrome b5 and studies on their mechanism of function. *Archives of biochemistry and biophysics* **1994**, *312* (2), 554-565. DOI: 10.1006/abbi.1994.1345 From NLM Medline.
- (120) Estabrook, R. W.; Werringloer, J. The measurement of difference spectra: application to the cytochromes of microsomes. *Methods Enzymol* **1978**, *52*, 212-220. DOI: 10.1016/s0076-6879(78)52024-7 From NLM Medline.
- (121) Shaw, P. M.; Hosea, N. A.; Thompson, D. V.; Lenius, J. M.; Guengerich, F. P. Reconstitution premixes for assays using purified recombinant human cytochrome P450, NADPH-cytochrome P450 reductase, and cytochrome b5. *Archives of biochemistry and biophysics* **1997**, *348* (1), 107-115. DOI: 10.1006/abbi.1997.0378 From NLM Medline.
- (122) *The PyMOL Molecular Graphics System*; Schrodeinger, LLC: New York, 2017. (accessed.
- (123) Krissinel, E.; Henrick, K. Secondary-structure matching (SSM), a new tool for fast protein structure alignment in three dimensions. *Acta Crystallographica Section D* **2004**, *60* (12 Part 1), 2256-2268. DOI: doi:10.1107/S0907444904026460.
- (124) Atkins, W. M. Current views on the fundamental mechanisms of cytochrome P450 allostereism. *Expert opinion on drug metabolism & toxicology* **2006**, *2* (4), 573-579. DOI: 10.1517/17425255.2.4.573 From NLM Medline.
- (125) Cupp-Vickery, J.; Anderson, R.; Hatziris, Z. Crystal structures of ligand complexes of P450eryF exhibiting homotropic cooperativity. *Proceedings of the National Academy of Sciences of the United States of America* **2000**, *97* (7), 3050-3055. DOI: 10.1073/pnas.97.7.3050 From NLM Medline. Paquin, A.; Oufqir, Y.; Sevrioukova, I. F.; Reyes-Moreno, C.; Berube, G. Innovative C(2)-symmetric testosterone and androstenedione dimers: Design, synthesis, biological evaluation on prostate cancer cell lines and binding study to recombinant CYP3A4. *Eur J Med Chem* **2021**, *220*, 113496. DOI: 10.1016/j.ejmech.2021.113496 From NLM Medline.
- (126) Williams, P. A.; Cosme, J.; Vinkovic, D. M.; Ward, A.; Angove, H. C.; Day, P. J.; Vonrhein, C.; Tickle, I. J.; Jhoti, H. Crystal structures of human cytochrome P450 3A4 bound to metyrapone and progesterone. *Science* **2004**, *305* (5684), 683-686. DOI: 10.1126/science.1099736.
- (127) Baas, B. J.; Denisov, I. G.; Sligar, S. G. Homotropic cooperativity of monomeric cytochrome P450 3A4 in a nanoscale native bilayer environment. *Archives of biochemistry and biophysics* **2004**, *430* (2), 218-228, Research Support, Non-U.S. Gov't Research Support, U.S. Gov't, Non-P.H.S. Research Support, U.S. Gov't, P.H.S. DOI: 10.1016/j.abb.2004.07.003.
- (128) Schwab, G. E.; Raucy, J. L.; Johnson, E. F. Modulation of rabbit and human hepatic cytochrome P-450-catalyzed steroid hydroxylations by alpha-naphthoflavone. *Molecular pharmacology* **1988**, *33* (5), 493-499. From NLM Medline. He, Y. A.; He, Y. Q.; Szklarz, G. D.; Halpert, J. R. Identification of three key residues in substrate recognition site 5 of human cytochrome P450 3A4 by cassette and site-directed mutagenesis. *Biochemistry* **1997**, *36* (29), 8831-8839. DOI: 10.1021/bi970182i From NLM Medline. Harlow, G. R.; Halpert, J. R. Alanine-scanning mutagenesis of a putative substrate recognition site in human cytochrome P450 3A4. Role of residues 210 and 211 in flavonoid activation and substrate specificity. *The Journal of biological chemistry* **1997**, *272* (9), 5396-5402.

- (129) Ueng, Y. F.; Kuwabara, T.; Chun, Y. J.; Guengerich, F. P. Cooperativity in oxidations catalyzed by cytochrome P450 3A4. *Biochemistry* **1997**, *36* (2), 370-381. DOI: 10.1021/bi962359z From NLM Medline.
- (130) Kerlan, V.; Dreano, Y.; Bercovici, J. P.; Beaune, P. H.; Floch, H. H.; Berthou, F. Nature of cytochromes P450 involved in the 2-/4-hydroxylations of estradiol in human liver microsomes. *Biochemical pharmacology* **1992**, *44* (9), 1745-1756. DOI: 10.1016/0006-2952(92)90068-t From NLM Medline.
- (131) Kerr, B. M.; Thummel, K. E.; Wurden, C. J.; Klein, S. M.; Kroetz, D. L.; Gonzalez, F. J.; Levy, R. H. Human liver carbamazepine metabolism. Role of CYP3A4 and CYP2C8 in 10,11-epoxide formation. *Biochemical pharmacology* **1994**, *47* (11), 1969-1979. DOI: 10.1016/0006-2952(94)90071-x From NLM Medline.
- (132) Harlow, G. R.; Halpert, J. R. Analysis of human cytochrome P450 3A4 cooperativity: construction and characterization of a site-directed mutant that displays hyperbolic steroid hydroxylation kinetics. *Proceedings of the National Academy of Sciences of the United States of America* **1998**, *95* (12), 6636-6641.
- (133) Polic, V.; Auclair, K. Allosteric Activation of Cytochrome P450 3A4 via Progesterone Bioconjugation. *Bioconjug Chem* **2017**, *28* (4), 885-889. DOI: 10.1021/acs.bioconjchem.6b00604 From NLM. Ducharme, J.; Polic, V.; Auclair, K. A Covalently Attached Progesterone Molecule Outcompetes the Binding of Free Progesterone at an Allosteric Site of Cytochrome P450 3A4. *Bioconjugate Chemistry* **2019**, *30* (6), 1629-1635. DOI: 10.1021/acs.bioconjchem.9b00248.
- (134) Nakamura, H.; Torimoto, N.; Ishii, I.; Ariyoshi, N.; Nakasa, H.; Ohmori, S.; Kitada, M. CYP3A4 and CYP3A7-mediated carbamazepine 10,11-epoxidation are activated by differential endogenous steroids. *Drug metabolism and disposition: the biological fate of chemicals* **2003**, *31* (4), 432-438. DOI: 10.1124/dmd.31.4.432 From NLM Medline.
- (135) He, S.; Nelson, E. R. 27-Hydroxycholesterol, an endogenous selective estrogen receptor modulator. *Maturitas* **2017**, *104*, 29-35. DOI: 10.1016/j.maturitas.2017.07.014 From NLM.
- (136) Ma, L.; Wang, L.; Nelson, A. T.; Han, C.; He, S.; Henn, M. A.; Menon, K.; Chen, J. J.; Baek, A. E.; Vardanyan, A.; et al. 27-Hydroxycholesterol acts on myeloid immune cells to induce T cell dysfunction, promoting breast cancer progression. *Cancer Lett* **2020**, *493*, 266-283. DOI: 10.1016/j.canlet.2020.08.020 From NLM.
- (137) Torres, C. G.; Ramírez, M. E.; Cruz, P.; Epuñan, M. J.; Valladares, L. E.; Sierralta, W. D. 27-hydroxycholesterol induces the transition of MCF7 cells into a mesenchymal phenotype. *Oncol Rep* **2011**, *26* (2), 389-397. DOI: 10.3892/or.2011.1284 From NLM.
- (138) Norlin, M.; von Bahr, S.; Björkhem, I.; Wikvall, K. On the substrate specificity of human CYP27A1: implications for bile acid and cholestanol formation. *Journal of lipid research* **2003**, *44* (8), 1515-1522. DOI: <https://doi.org/10.1194/jlr.M300047-JLR200>.
- (139) Pikuleva, I. A.; Björkhem, I.; Waterman, M. R. Expression, Purification, and Enzymatic Properties of Recombinant Human Cytochrome P450c27 (CYP27). *Archives of biochemistry and biophysics* **1997**, *343* (1), 123-130. DOI: <https://doi.org/10.1006/abbi.1997.0142>.
- (140) Gupta, R. P.; Patrick, K.; Bell, N. H. Mutational analysis of CYP27A1: assessment of 27-hydroxylation of cholesterol and 25-hydroxylation of vitamin D. *Metabolism: clinical and experimental* **2007**, *56* (9), 1248-1255. DOI: 10.1016/j.metabol.2007.04.023 PubMed.
- (141) Mast, N.; Lin, J. B.; Pikuleva, I. A. Marketed Drugs Can Inhibit Cytochrome P450 27A1, a Potential New Target for Breast Cancer Adjuvant Therapy. *Molecular pharmacology* **2015**, *88* (3), 428-436. DOI: 10.1124/mol.115.099598 From NLM Medline.

- (142) Lam, M.; Mast, N.; Pikuleva, I. A. Drugs and Scaffold That Inhibit Cytochrome P450 27A1 In Vitro and In Vivo. *Molecular pharmacology* **2018**, *93* (2), 101-108. DOI: 10.1124/mol.117.110742 From NLM Medline.
- (143) Das, A.; Mukhopadhyay, C. Urea-mediated protein denaturation: a consensus view. *The journal of physical chemistry. B* **2009**, *113* (38), 12816-12824. DOI: 10.1021/jp906350s From NLM.
- (144) Sliwoski, G.; Kothiwale, S.; Meiler, J.; Lowe, E. W., Jr. Computational methods in drug discovery. *Pharmacological reviews* **2014**, *66* (1), 334-395. DOI: 10.1124/pr.112.007336 From NLM.